Investigation of Alternative Evaluation Spaces for Failure Prediction in Sheet Metals

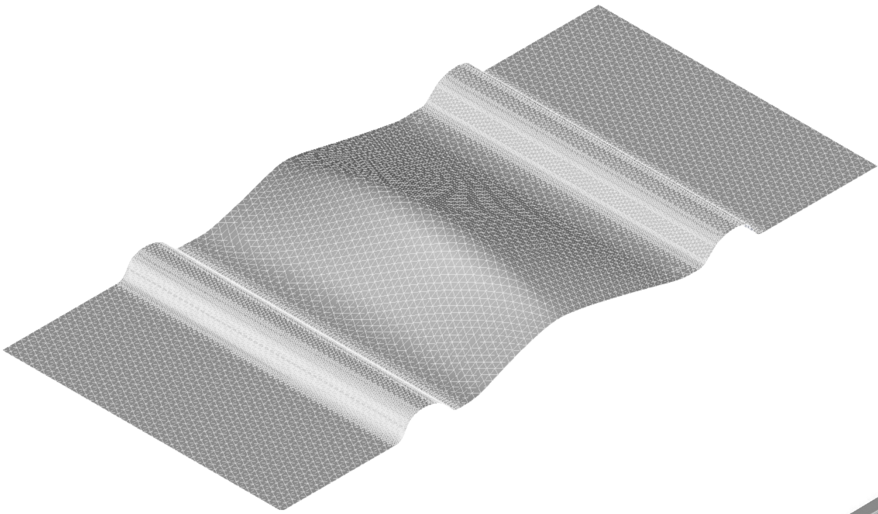

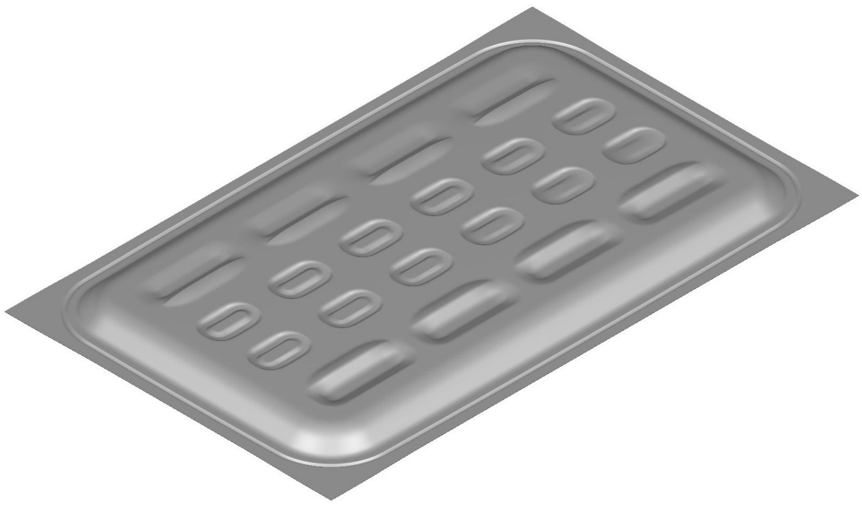

Master Thesis

Alexander Bendix Krukow Barlo

Aalborg University
Faculty of Engineering and Science
Department of Materials and Production

AALBORG UNIVERSITY
STUDENT REPORT

Faculty of Engineering and Science
Department of Materials and Production
Fibigerstræde 16
DK-9220 Aalborg Øst
http://www.mp.aau.dk

Title:
Investigation of Alternative Evaluation Spaces for Failure Prediction in Sheet Metals

Subtitle:
-

Project:
Master Thesis

Project period:
February 2019 - June 2019

Collaborative Company:
Volvo Cars Body Components, Olofstrom

Author:
Alexander Bendix Krukow Barlo
`abarlo14@student.aau.dk`

Signed 31.05.2019

Supervisor (AAU):
Benny Endelt

Suporvisor (Volvo):
Dr. Mats Sigvant

Circulation: 1
Pages of Main Report: 62
Pages of Appendices: 21
Pages in Total: 83
Date of completion: 31.05.2019

Abstract:

The following Master Thesis is a result of a stay at Volvo Cars Body Components in Olofström, Sweden. The project concerns failure prediction of mainly an AA6016 aluminium alloy exposed to bending-under-tension.
The work presented in this report initially aimed to validate the *Generalized Incremental Stress State Dependant Damage Model* (GISSMO) failure prediction approach using Finite Element simulations of a bending-under-tension specimen bend over a tool with a nose radius of 6 mm. The GISSMO approach was attempted validated by transforming the standard Forming Limit Curve (FLC) and the specimen strain field from the principal strain space to a stress triaxiality based space. This transformation was performed using transformation equations derived from the von Mises constitutive equations. Using the GISSMO model as a digital post-processing tool, the failure of the aluminium specimen, and an identical specimen using an CR440Y780T-DP dual-phase steel alloy for further validation, was found. This failure determination showed that the GISSMO model performed well for the aluminium alloy, but poorly for the dual-phase steel alloy when trying to determine the onset of localized necking.
The poor performance of the GISSMO failure prediction approach on the dual-phase steel was concluded to be due to the bending effect in the material. With this conclusion, an attempt to create a bending correction of the standard FLC was initiated. A method for bending correction of the FLC was proposed using the failure strains of bending-under-tension experimental tests with punch nose radii 3, 6, and 10 mm. To distinguish between these corrected curves, the tool curvature was introduced as a third parameter, creating a Bending Corrected Forming Limit Surface (BC-FLS). The proposed failure prediction approach was validated using an available Volvo Cars Test Die panel using the same AA6016 aluminium alloy. Applying the proposed method post-processing to the panel in the commercial Finite Element code AutoForm^{plus} R8, the failure states of 8 different zones were predicted accurately. The results of the BC-FLS approach was compared to that of the standard FLC and proved to be far superior.

Preface

This Master Thesis is completed by Alexander Bendix Krukow Barlo (AAU student ID 20142261) on the 4^{th} semester of the master program in Manufacturing Technology at Aalborg University. The project is carried out and completed in the time period from the 1^{st} of February 2019 to the 3^{rd} of June 2019. The work presented in this master thesis is a result of a collaboration with Volvo Cars Body Components in Olofström, Sweden, and is equivalent to an entire semesters work (30 ECTS credits).

The content of this report is available for the public, however, publication of the presented results must only occur after agreement with the author and Volvo Cars Body Components, and with correct citation.

Acknowledgements

The author of this report would like to express his gratitude firstly towards his two supervisors Dr. Mats Sigvant from Volvo Cars Body Components, and Benny Ø. Endelt from Aalborg University for their professional and competent guidance through the project period.

The author would also like to direct a special thanks to Dr. Niko Manopulo from AutoForm Engineering GmbH for interesting discussions about the investigated GISSMO approach. Furthermore, the author would like to thank Mr. Kristoffer Trana for sharing his results and Finite Element model regarding the Volvo Cars Test Die.

Literature

The citations in the report complies to the Harvard citation methodology. References in this report are highlighted in the text with blue color and constructed of the author(s) last name(s) and the year of publication. An example hereof is given: Banabic (2010). If used literature is published by more than two authors, the last name of the first author will be used, and followed by *et al.* An example hereof is given: Volk et al. (2012).

Figures and Tables

The enumeration of figures and tables follow the chapter number and order in which these are presented. This means, that e.g. the first table in Chapter 3 will be referred to as Table 3.1.

Appendix

Appendices in this report is given a Latin letter and is listed in alphabetic order. References to the specific appendix will be in the text referring only to the Latin letter assign to the appendix, and not to the name of the appendix. An example hereof is given: *...the full derivation of Equations 5.15 and 5.16 can be found in Appendix A.*

An electronic appendix has also been submitted containing e.g. the MatLab script used for the GISSMO failure prediction approach. For this electronic appendix, a guide explaining the purpose of the contents can be found in Appendix C.

Conference Contributions

Throughout the project period, the author has also submitted two scientific papers and a poster to two different conferences on the topic of sheet metal forming:

Conference	Paper / Poster Title	Conference Status
IDDRG 2019, 3rd-7th of June 2019, Enschede, The Netherlands	*On the Failure Prediction of Dual-Phase Steel and Aluminium Alloys Exposed to Combined Tension and Bending*	Accepted
FTF 2019, 19th-20th of September 2019, Munich, Germany	*Investigation of a Bending Corrected Forming Limit Surface for Failure Prediction in Sheet Metals (paper)*	Under review
FTF 2019, 19th-20th of September 2019, Munich, Germany	*Investigation of a Bending Corrected Forming Limit Surface for Failure Prediction in Sheet Metals (poster)*	Under review

Both papers have been included in the back of the report, while the poster can be found in the electronic appendix.

Resumé

Det følgende projekt er forfatterens kandidatspeciale for uddannelsen *Virksomhedsteknologi* ved Aalborg Universitet. Projektet er udarbejdet i samarbejde med Volvo Cars Body Components i Olofström, Sverige, og omhandler en undersøgelse af alternative evalueringsmetoder for komponenter fremstillet af plademetal, med henblik på forudsigelse af halsdannelse. Som udgangspunkt har reporten fokuseret på nøjagtigt forudsigelse af halsdannelse i komponenter af en AA6016 aluminiumslegering udsat for kombineret stræk og bøjning. Hvor det har været muligt, har en CR440Y780T-DP to-fase stållegering været anvendt til at verificere metoder, der har vist gode egenskaber for den tidligere nævnte aluminiumslegering. Projektet tager udgangspunkt i følgende problemformulering:

"How can the onset of necking accurately be predicted by Finite Element simulations tools for AA6016 aluminium sheets exposed to various cases of combined tension and bending?"

I første del tages der udgangspunkt i forfatterens tidligere arbejde med lignende forskningsområde, i forbindelse med et akademisk praktikophold hos selv samme virksomhed (Barlo 2019). Denne første del arbejder videre fra det foreslåede videre arbejde, og undersøger en evaluaerignsmetode ved navn GISSMO (*Generalized Incremental Stress State Dependant Damage Model*). Denne metode er baseret på en transformation af den standarde formbarhedskurve (FLC) samt tøjningsfeltet gennem transformationsligninger, udledt fra von Mises konstitutive model. De udledte von Mises baserede transformationsligninger sammenlighes med transformationsligninger baseret på den konstitutive model af Banabic-Balan-Comsa (BBC05). Her vurderes det, at forskellen på resultatet af de to er negligerbar, hvorfor de von Mises basered transformationsligninger vælges, da disse kan udtrykkes eksplicit hvorimod transformationsligningerne baseret på BBC05 kræver en implicit implementering af materialeroutinen. To komponenter, begge udsat for kombineret stræk og bøjning over et stempel med radius 6 mm, anvendes til at validere metoden. Her forudsiges halsdannelsen nøjagtigt for aluminiumslegeringen, imens dårlig performance ses for den anvendte to-fase stållegering. På baggrund af dette undersøges indflydelsen af bøjningen på emnerne.

Undersøgelsen af bøjningens indflydelse på materialerne viser, at en reduktion i bukkeradius resulterer i en forøgelse af grænsetøjningen for begge materialer. Dog ses denne effekt størst for den undersøge to-fase stållegering. På baggrund af dette præsenteres en ny metode til forudsigelse af halsdannelse baseret på det nuværende formbarhedsdiagram (FLD), samt krumningen af emneoverfladen for tre eksperimentielle tests af kombineret stræk og bøjning med stempal radier 3, 6 og 10 mm . Dette flytter det todimensionelle FLD ind i et tredimensionelt rum, hvor en grænseflade præsenteres som en *Bending Corrected Forming Limit Surface (BC-FLS)*. Da de tidligere anvendte emner udsat for kombineret stræk og bøjning er anvendt til frembringelsen af grænsefladen, anvendes et specielt testpanel designet hos Volvo Cars med stempel radier 4 og 8 mm til at validere modellen, for den undersøgte aluminiumslegering. Metoden implementeres i den kommerciele Finite Element kode AutoForm$^{\text{plus}}$ R8, og formår at forudsige haldannelsen præcist.

Ved at have testet ovenstående to tilgange svares der ikke fuldstændingt på den præsenterede problemformulering. Dette vurderes da den præsenterede BC-FLS model stadig har kritiske mangler, men samtidig vurderes det at introduktionen af denne metode er et skridt i den rigtige retning, i forhold til nøjagtig forudsigelse af halsdannelse i plademateriale gennem digitale værktøjer.

Nomenclature

Symbol(s)	SI-Unit	Explanation
Latin Symbols		
D	[-]	Damage measure.
$\dot{D}$	[-]	First derivative of the damage measure with respect to time.
d_i	[-]	Damage variables in the Johnson-Cook damage model.
F	[-]	Failure measure.
F_{max}	[-]	Maximum failure measure.
F_{nl}	[-]	Non-linear failure measure.
F_{punch}	[N]	Punch force.
$\boldsymbol{I}$	[-]	Identity matrix.
k	[-]	Stress ratio.
M	[-]	Exponent in the BBC05 yield criteria.
n	[-]	Damage exponent in the GISSMO failure prediction approach.
p	[Pa]	Hydrostatic pressure.
R	[m]	Punch nose radius.
r_i	[-]	Lankford coefficient describing the plastic anisotropy of the rolled sheet metal. i can either take an angle value θ or express the biaxial case b.
$\boldsymbol{s}$	[Pa]	Deviatoric stress tensor.
s	[m]	Punch displacement.
t	[s]	Time.
Greek Symbols		
α	[-]	Ratio between tool radius and sheet thickness.
$\boldsymbol{\varepsilon}$	[-]	Strain tensor.
ε_{crit}	[-]	Critical strain in the GISSMO failure prediction approach.
ε_f	[-]	Failure strain.
ε_{ii}	[-]	Principal strain.
ε^p	[-]	Effective plastic strain.
$\dot{\varepsilon}$	$[s^{-1}]$	Strain rate.
$\overline{\varepsilon}^p$	[-]	Equivalent plastic strain.
η	[-]	Stress triaxiality.
θ	[°]	Angle to the rolling direction of the sheet metal.
κ	[m^{-1}]	Formed blank curvature.
μ_i	[-]	Coulomb friction coefficient in friction zone i.
$\boldsymbol{\sigma}$	[Pa]	Stress tensor.
σ	[-]	True stress.
σ_{ii}	[Pa]	Principal stress.
σ_m	[Pa]	Mean stress.
$\overline{\sigma}$	[-]	Equivalent stress.
$\overline{\sigma}_{vm}$	[Pa]	von Mises equivalent stress.

Contents

Contents

1 Introduction

The automotive industry is one of the fastest moving and highest technological advanced industries in the world. Due to this, the competition within the industry requires continuous improvement in the reduction of lead time as well as development costs. One way to achieve such improvements is by the application of Computer Aided Engineering (CAE), particularly with the use of Finite Element simulation tools. One area where the application of Finite Element simulation tools is widely used, is in the departments concerning the stamping of both interior and exterior body components. In order to ensure the stamping process feasibility, an area that has received a lot of attention in the last decade is the accurate prediction of failure in both stamping and car crash event simulations (Mattiasson et al. 2014). In order to reduce the weight of cars today, the industry has drifted towards the use of high strength steels and aluminium alloys in the manufacturing of car body components. A downside to introducing said materials in the manufacturing process is, that the ductility of these materials is reduced significantly compared to those materials used previously. This reduction in ductility inevitably makes the already difficult task of car body component manufacturing even more difficult, and, at the same time, increases the need for a general, accurate failure prediction method.

The work presented in this Master Thesis will investigate alternative failure prediction approaches for the bending-under-tension loading case.

1.1 Previous Work

The work presented in this report will be an extension of the work presented in Barlo (2019) and Barlo et al. (2019). The work previously presented on this topic has focused on the failure prediction of an AA6016 aluminium and a CR440Y780T-DP dual-phase steel specimen exposed to combined tension and bending. The specimens have been tested in the experimental setup presented in Figure 1.1 with a punch nose radius of 6 mm.

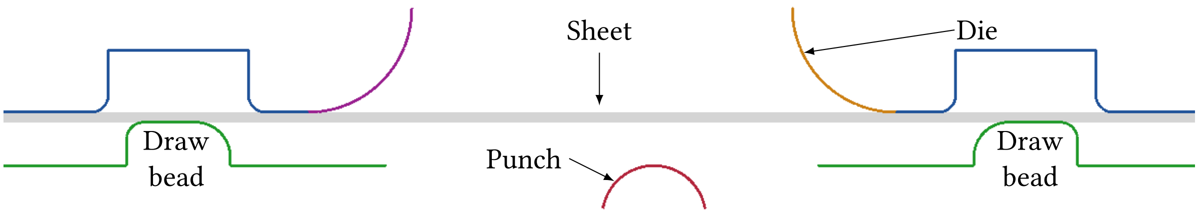

Figure 1.1. Cross-sectional view of the experimental setup geometry.

The following sections will present the key findings of the previous work.

1.1.1 Numerical Models

In Barlo (2019) numerical models were created in the commercial Finite Element (FE) code AutoForm^{plus} R7.04 with the purpose of reproducing experimental results recorded with the Digital Image Correlation (DIC) software ARAMIS^{TM} by GOM. For the models to accurately predict the major strain behaviour of the experimental results, the material models used hardening curves constructed from a combination of tensile tests and bulge tests. The hardening curves of both the AA6016 aluminium alloy and the CR440Y780T-DP dual-phase steel alloy can be found in Figures 1.2 and 1.3 respectively.

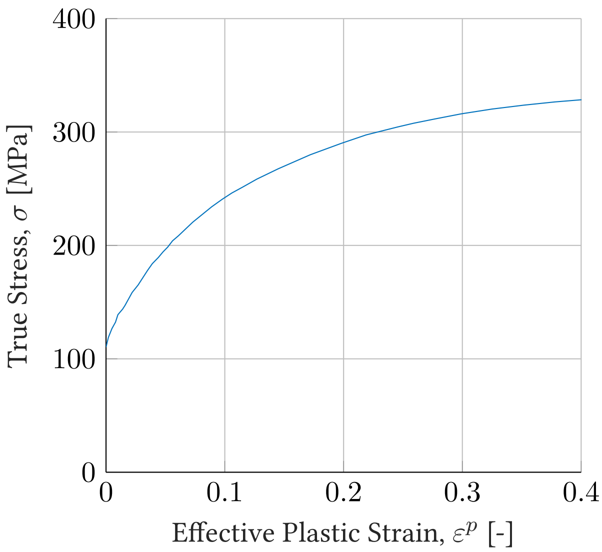

Figure 1.2. Hardening curve of the AA6016 aluminium alloy.

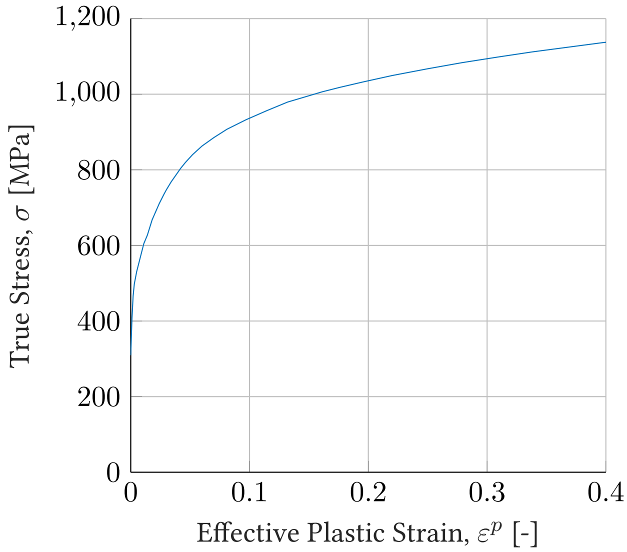

Figure 1.3. Hardening curve of the CR440Y780T-DP dual-phase steel alloy.

The anisotropic behaviour of the two materials was taken into account by using the Banabic-Balan-Comsa (BBC05) yield criterion. The exponent parameter (M) was found optimal when deviating from the standard values (6 for BCC crystallographic structures and 8 for FCC crystallographic structures (Banabic & Sester 2012)). The calibration of the M parameter was performed by inverse modelling of the Limiting Dome Height (LDH) test. Table 1.1 presents an overview of the parameters used for the material modelling.

Parameter	AA6016 Aluminium Alloy	CR440Y780T-DP Dual-Phase Steel Alloy
σ_0	110.3 [MPa]	309.5 [MPa]
σ_{45}	105.9 [MPa]	307.8 [MPa]
σ_{90}	106.5 [MPa]	313.4 [MPa]
σ_b	98.3 [MPa]	307.5 [MPa]
Yield Criterion	BBC05	BBC05
r_0	0.732	0.678
r_{45}	0.535	0.875
r_{90}	0.677	0.848
r_b	1.01	1.02
Exponent (M)	5.7	6.2

Table 1.1. Material model parameters used in the two numerical models.

The friction in the two models was modelled dividing the model into five Coulomb friction zones. The zones can be seen on Figure 1.4, and the applied coefficients can be found in Table 1.2.

Applying the presented numerical settings yielded models with acceptable accuracy for the purpose of predicting failure.

1.1.2 Failure Prediction Approaches

In both Barlo (2019) and Barlo et al. (2019) two failure prediction approaches, currently implemented in AutoForm$^{\text{plus}}$ R7.04, were evaluated:

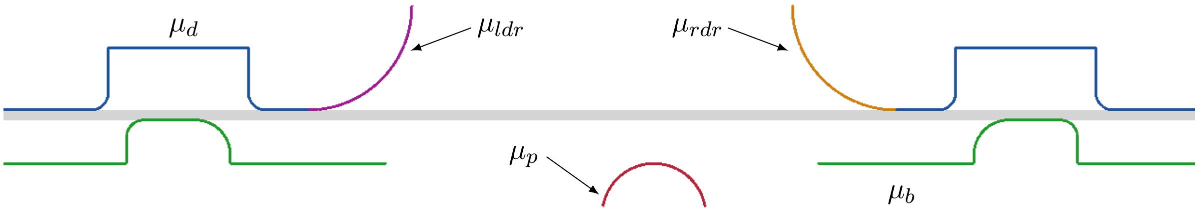

Figure 1.4. Friction zones used for the numerical models (Barlo et al. 2019).

Zone	**Notation**	**AA6016 Aluminium Alloy**	**CR440Y780T-DP Dual-Phase Steel Alloy**
Punch	μ_p	0.1	0.1
Die	μ_d	0.3	0.07
Binder	μ_b	0.3	0.07
Left Draw Radius	μ_{ldr}	0.05	0.08
Right Draw Radius	μ_{rdr}	0.07	0.03

Table 1.2. Coulomb friction coefficients applied to the different friction zones in the numerical models.

1. The standard Forming Limit Diagram (FLD)
2. The Non-linear Forming Limit Diagram

Standard Forming Limit Diagram (FLD)

In Barlo (2019) and Barlo et al. (2019), the standard Forming Limit Diagram was evaluated. Figures 1.5 and 1.6 present the strain paths of the element in both Finite Element models having the highest major strain value at the end of the simulation. For each model, the strain path is found in the membrane, upper, and lower layer.

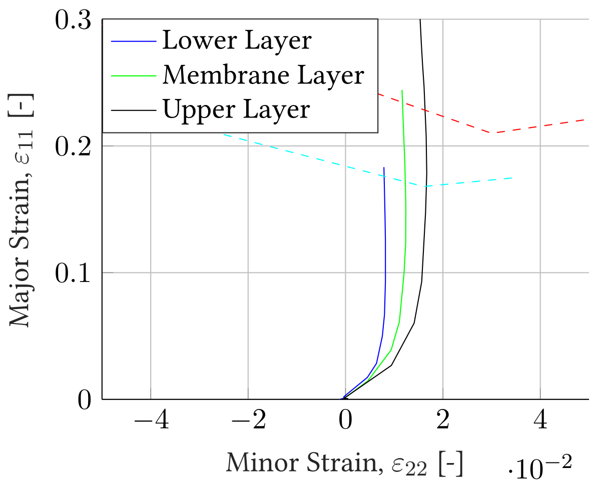

Figure 1.5. Strain paths of the AA6016 aluminium alloy.

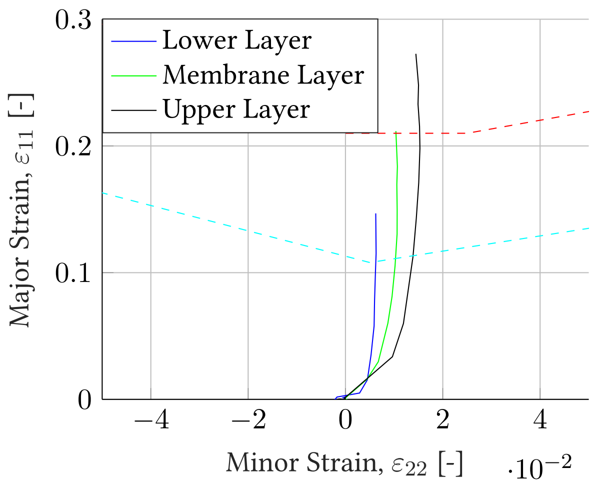

Figure 1.6. Strain paths of the CR440Y780T-DP dual-phase steel alloy.

In the evaluation of the method, it was found not applicable as a suitable failure criterion for specimens exposed to combined tension and bending, due to its inability to handle the non-linear strain paths in the models.

Non-linear Forming Limit Diagram

In Barlo (2019) the Non-linear Forming Limit Diagram was evaluated as a failure criterion for fracture in the upper layer of the model. This error was corrected by Barlo et al. (2019) evaluating the Non-linear Forming Limit Diagram as a failure criterion for necking in the membrane layer instead. The point of instability in each experiment was determined based on an approach relying on the development of the first derivative with respect to time of the major strain (major strain rate, $\dot{\varepsilon}_{11}$). The point of instability was recreated in the numerical models, and both the standard Forming Limit Diagram and the Non-linear Forming Limit Diagram were evaluated at this point. Both the standard Forming Limit Diagram and the Non-linear Forming Limit Diagram of both materials at the point of instability can be found in Figure 1.7.

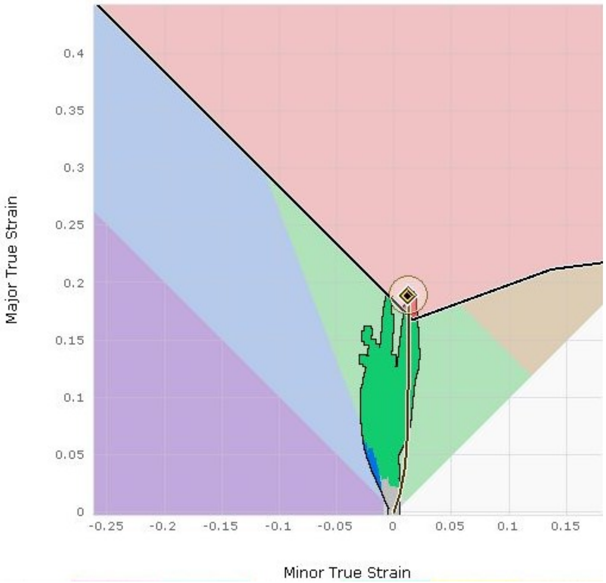

(a) Standard Forming Limit Diagram of the AA6016 aluminium alloy.

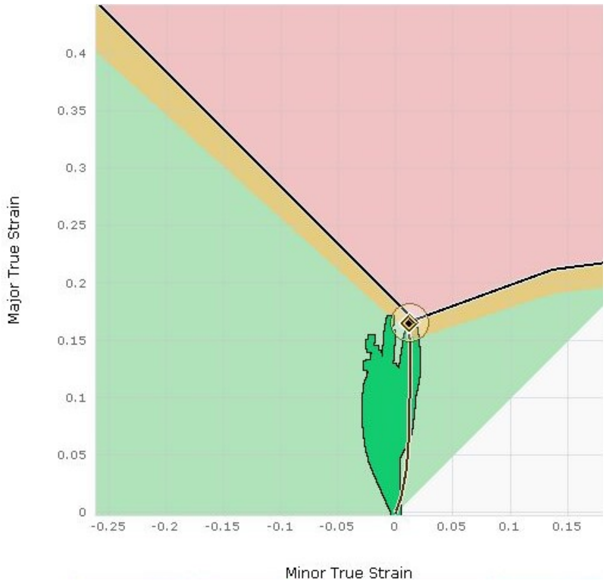

(b) Non-linear Forming Limit Diagram of the AA6016 aluminium alloy.

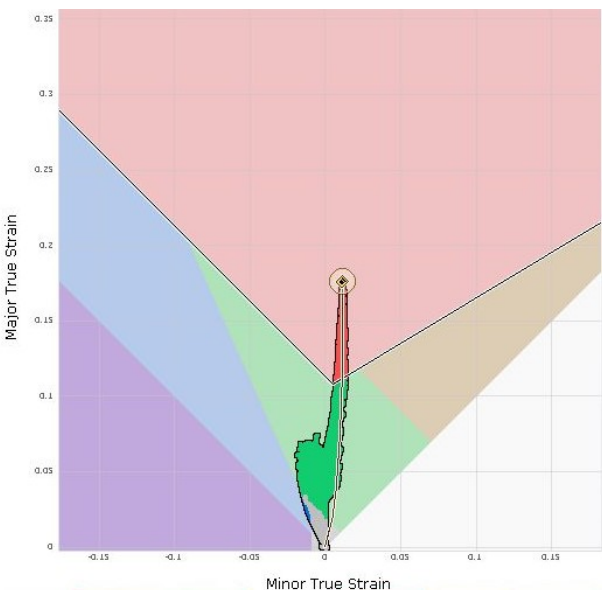

(c) Standard Forming Limit Diagram of the CR440Y780T-DP dual-phase steel alloy.

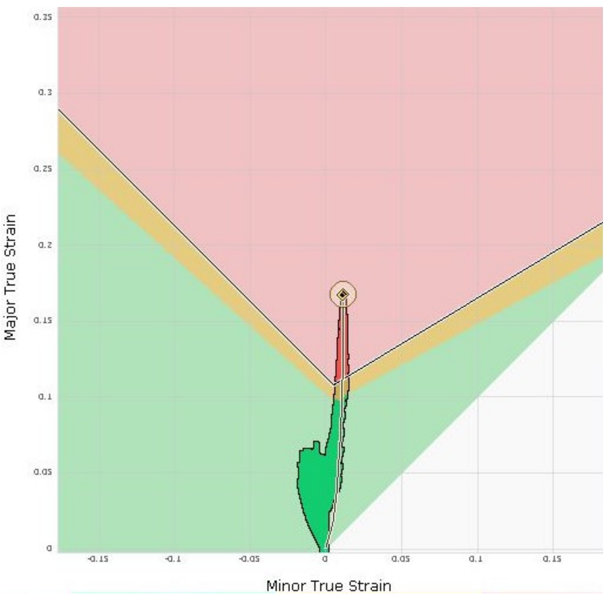

(d) Non-linear Forming Limit Diagram of the CR440Y780T-DP dual-phase steel alloy.

Figure 1.7. Standard Forming Limit Diagrams (FLD) and Non-linear Forming Limit Diagrams at the point of instability for the AA6016 aluminium alloy (a and b) and the CR440Y780T-DP dual-phase steel alloy (c and d).

Figures 1.7(a) and 1.7(b) presents the results of the AA6016 aluminium alloy. In this case, the Non-linear Forming Limit Diagram performs well, as it predicts the specimen to be on the border of necking, which was the modelled state. Figures 1.7(c) and 1.7(d) presents the results for the CR440Y780T-DP dual-phase steel alloy. In this case, the Non-linear Forming Limit Diagram was not able to predict the onset of necking. Due to the unstable performance of the Non-linear Forming Limit Diagram, it could not be accepted as a generally accurate approach for failure prediction in its current implementation in AutoForm^{plus} R7.04.

1.1.3 Summary

The previous work of Barlo (2019) and Barlo et al. (2019) presented numerical models for an AA6016 aluminium alloy and a CR440Y780T-DP dual-phase steel alloy with acceptable accuracy, that can be directly used in the work presented in this Master Thesis. Furthermore, two failure prediction approaches have been evaluated:

1. The standard Forming Limit Diagram (FLD)
2. The Non-linear Forming Limit Diagram

Both approaches were deemed not acceptable as general approaches for the prediction of failure in specimens exposed to combined tension and bending.

1.2 Defining the Term 'Failure'

Failure is a term that covers two different modes, that varies depending on the field of research:

1. **Necking:** A diffuse or local neck (Figure 1.8) presents itself in the specimen
2. **Fracture:** A clear visible fracture (Figure 1.9) occurs in the specimen

In literature mentioning failure today, the fracture mode is by far the most frequent definition. Even within the automotive industry, the definition of failure differs from department to department, where e.g. the crash community defines failure in line with the literature, and some members of the stamping community defines the point of failure at the onset of localized necking.

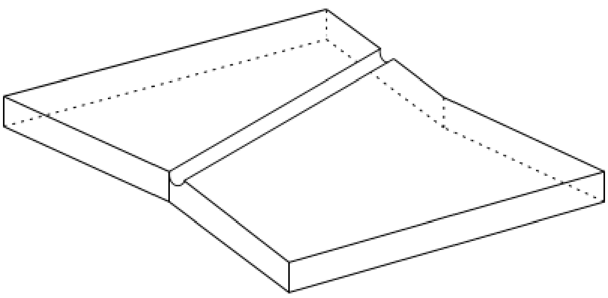

Figure 1.8. Example of the combined diffuse and localized necking phenomena. Please note that the severity of both phenomena is exaggerated for the purpose of visualization.

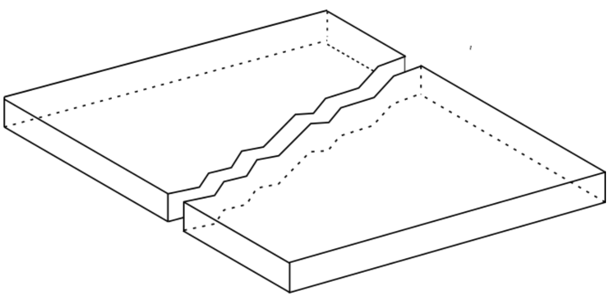

Figure 1.9. Example of the fracture phenomenon.

Despite the different definitions of the term failure, in sheet metal parts, this will occur following one of the in Figure 1.10 presented three scenarios. According to Mattiasson et al. (2014), the most common scenario for a sheet undergoing forming to follow, is scenario 1.

At Volvo Cars the main objective is to determine a general failure prediction approach to predict the onset of localized necking in the stamped parts. The reason for this definition is, that a component having reached the point of necking, will automatically be deemed as non-conforming if detected. If the component is in

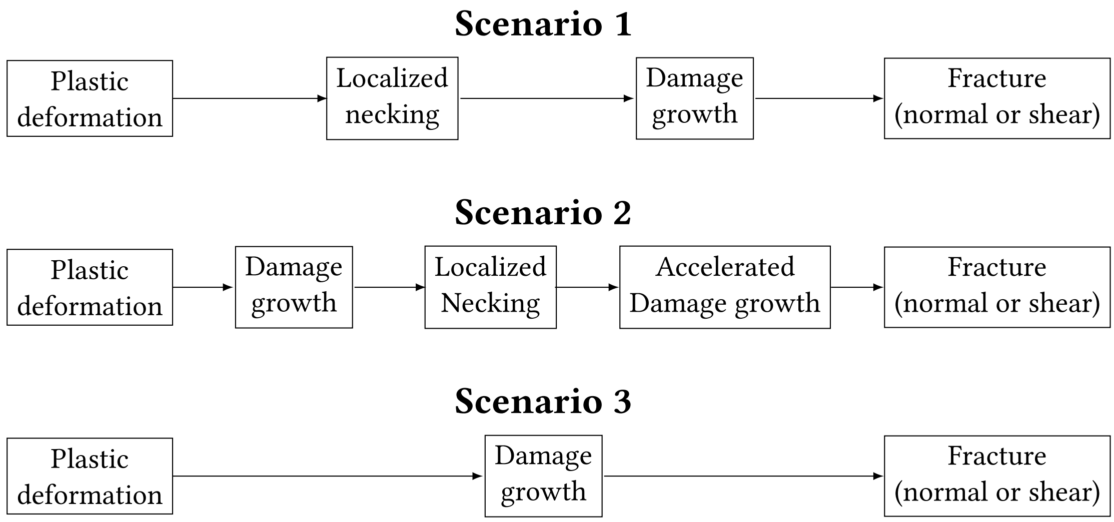

Figure 1.10. Three different scenarios leading to fracture in sheet metal (Mattiasson et al. 2014). Scenario 1 is the most common in sheet metal forming operations.

the 'twilight zone', and the neck is not detected, this will have a damaging effect on the structural integrity of the component during e.g. a crash test.

Several authors, including Sowerby & Duncan (1971) and Needleman & Tvergaard (1977), have argued that there is an intermediate state between the plastic deformation and localized necking presented in scenario 1 in Figure 1.10. This intermediate state defines the phenomenon of diffuse necking as know from a uniaxial tensile test. Figures 1.11 and 1.12 illustrates the isolated cases of the diffuse necking and localized necking phenomena respectively.

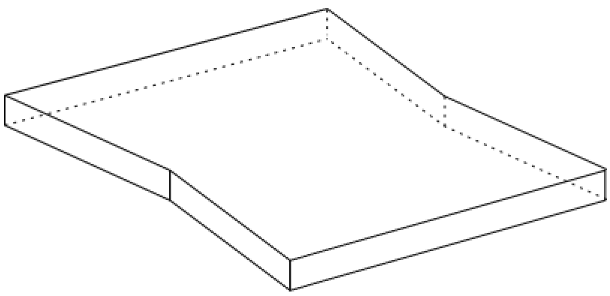

Figure 1.11. Illustration of the isolated diffuse necking phenomenon. Please note that the severity of the phenomenon is exaggerated for the purpose of visualization.

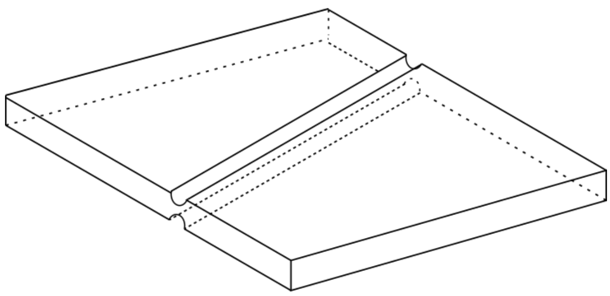

Figure 1.12. Illustration of the isolated localized necking phenomenon. Please note that the severity of the phenomenon is exaggerated for the purpose of visualization.

An uniaxial tensile test, tested in the sheet rolling direction, of the AA6016 aluminium alloy, recorded with the Digital Image Correlation (DIC) software ARAMIS$^{\mathrm{TM}}$, is used as a case to investigate the two phenomena.

$$r_\theta = \frac{\varepsilon_{22}}{\varepsilon_{33}} \tag{1.1}$$

$$\varepsilon_{33} = -(\varepsilon_{11} + \varepsilon_{22}) \tag{1.2}$$

From the definition of the Lankford coefficient in direction θ (Equation 1.1), and the rule of constant volume (Equation 1.2), the following relation can be made to describe the theoretical major strain value of a tensile test specimen at any given minor strain value:

$$\varepsilon_{11} = \frac{(1 + r_\theta) \cdot \varepsilon_{22}}{r_\theta} \tag{1.3}$$

The relations are used to create the theoretical strain path, presented in Figure 1.14. As the strain path is linear for the uniaxial tensile test, the standard Forming Limit Diagram (FLD) can be used to evaluate the test. Figure 1.13 presents the uniaxial tensile test specimen with indications of both diffuse and localized necking, and the point cloud (ε_{22},ε_{11}) of both cases is presented in Figure 1.14.

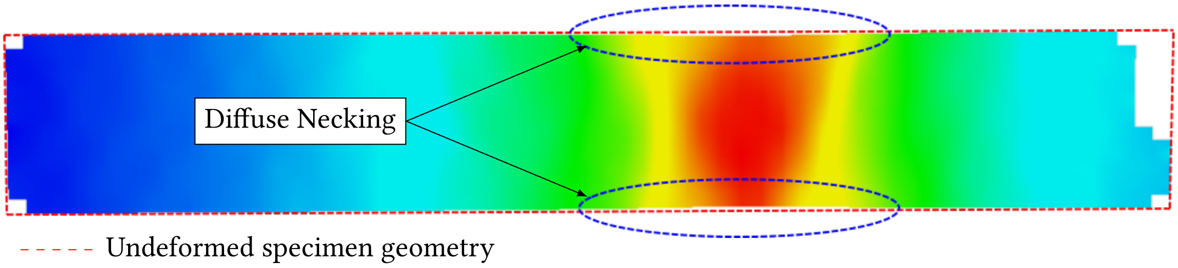

(a) Diffuse necking phenomenon.

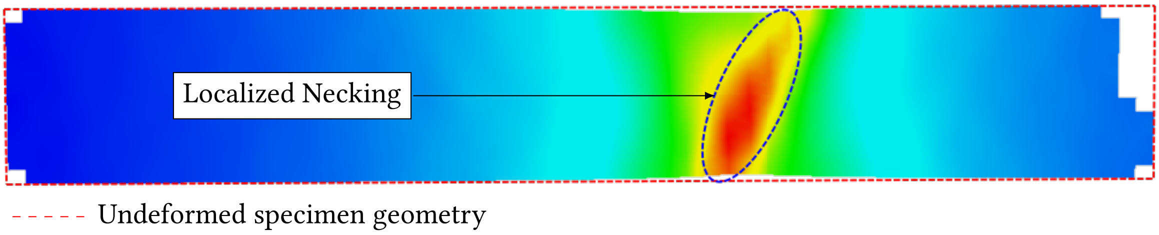

(b) Localized necking phenomenon.

Figure 1.13. Uniaxial tensile test of the AA6016 aluminium alloy recorded with ARAMIS^{TM}. The illustration presents both the case of (a) diffuse necking, and (b) localized necking.

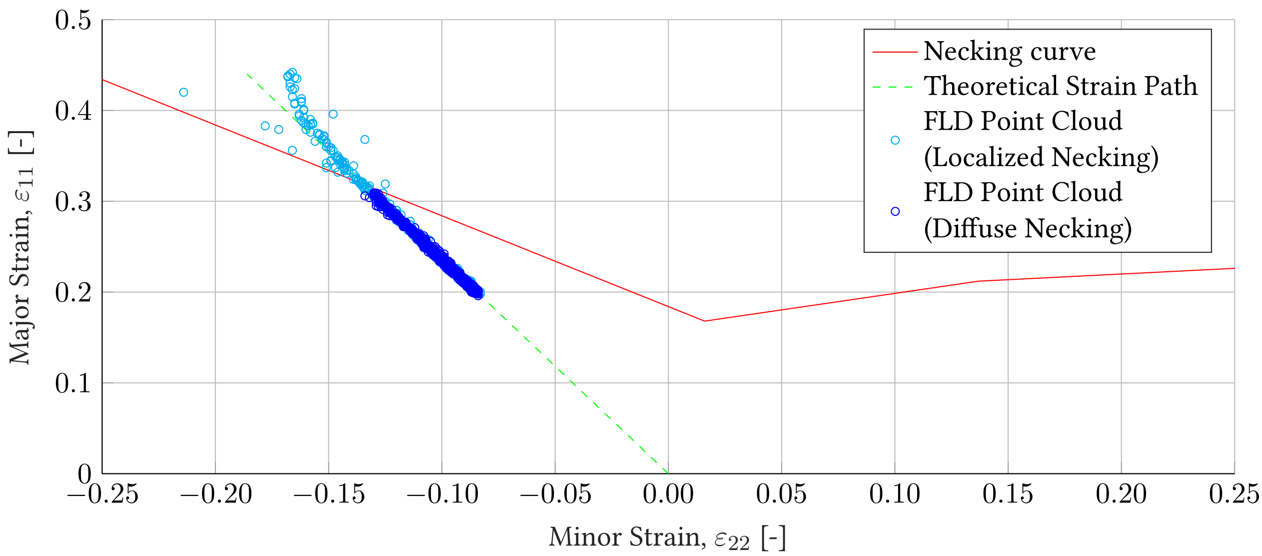

Figure 1.14. Forming Limit Diagram (FLD) of the AA6016 aluminium alloy uniaxial tensile test. The FLD contains a point cloud for the specimen having reach both diffuse necking and localized necking.

The Forming Limit Curve (FLC) included in the Forming Limit Diagram (FLD) in Figure 1.14 represents the necking limit, and according to ISO standard *ISO 12004-2:2008*, all points below this curve should not lead to specimen failure (Yoshida et al. 2008). As it appears from Figure 1.14, none of the points in the point cloud from the diffuse necking state passes the necking curve, thereby not causing failure in the specimen.

Based on this small exercise, it is determined that the final definition of the term 'failure' in this report will cover the phenomenon of localized necking.

1.3 Thesis Delimitation

From the presented previous work, the project can be driven in several directions. Therefore, in order to specify the scope of the project, the following section will present the thesis delimitation.

Where the work presented in Barlo (2019) focused on both an aluminium and a dual-phase steel alloy, this thesis will primarily focus on the failure prediction of specimens/components of the AA6016 aluminium alloy. If good results are obtained for the aluminium component, the dual-phase steel alloy will be used for further validation. The choice of focusing on the AA6016 aluminium alloy rather than on the CR440Y780T-DP dual-phase steel alloy is justified by the amount of available experimental data for the two alloys. Where experimental data for the dual-phase steel is available for three bending-under-tension tests with punch nose radii of 3, 6, and 10 mm, the same experimental data is available for the aluminium alloy, and additional data for a special test die panel developed at Volvo Cars as well.

In order to have an initial working hypothesis, the specimens/components tested in this report is assumed not to experience damage growth before the onset of localized necking i.e. following failure scenario 1. Furthermore, in Section 1.2, the term failure was defined as the onset of localized necking. Based on these, a fourth failure scenario is presented in Figure 1.15.

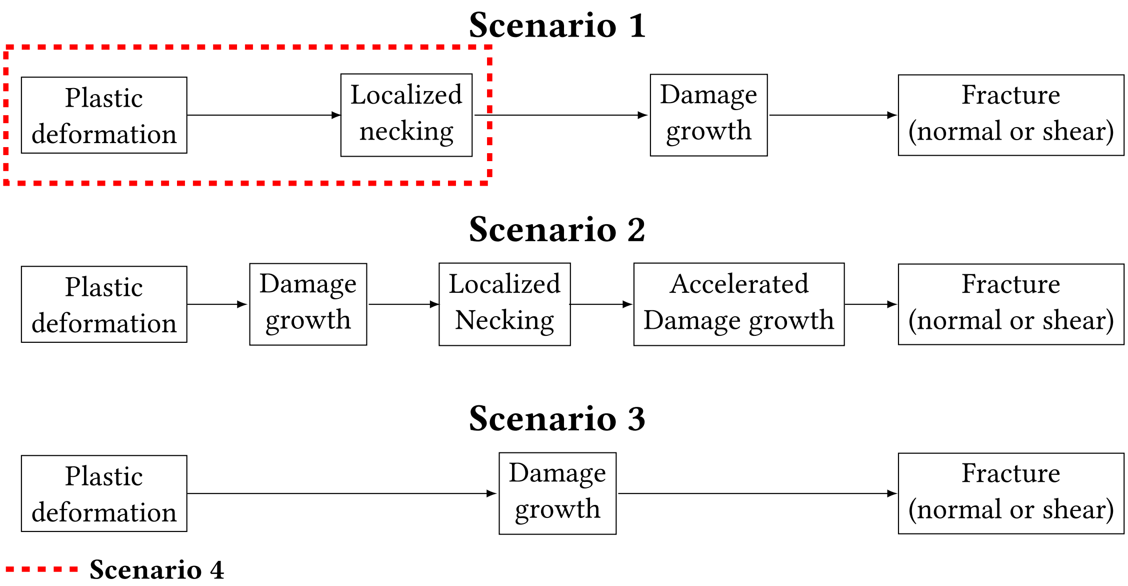

Figure 1.15. Delimitation of the failure scenarios. The illustration is based on Mattiasson et al. (2014).

To reduce the complexity of the yield criterion applied, an assumption of a plane stress state in the specimen/component is made. This assumption apply to the model from the undeformed blank until the specimen reaches the onset of localized necking. Once the point of localized necking has been passed, a three dimensional stress situation must be defined. Another benefit of assuming a plane stress state is, that the Finite Element models then can be created from shell elements instead of solid elements. By applying the shell elements, the computational time of the models is significantly reduced. To obtain as accurate a description of the material behaviour as possible, shell elements with 11 integration points through the thickness will be applied.

1.4 Summary

The introduction had the purpose of describing the motivation for the work presented in this Master Thesis, presenting previous work, define the meaning of the term 'failure', as well as narrow down the scope of the Master Thesis. Table 1.3 presents an outline of the key elements of this chapter.

The Master Thesis will primarily focus on specimens or parts of an AA6016 aluminium alloy.
Through previous work, both the standard Forming Limit Diagram (FLD) and the Non-linear Forming Limit Diagram have been disregarded as suitable general failure prediction approaches for bending-under-tension specimens.
The term 'failure' is, in this report, defined as the onset of localized necking.
Localized necking is assumed to happen before any damage growth occurs in the specimen (See scenario 1 Figure 1.10, or scenario 4 Figure 1.15).
An assumption of a plane stress state in the specimen/component up till the onset of localized necking is made.

Table 1.3. Outline of key elements presented in Chapter 1.

With assumptions and semantics defined, a problem statement can now be created. The forming of the problem statement will take place in Chapter 2.

2 Problem Statement

The previous chapter presented the previous work conducted on the field of research by the author, as well as a definition of the term ’failure’ as localized necking. Furthermore, a thesis delimitation was presented, where it was decided that the primary material of interest for this report is the AA6016 aluminium alloy. Experimental data is available for the three following tests:

- Combined tension and bending test - Punch nose radius 3 mm
- Combined tension and bending test - Punch nose radius 6 mm
- Combined tension and bending test - Punch nose radius 10 mm

Furthermore, a special test die has been developed by Volvo Cars to test the combined bending and tension phenomenon on various punch radii at the same time. Initially, this test die is not the primary focus of the report, but is seen as a good way to validate a potential failure prediction approach found for the aforementioned three tests. Based on these definitions and delimitations, the following problem statement is presented:

"*How can the onset of localized necking accurately be predicted by Finite Element simulation tools for AA6016 aluminium alloy sheets exposed to various cases of combined tension and bending?*"

Having defined the problem statement, the first step towards finding a suitable failure prediction approach, is to investigate the validity of the failure scenario assumption presented in Section 1.3. The investigation of the failure mode will be presented in Chapter 3.

Failure Scenario Investigation 3

In Section 1.2, and again in Section 1.3, an assumption of the specimens fracturing as a result of localized necking was presented. The following chapter aims to either validate or dismiss this assumption using an experimental approach.

3.1 Experimental Approach

The experimental approach used to investigate the failure scenario serves two purposes:

1. Verify that the specimen do in fact experience localized necking prior to fracture.
2. Test the repeatability of the experimental setup.

As in Barlo (2019), the focus is on the intermediate punch nose radius (6 mm). The experiment has initially been repeated five times. The force-displacement curves of the five experiments can be seen in Figure 3.1, and the punch depth at fracture and maximum force level can be found in Table 3.1

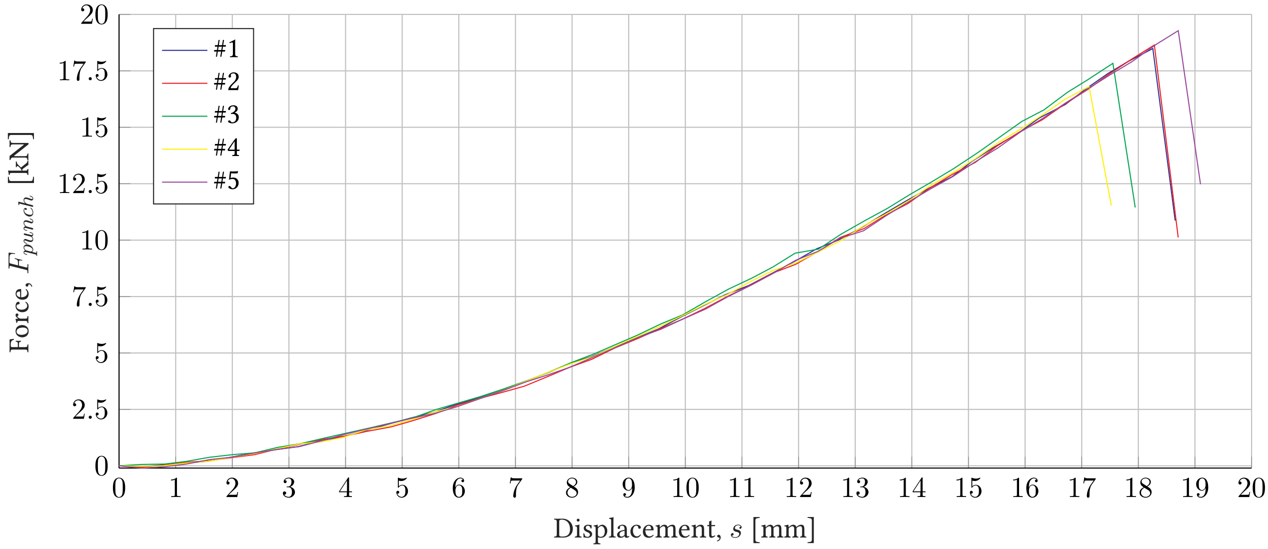

Figure 3.1. Force-displacement curves of the five repeated experiments for the test setup with a punch nose radius of 6 mm.

Experiment #	Max. Punch Force [kN]	Punch Depth [mm]
1	18.488	18.256
2	18.646	18.283
3	17.833	17.551
4	16.801	17.130
5	19.281	18.705

Table 3.1. Max. values of the five repeated experiments.

The data presented in Figure 3.1 shows a good correspondence of the force levels for all five tests. The correspondence between the final punch depth of the different tests does vary. Consulting the data presented in Table 3.1, a difference of approximately 1.5 mm is found between the tests with the largest (test #5) and lowest (test #4) punch depth.

3.2 Detection of Localized Neck in Bending-Under-Tension R6 Specimen

From the data presented in Figure 3.1 and Table 3.1, the repetition with the lowest punch depth (test #4) is used as a reference test for the investigation of the localized neck phenomenon in the specimen. A mechanical stop is created to terminate the test 0.5 mm before fracture. This yields a punch depth of 16.63 mm. From this test, a microscopic examination has been performed on the cross section of the specimen. The result of this examination is presented in Figure 3.2.

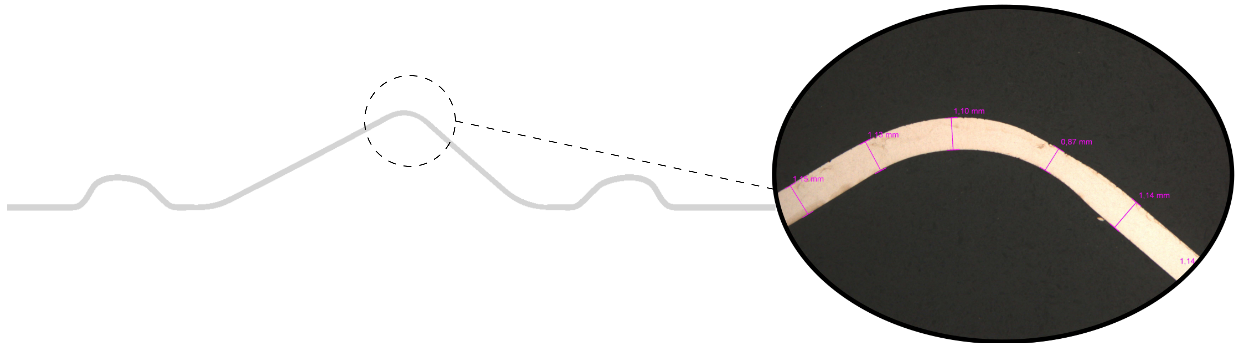

Figure 3.2. Cross section of the specimen from the test terminated 0.5 mm before fracture. Microscopic examination reveals a localized neck in the specimen.

As Figure 3.2 indicates, a localized neck is present in the specimen. This justifies the assumption of the failure scenario presented in Chapter 1, and the failure scenario used will be the one presented in Figure 3.3

Plastic deformaion → Localized necking

Figure 3.3. Failure scenario for the AA6016 aluminium alloy.

Onset of Localized Necking 4

Having verified the assumption presented in Section 1.2, the next step is to identify the exact point where the localized neck is initiated. In order to do so, a strain rate based method, proposed by Sigvant et al. (2008), will be applied. To apply this method, Digital Image Correlation (DIC) measurements of the experiments is required. The following chapter will present the application of the proposed method using the bending-under-tension R6 experiment of an AA6016 aluminium alloy. This experiment has been recorded with the DIC software ARAMIS$^{\text{TM}}$ by GOM.

In simple terms, the method relies on a statistical data set of an area around the location of the fracture. Looking at both the maximum and minimum major strain rate ($\dot{\varepsilon}_{11}$) in this area, it is said that the specimen has reached the onset of localized necking when the maximum and minimum major strain rate values exceeds the predicted major strain rate plus three standard deviations. And illustration of this phenomenon can be found in Figure 4.1.

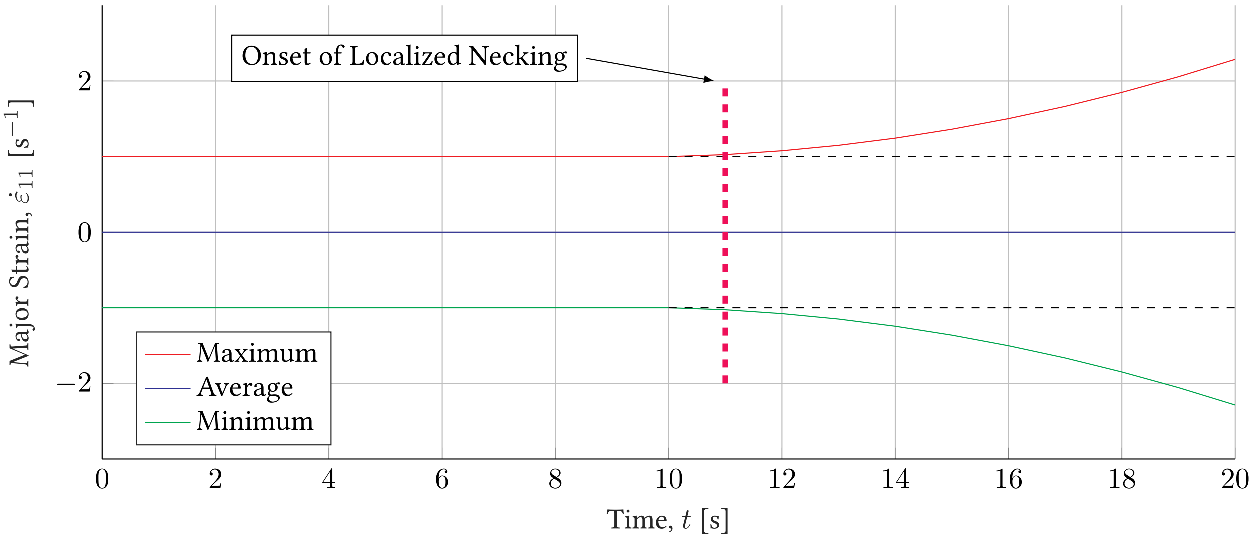

Figure 4.1. Ideal major strain rate development. These data are not experimentally obtained, and only serves the purpose of illustrating the basic concept of the model.

The method can be split into two steps:

1. Defining and extracting the necessary data from ARAMIS$^{\text{TM}}$
2. Run the data iteratively through a MatLab script

The following two sections will present these steps.

4.1 Data Definition and Extraction

The definition and extraction of data is split into four steps to ensure that data is determined at correct stages and locations of the experiment:

1. Identify the solution stage of the maximum punch force
2. Identify the global major strain maximum in the solution stage
3. Define the statistical space of the model
4. Correct data export format

The following subsections will describe the methodology of these four steps.

4.1.1 Identification of Solution Stage and Global Major Strain Maximum

The first step is to determine the point in the experiment, where the maximum punch force for a conforming specimen is present. This point is denoted as the solution stage, where the stage refers to the way ARAMIS^{TM} is set up. ARAMIS^{TM} snaps a series of photos during the operation to perform the strain calculation, and these photos are called strain stages in the software. A strain stage includes the following raw data from the experimental setup:

- Punch Force
- Punch Displacement
- Time
- Blank Holder Force

To define the solution stage, the force-displacement curve, presented in Figure 4.2, is used. The red dashed line indicates the solution stage of the experiment.

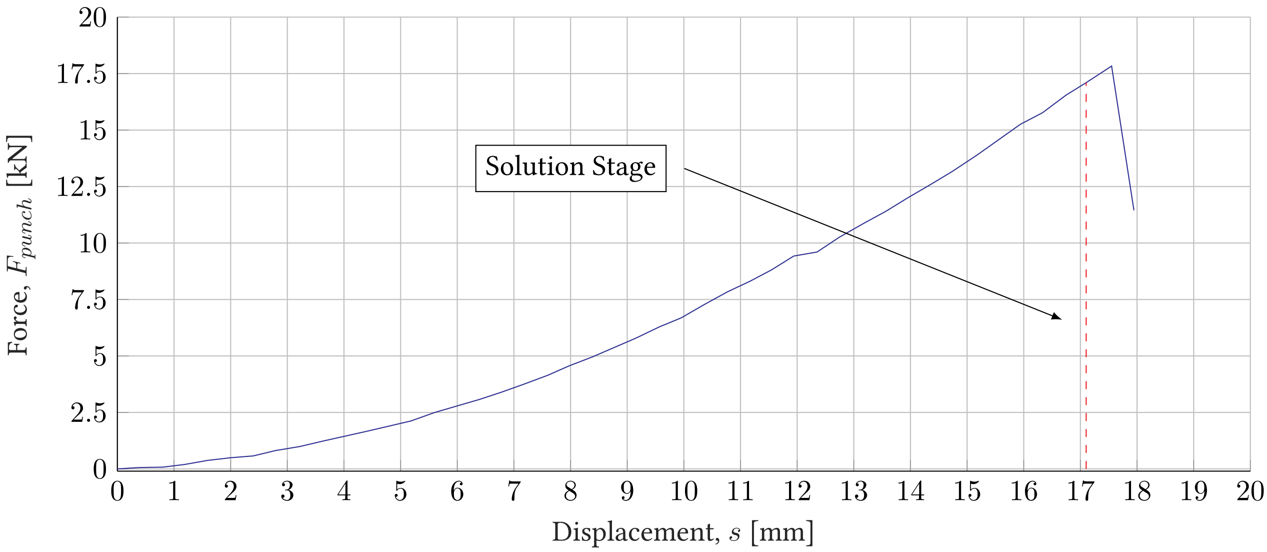

Figure 4.2. Solution stage of the AA6016 aluminium alloy R6 experiment.

As presented in Figure 4.2 the solution stage is not located at the absolute maximum punch force and displacement. The reason for this is presented in Figure 4.3, where a surface defect is visible in the last stage before full fracture. Going one stage back in time (corresponding to 0.449 mm on the force-displacement curve), no surface defects are visible on the specimen (presented in Figure 4.4), why this is chosen as the solution stage.

Having determined the solution stage, the global major strain maximum can be found. This is relatively easy done, using the fringe plot feature available in ARAMIS^{TM}. Figures 4.5 and 4.6 presents these fringe plots with a standard scale and a manipulated scale respectively. Manipulating the scale in such way, that only high strains get separate colors, the global major strain maximum is found as in Figure 4.6, and a marker is pinned to this point. The global major strain maximum is of interest due to the assumption, that this is where the specimen will experience the onset of localized necking. It is possible that fracture

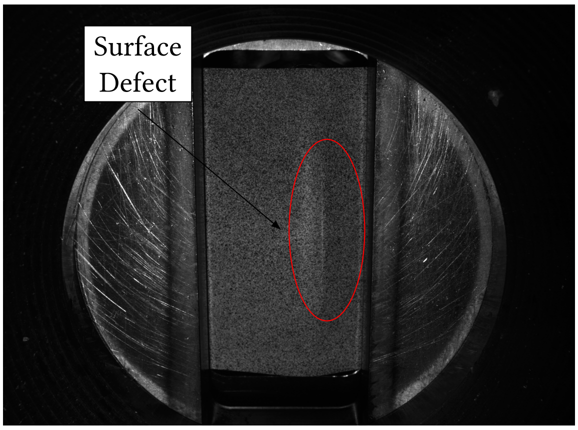

Figure 4.3. Specimen at maximum punch force and depth. A visible surface defect is present in the specimen.

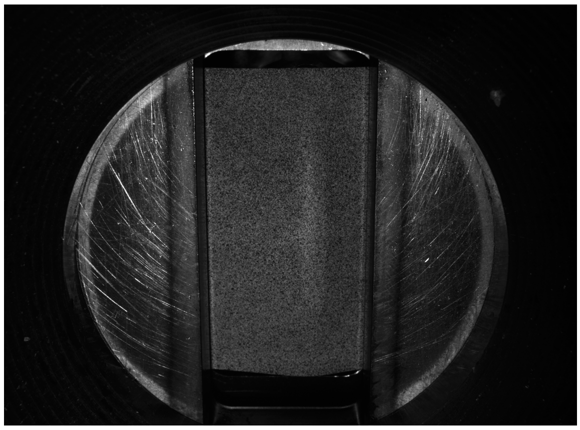

Figure 4.4. Specimen 0.449 mm before maximum punch force and depth. No surface defects visible.

will occur in the draw beads of the experiment before the onset of localized necking, but in that case, the experiment is deemed not valid. Having identified both the solution stage, and the global maximum major strain, a statistical area must now be defined.

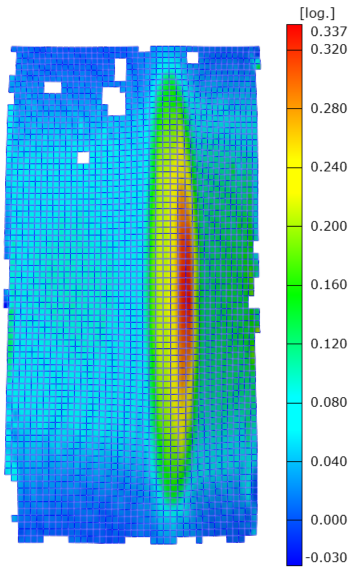

Figure 4.5. Major strain (ε_{11}) fringe plot.

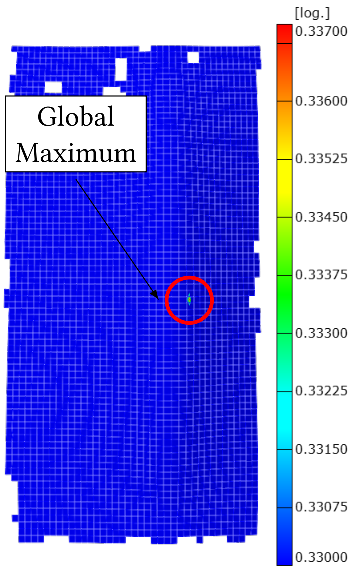

Figure 4.6. Manipulated major strain (ε_{11}) fringe plot.

4.1.2 Defining the Statistical Space of the Model

The method presented by Sigvant et al. (2008) relies on strain rate data found in a statistical area in the measurement. The statistical function in ARAMIS™ provides five parameters when performed. For the case of the major strain rate, these five variables are:

1. Maximum major strain rate ($\dot{\varepsilon}_{11}^{max}$)
2. Minimum major strain rate ($\dot{\varepsilon}_{11}^{min}$)
3. Average major strain rate ($\dot{\varepsilon}_{11}^{avg}$)
4. Standard deviation of the statistical area ($\dot{\varepsilon}_{11}^{sig}$)
5. Number of points included in the statistical area

The size of this statistical area is determined by Sigvant et al. (2008) to be 2x30x100 mm. The center of the 'box' is located in the point of the global major strain maximum previously determined. The statistical area used for the AA6016 aluminium alloy R6 experiment can be seen in Figure 4.7.

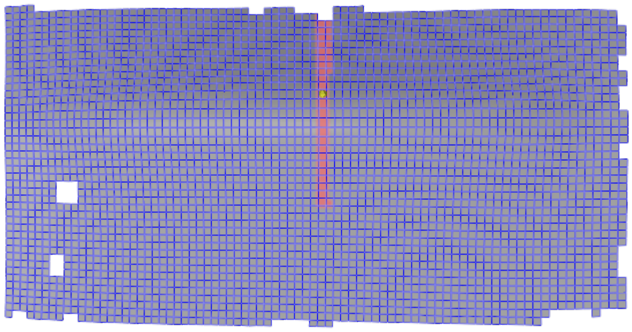

Figure 4.7. Statistical area used for the AA6016 aluminium alloy R6 experiment. The area is highlighted with the red color.

Performing the statistical operation for the elements in the chosen area yields the variables seen in Figure 4.8.

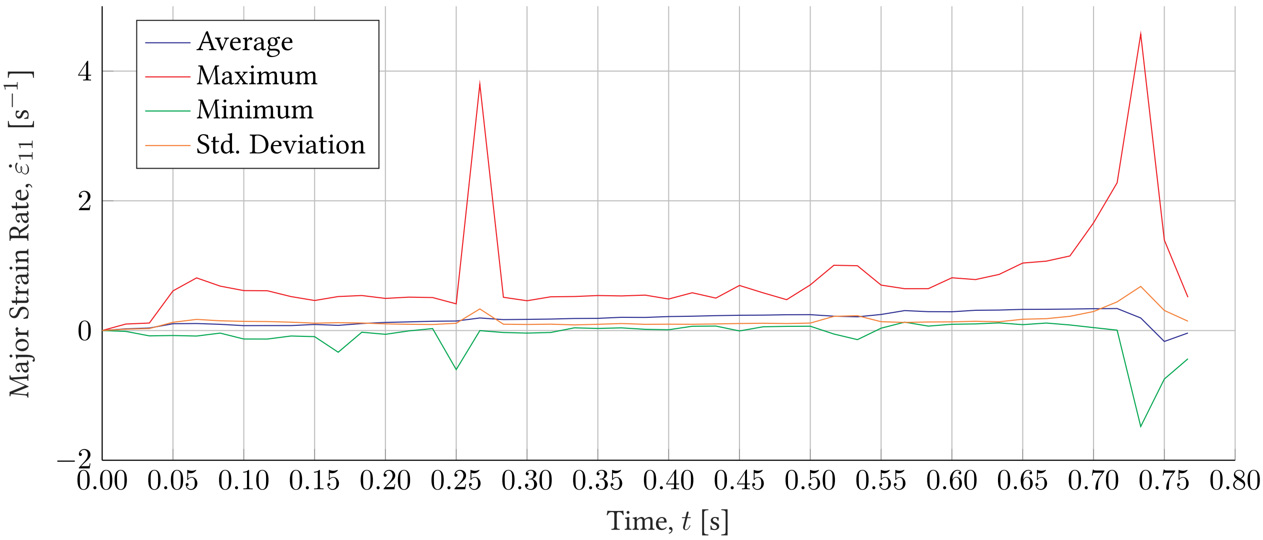

Figure 4.8. Statistical major strain rate as a function of time.

The strain rates obtained from this operation, and presented in Figure 4.8, seems to contain an unacceptable amount of noise. This noise is believe to be caused by the calculation of the strain rate in the 3D strain field using only the previous time value for the differentiation (Equation 4.1).

$$\dot{\varepsilon}_{11,ARAMIS} = \frac{\varepsilon_{11}(t_n) - \varepsilon_{11}(t_{n-1})}{t_n - t_{n-1}} \tag{4.1}$$

In an attempt to reduce the noise in the data, a calculation using both the previous and future point in time (Equation 4.2) is performed on the major strain statistical values.

$$\dot{\varepsilon}_{11} = \frac{\varepsilon_{11}(t_{n+1}) - \varepsilon_{11}(t_{n-1})}{t_{n+1} - t_{n-1}} \tag{4.2}$$

Performing the calculation with both backwards and forwards time points, as well as calculating the strain rate using only the backward time point, Figures 4.9 to 4.11 presents the average, maximum and minimum major strain rates calculated based on the statistical major strain as well as the ARAMIS calculation.

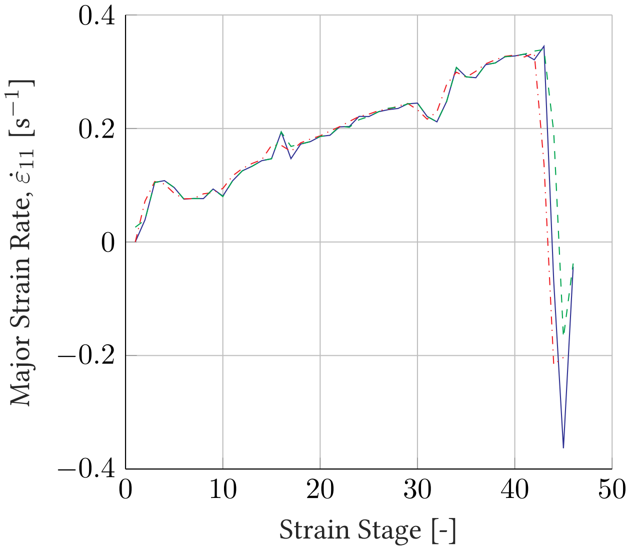

Figure 4.9. Average major strain rate ($\dot{\varepsilon}_{11}^{avg}$).

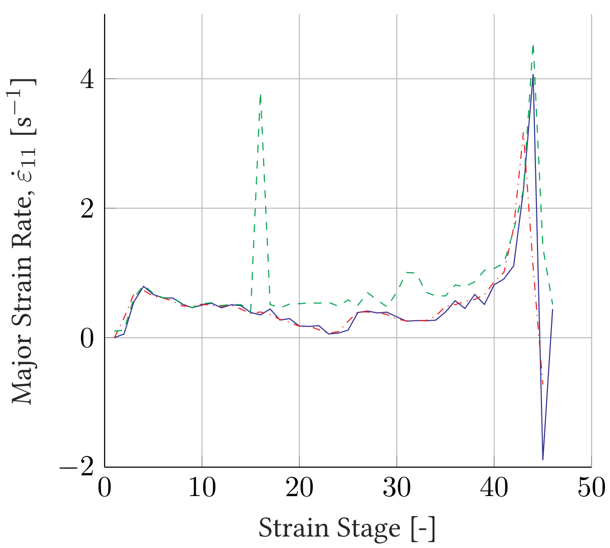

Figure 4.10. Maximum major strain rate ($\dot{\varepsilon}_{11}^{max}$).

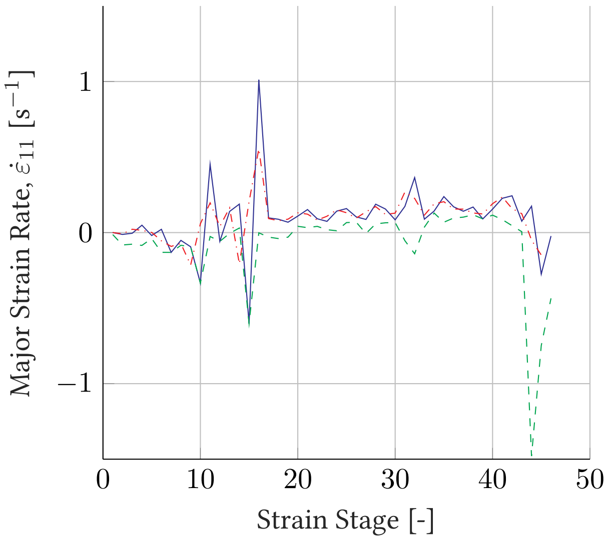

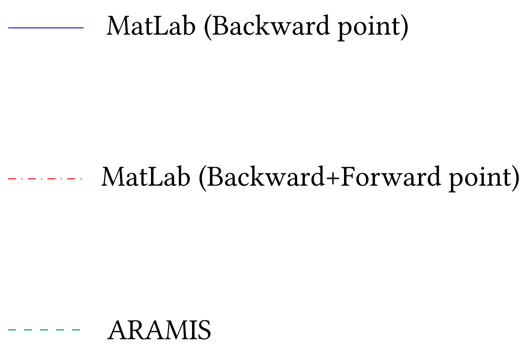

Figure 4.11. Minimum major strain rate ($\dot{\varepsilon}_{11}^{min}$).

Having performed the calculations, it shows that the calculations performed in MatLab for both methods (using the backward point and the backward+forward point) results in a slight reduction of the noise. The largest impact is found in the calculation of the maximum strain rate (Figure 4.10), where the calculations performed outside of ARAMIS^{TM} results in lower strain rates in the area where the onset of localized necking is believed to occur. Based on this, for future determination of the onset of localized necking, the strain rate calculation will be performed outside ARAMIS^{TM} and apply the method using both the backward and forward time points (Equation 4.2).

4.1.3 Correct Data Export Format

Now having determined how the strain rate should be calculated, all data needed for the final determination of the onset of localized necking is defined. The data will therefore be exported in a .txt document, in the following order:

1. Strain Stage [-]
2. Average Major Strain [-]
3. Maximum Major Strain [-]
4. Minimum Major Strain [-]
5. Standard Deviations of the Major Strain [-]
6. Force [kN]
7. Time [s]

A graphical representation of the exported data is presented in Figure 4.12. Having exported these data, it is now possible to determine the onset of localized necking.

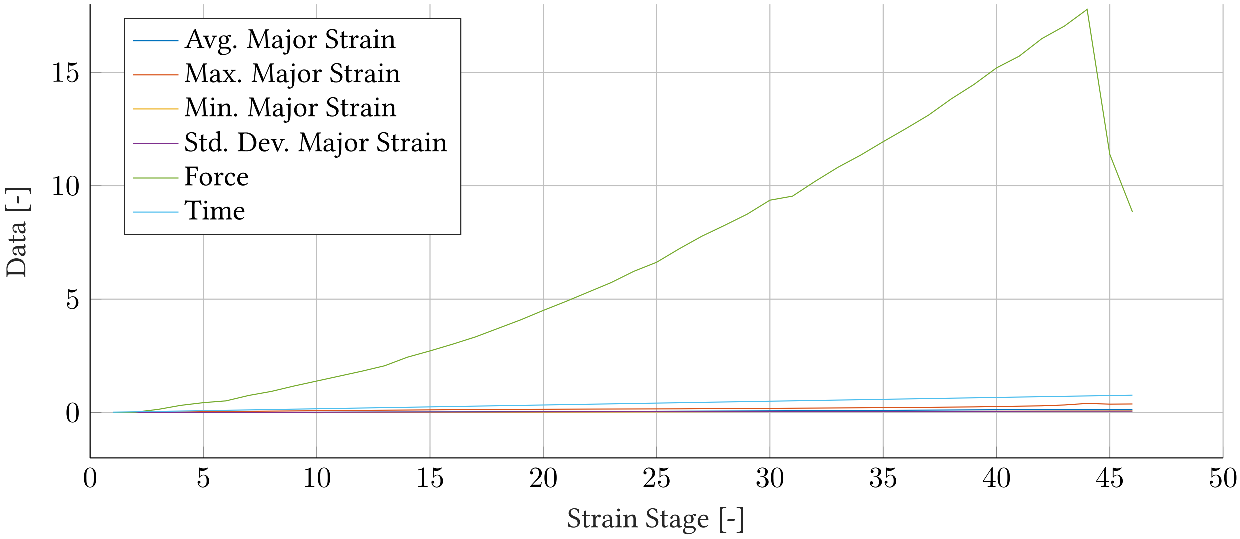

Figure 4.12. Graphical representation of data exported from ARAMIS.

4.2 Determination of the Onset of Localized Necking

Having obtained the necessary data, the MatLab script for determination of the onset of localized necking can now be run. In order to run the script, the user must provide an area of interest, i.e. the strain stages in between which the onset of localized necking is expected to occur. In the case of the bending-under-tension R6 AA6016 aluminium alloy specimen, the initial guess is that this will occur between strain stage 25 and 40.

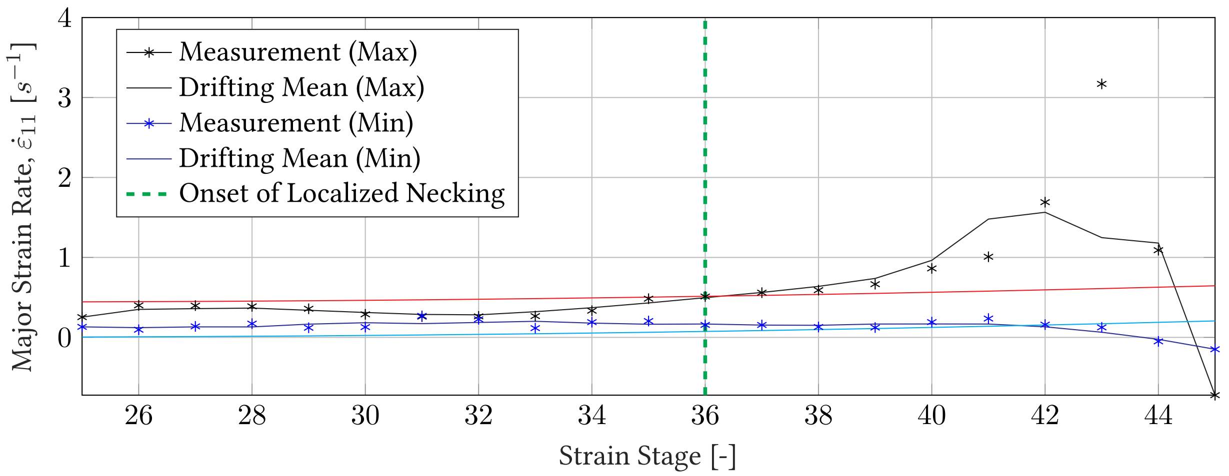

Figure 4.13. Maximum and minimum major strain rates used to determine the onset of localized necking.

Having defined this area of interest, the script generates a figure like the one presented in Figure 4.13. From this figure, the onset of localized necking can be determined. This is done by observing the drifting mean of the minimum and maximum major strain rate. When one of these begin to deviate from the red or cyan coloured line, this is an indication of the onset. The two line described, are the predicted major strain values based on the data points in the area of interest added three times the standard deviation.

In the case of the bending-under-tension R6 AA6016 aluminium alloy specimen, the onset of localized necking occurs at strain stage 36, which corresponds to a punch displacement of roughly 3.5 mm before the surface defect presented in Figure 4.3 occurs.

5 GISSMO Failure Prediction Approach

The GISSMO failure prediction approach was initially proposed by Neukamm et al. (2008) as a method of transferring the damage accumulated in the stamped components into the crash simulations. The abbreviation GISSMO covers the full name *Generalized Incremental Stress State Dependant Damage Model*, and as indicated by the name, the model is based on the stress state rather than the strain state as it is in the standard Forming Limit Diagram and the Non-linear Forming Limit Diagram. The concept of the GISSMO model is to evaluate the damage accumulated in the stamping process using an extended Johnson-Cook damage model, and mapping this to the crash simulation, also evaluating damage using the extended Johnson-Cook damage model. Figure 5.1 illustrates the setup of both the forming and crash simulation, as well as the mapping between the two.

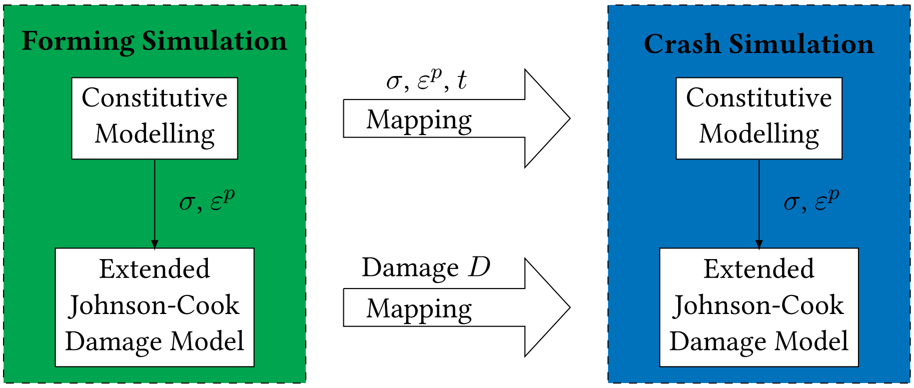

Figure 5.1. Overall concept of the GISSMO model. The illustration is based on Neukamm et al. (2008).

In the original Johnson-Cook damage model, the damage is accumulated as presented in Equation 5.1, and the failure strain defined as presented in Equation 5.2.

$$D = \int \frac{d\varepsilon_e^p}{\varepsilon_f} < 1 \tag{5.1}$$

$$\varepsilon_f = (d_1 + d_2 \cdot \exp(-d_3 \cdot \eta)) \cdot \left[1 + d_4 \cdot \ln\left(\frac{\dot{\varepsilon}_e^p}{\dot{\varepsilon}_0}\right)\right] \tag{5.2}$$

The stress state dependency of the model is defined by the stress triaxiality η, as a part of the failure strain expression. The stress triaxiality is defined as in Equation 5.3.

$$\eta = \frac{\sigma_m}{\overline{\sigma}_{vm}} = -\frac{p}{\overline{\sigma}_{vm}} = \frac{\frac{\sigma_{11}+\sigma_{22}+\sigma_{33}}{3}}{\sqrt{\frac{1}{2} \cdot [(\sigma_{11}+\sigma_{22})^2 + (\sigma_{11}-\sigma_{33})^2 + (\sigma_{22}-\sigma_{33})^2]}} \tag{5.3}$$

As presented, the stress triaxiality is a ratio between the hydrostatic pressure and the von Mises equivalent stress. The hydrostatic pressure can be determined by splitting the stress tensor $\boldsymbol{\sigma}$ into two parts; the deviatoric stress tensor $\boldsymbol{s}$ and the hydrostatic pressure p.

$$\boldsymbol{\sigma} = \boldsymbol{s} + \frac{1}{3} \cdot \mathrm{tr}(\boldsymbol{\sigma}) \cdot \boldsymbol{I} \tag{5.4}$$

where

$$\frac{1}{3} \cdot \mathrm{tr}(\boldsymbol{\sigma}) \cdot \boldsymbol{I} = \frac{1}{3} \cdot \sigma_{kk} = -p \quad \text{and} \quad \boldsymbol{s} = \boldsymbol{\sigma} - \left(\frac{1}{3} \cdot \sigma_{kk} \cdot \boldsymbol{I}\right) \tag{5.5}$$

The two parts of the stress tensor describes two different areas of concern:

- The hydrostatic pressure describes change in volume.
- The deviatoric stress describes change in shape.

For this model, a new understanding of the term 'damage', that differs from the one presented in Section 1.2, is adopted. For the failure prediction associated to the GISSMO approach, the term damage is defined as the severity of the material degradation. This means, when the failure variable F reaches unity, an accelerated localized straining of the specimen will occur up until the point of fracture. The expression describing the failure F is presented in Equation 5.6.

$$F = \left(\frac{\varepsilon^p}{\varepsilon_{crit}(\eta)}\right)^n \tag{5.6}$$

Differentiating Equation 5.6 with respect to time, the following expression for the failure is found:

$$\dot{F} = \frac{n}{\varepsilon_{crit}(\eta)} \cdot F^{(1-1/n)} \cdot \dot{\varepsilon}^p \tag{5.7}$$

Equations 5.6 and 5.7 are only valid until the failure has reached unity, indicating the onset of localized necking. As previously mentioned, when this point have been passed, the material degradation becomes severe, and the damage must be coupled to the stress tensor:

$$\boldsymbol{\sigma} = (1 - \tilde{D}) \cdot \tilde{\boldsymbol{\sigma}} \tag{5.8}$$

where $\tilde{\boldsymbol{\sigma}}$ is the undamaged stress tensor, and $\tilde{D}$ is defined as:

$$\tilde{D} = \begin{cases} 0, & \text{if} \quad F < 1 \\ \left(\frac{D - D_{crit}}{1 - D_{crit}}\right)^m, & \text{if} \quad F \geq 1 \end{cases} \tag{5.9}$$

where D_{crit} is the damage accumulated when F reaches unity, m is a fading exponent, and D is defined as:

$$D = \left(\frac{\varepsilon^p}{\varepsilon_f(\eta)}\right)^n \tag{5.10}$$

5.1 Failure Model Delimitation

In Section 1.2 it was defined, that failure handled in this report is defined as the onset of localized necking, and in Chapter 3 it was presented, that a localized neck occurs before fracture. Having defined the failure in this way, only a part of the theory presented above is needed. In order to reduce causes for confusion, talking about failure damage F and fracture damage D, the general term damage will be used, and denoted

D. Only looking at the damage accumulated up to the onset of localized necking, the failure model becomes simpler, and defined in the following way:

$$D = \left(\frac{\varepsilon^p}{\epsilon_f(\eta)} \right)^n \tag{5.11}$$

and

$$\dot{D} = \frac{n}{\varepsilon_f(\eta)} \cdot D^{(1-1/n)} \cdot \dot{\varepsilon}^p \tag{5.12}$$

Having defined the range the failure prediction approach will operate in, the next step is to defined the failure strain ε_f.

5.2 Failure Strain Determination

The GISSMO failure prediction approach operates in the stress triaxiality space, where the equivalent plastic strain $\bar{\varepsilon}^p$ is evaluated as a function of the stress triaxiality η. The industry standard Forming Limit Diagram operates in the principal strain space (strain-strain based), but evaluating the damage using the GISSMO model, the evaluation is stress-strain based. In the original Johnson-Cook failure model, the failure strain is defined as in Equation 5.2, which results in a monotonically decreasing function of the triaxiality. In the work presented by Neukamm et al. (2008), it is presented that the minimum failure strain will occur at plane strain conditions, why the shape of the failure strain curve $\varepsilon_f(\eta)$ should differ from the one used in the Johnson-Cook model.

As the standard Forming Limit Diagram has been the industry standard since it was presented in the pioneering work by Keeler & Backofen (1964), the idea of using the principal strains for formability evaluation, is something that has been deeply lodged into the minds of the stamping community. In order to ease the transition to using a new way to evaluate formability, a method of determining the failure strain curve $\varepsilon_f(\eta)$ by transforming the standard Forming Limit Curve (FLC) is used.

The failure strain in the stress triaxiality space covers, like the FLC, a variety of load scenarios, why the failure strain $\varepsilon_f(\eta)$ can be investigated in four different regions (Gorji 2015):

Between uniaxial compression ① and pure shear ②	$-\frac{1}{3} < \eta < 0$
Between pure shear ② and uniaxial tension ③	$0 < \eta < \frac{1}{3}$
Between uniaxial tension ③ and plane strain ④	$\frac{1}{3} < \eta < \frac{1}{\sqrt{3}}$
Between plane strain ④ and equibiaxial tension ⑤	$\frac{1}{\sqrt{3}} < \eta < \frac{2}{3}$

The above mentioned load scenarios for the triaxiality space is illustrated in Figure 5.2, and the corresponding load scenarios in the principal strain space is illustrated in Figure 5.3.

The triaxiality values presented for the different load scenarios in Figure 5.2 is only valid under the assumptions of an isotropic material model and plane stress condition. This can be visualised by expressing the triaxiality as a function of the relationship between the principal stresses denoted k. By assuming plane stress, the following relationship between the principal stresses ($\sigma_{33} = 0$) can be created,

$$\boldsymbol{\sigma} = \begin{bmatrix} \sigma_{11} & 0 & 0 \\ 0 & \sigma_{22} & 0 \\ 0 & 0 & 0 \end{bmatrix} = \begin{bmatrix} \sigma_{11} & 0 & 0 \\ 0 & k \cdot \sigma_{11} & 0 \\ 0 & 0 & 0 \end{bmatrix} \tag{5.13}$$

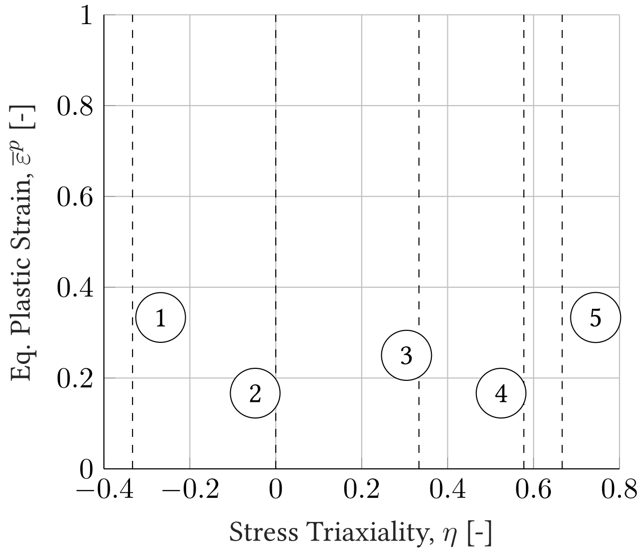

Figure 5.2. Load scenarios in the stress triaxiality space. The illustration is based on Gorji (2015).

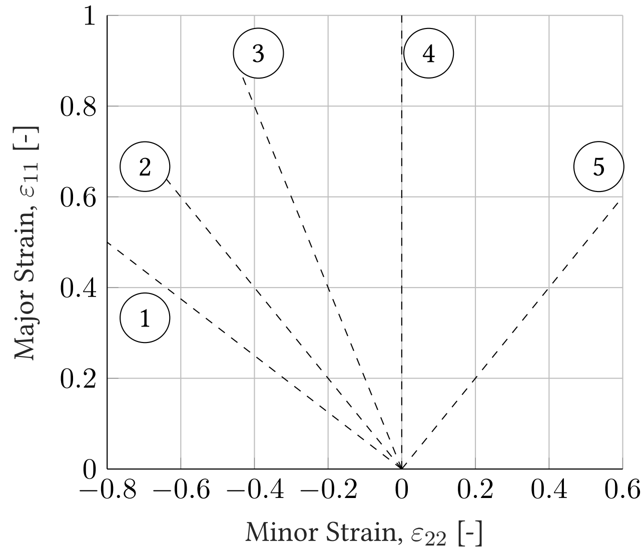

Figure 5.3. Corresponding load scenarios in the principal strain space.

and the stress triaxiality as a function of k can be expressed as:

$$\eta(k) = \frac{1+k}{3 \cdot \sqrt{1+(k-1) \cdot k}} \cdot \operatorname{sgn}(\sigma_{11}) \tag{5.14}$$

To ease the understanding of the parameter ks influence on the stress triaxiality, this is graphically illustrated in Figure 5.4 (Andrade et al. 2016).

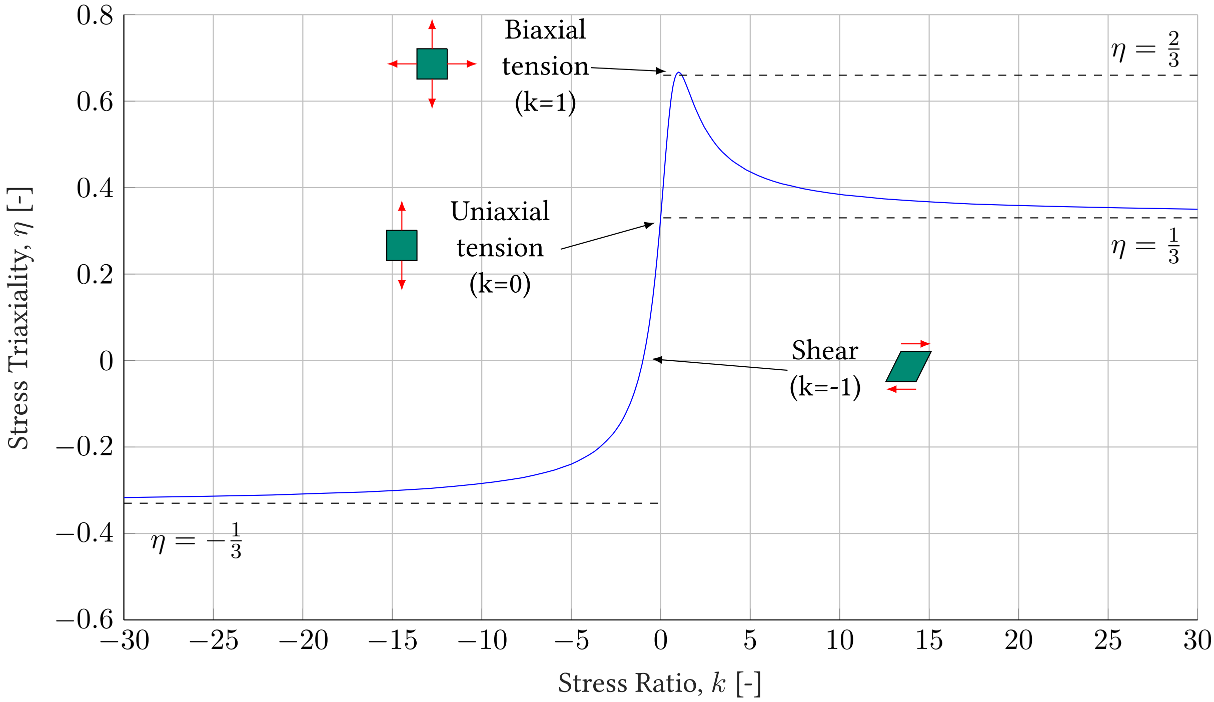

Figure 5.4. Stress triaxiality as a function of the stress ratio k for positive values of σ_{11}. The illustration is based on Andrade et al. (2016).

Having defined the stress triaxiality space, an attempt to couple the principal strain space and the stress triaxiality space will be performed using the isotropic von Mises material model.

5.2.1 von Mises based Limit Curve Transformation

An initial attempt to create a transformation of the FLC is made, based on the von Mises constitutive equations. It is a well know fact within the stamping community, that the von Mises constitutive equations performs very poorly. However, due to the simplicity of the constitutive equations, a von Mises based approach is tested to ease the transformation. What is desired is to perform the transformation presented in Figure 5.5, mapping the FLC from the principal strain space to the stress triaxiality space. To perform this transformation, three assumptions are made:

Linear deformation:	$d\boldsymbol{\varepsilon} = \boldsymbol{\varepsilon}$
Associated flow rule:	$d\boldsymbol{\varepsilon} = d\bar{\varepsilon}^p \cdot \frac{d\bar{\sigma}}{d\boldsymbol{\sigma}}$
von Mises yield locus:	$\bar{\sigma} = \sqrt{\sigma_{11}^2 - \sigma_{11} \cdot \sigma_{22} + \sigma_{22}^2}$

With these assumptions, the following transformation equations can be derived:

$$\eta = \frac{2 \cdot (\varepsilon_{11} + \varepsilon_{22})}{3 \cdot \bar{\varepsilon}^p} \tag{5.15}$$

$$\bar{\varepsilon}^p = \sqrt{\frac{4}{3} \cdot (\varepsilon_{11}^2 + \varepsilon_{22}^2 + \varepsilon_{11} \cdot \varepsilon_{22})} \tag{5.16}$$

The full derivation of Equations 5.15 and 5.16 can be found in Appendix A.

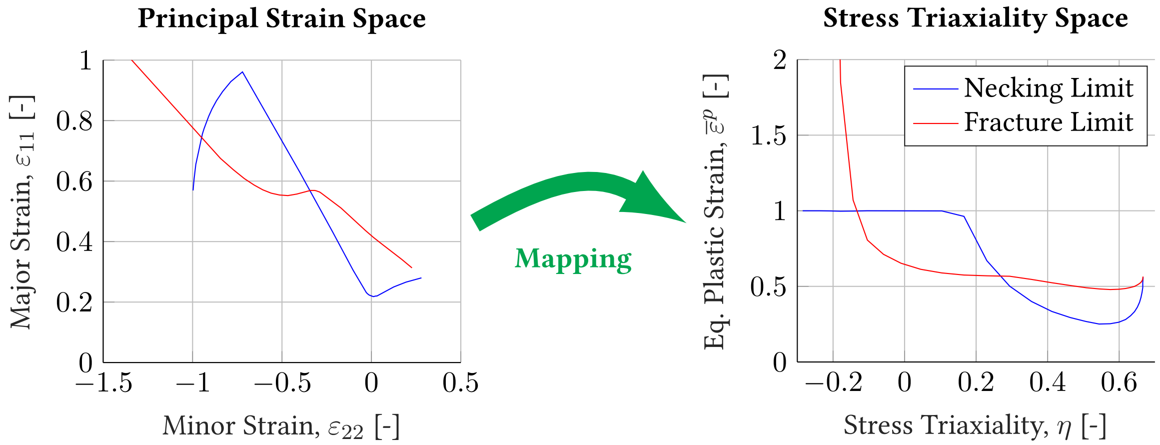

Figure 5.5. Illustration of the mapping from the principal strain space to the stress triaxiality space. The limit curves in the principal strain space used for the illustration have been provided by Dr. Niko Manopulo from AutoForm Engineering GmbH.

5.3 Strain Field Transformation

Just as the limit curve has been transformed from the principal strain space to the stress triaxiality space, this is also necessary for the strain field. When talking about the strain field rather than the limit curves, the material model of choice suddenly becomes even more important, as this directly influences the principal strain values. Figure 5.6 presents the strain field of a bending-under-tension R6 AA6016 aluminium alloy specimen, simulated with both the von Mises and BBC05 constitutive model at an arbitrary point in time.

A transformation of the two strain fields is performed following the flow presented in Figure 5.7, and a comparison of the von Mises and BBC05 based strain fields is presented in Figure 5.8.

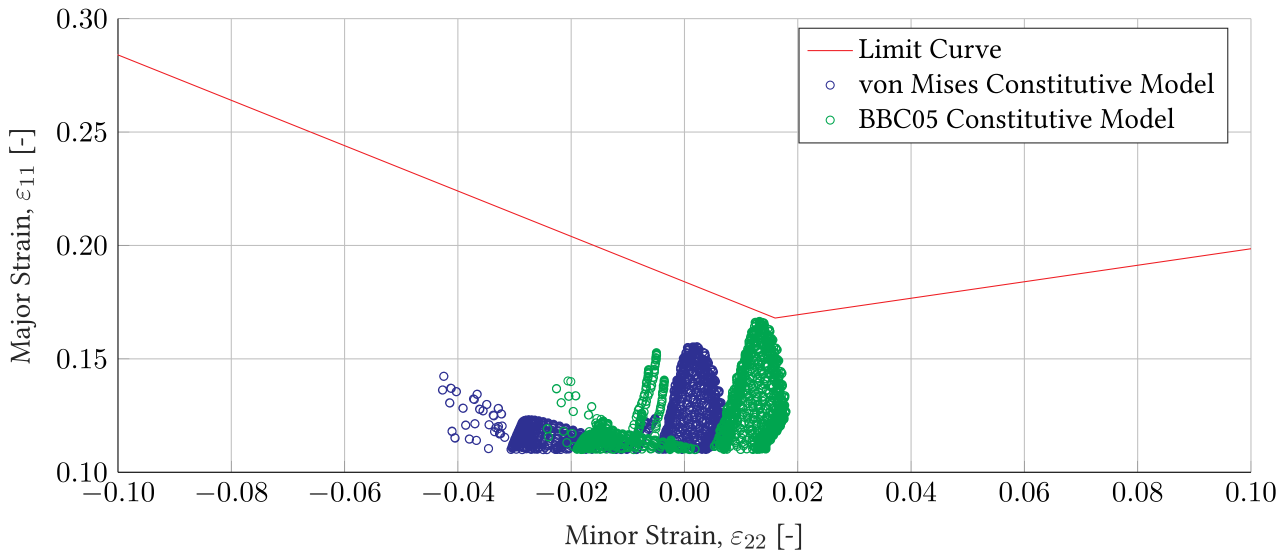

Figure 5.6. Strain fields of the bending-under-tension R6 AA6016 aluminium alloy specimen simulated with two different constitutive models. Only major strain values above 0.11 have been included to reduce computational cost for future calculations.

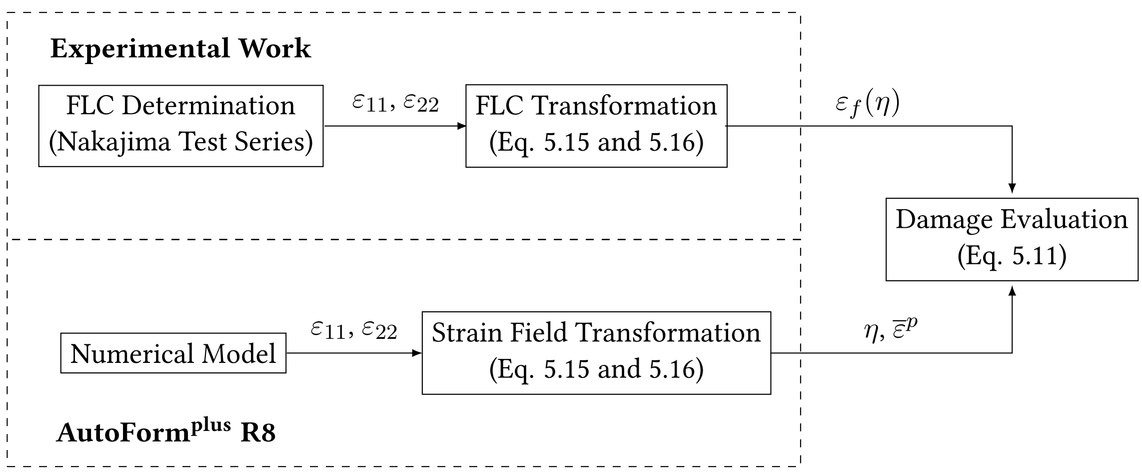

Figure 5.7. Flow of the strain based von Mises damage evaluation approach.

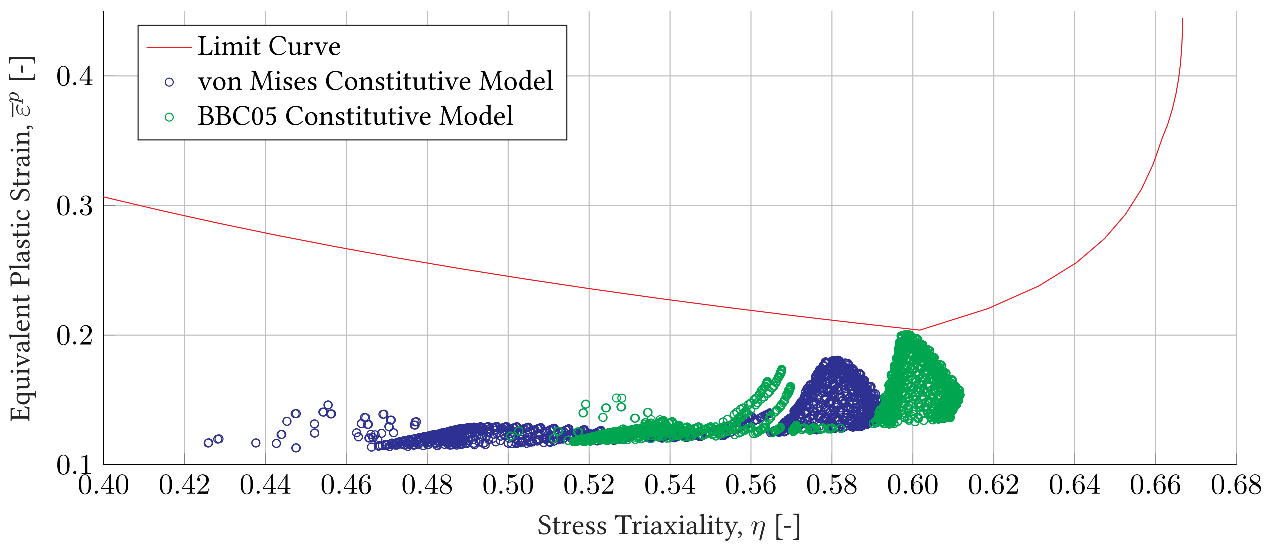

Figure 5.8. Strain fields presented in Figure 5.6 transformed into the stress triaxiality space using von Mises based transformation equations.

A difference is seen between the peak equivalent plastic strain values of the two constitutive models, as well as a difference in the triaxiality values. Having observed this difference, an attempt to perform a BBC based transformation will be presented.

5.3.1 BBC based Strain Field Transformation

As previously mentioned, it is a well known fact that the von Mises constitutive model performs poorly. Due to this knowledge the author finds it necessary to see if the choice of constitutive model for the transformation influences said transformation in the same way it influences the determination of strain fields.

Unlike the transformation of both the limit curve and the strain field using the von Mises constitutive model, the same operation using the BBC05 constitutive model can not be expressed explicitly. Instead, the method involves several implicit solutions considering the yield locus, the flow curve, and their derivatives. Equation 5.17 presents the expression for calculating the BBC05 equivalent stress.

$$\overline{\sigma} = \left[a \cdot (\Lambda + \Gamma)^M + a \cdot (\Lambda - \Gamma)^M + b \cdot (\Lambda - \Psi)^M + b \cdot (\Lambda - \Psi)^M\right]^{\frac{1}{M}} \tag{5.17}$$

where,

$$\begin{aligned} \Gamma &= J \cdot \sigma_{11} + L \cdot \sigma_{22} \\ \Lambda &= \sqrt{(N \cdot \sigma_{11} - P \cdot \sigma_{22})^2 + \sigma_{12} \cdot \sigma_{21}} \\ \Psi &= \sqrt{(Q \cdot \sigma_{11} - R \cdot \sigma_{22})^2 + \sigma_{12} \cdot \sigma_{21}} \end{aligned} \tag{5.18}$$

Here, parameters a, b, J, L, N, P, Q, and R must be identified through an extensive procedure presented in Banabic (2010).

It is therefore not a trivial task to perform the transformation from the principal strain space to the stress triaxiality space based on the BBC05 constitutive model. In order to resolve this issue, the author has engaged in extensive discussions with Dr. Niko Manopulo from AutoForm Engineering GmbH. Dr. Manopulo has made a script to perform the transformation, based on the work by (Gorji 2015, Section 5.2.1), why a transformation between the two spaces has been possible. The transformation is performed using Algorithm 1 in Appendix B

Figure 5.9 presents a comparison between the von Mises and BBC05 based transformations of the strain field generated from the numerical model using the BBC05 constitutive model. At first glance, i looks like there is no big difference in the strain fields in relation to their respective limit curves. This indicates, that the transformation from the principal strain space to the stress triaxiality space can be decoupled from the constitutive model used for the numerical simulation. However, in order to be sure that is the case, the damage D is calculated based on the two transformation methods. A more detailed description of the damage calculation will be presented in Section 5.4. The maximum damage calculated based on the two transformation approaches can be found in Figure 5.10.

As presented in Figure 5.10, the maximum damage values calculated for the two different approaches does not differ very much in terms of damage, but does deviate in terms of what level of plastic straining it occurs at. The actual values of the maximum damage, and the plastic strain levels they occur at, can be found in Table 5.1.

Based on these findings, it is concluded that the transformation from the principal strain space to the stress triaxiality space can be decoupled from the constitutive model used for the numerical simulation. This conclusion is drawn since only a negligible difference in the maximum damage calculation is observed.

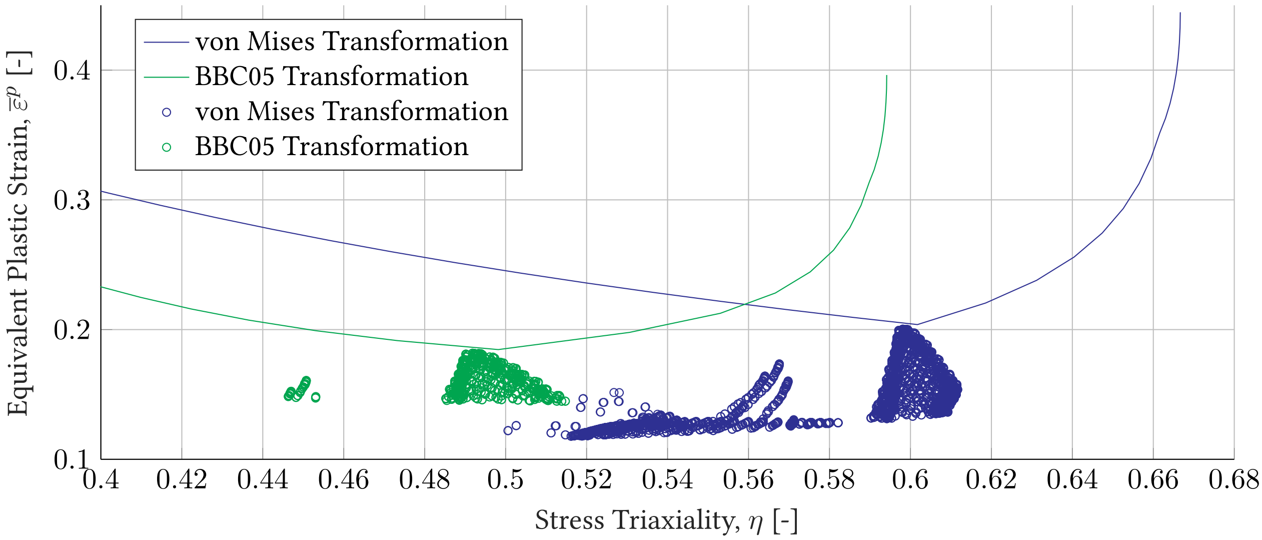

Figure 5.9. Comparison of performance for the space transformation based on von Mises and BBC05 constitutive models. The strain field is generated from the numerical model using the BBC05 constitutive model.

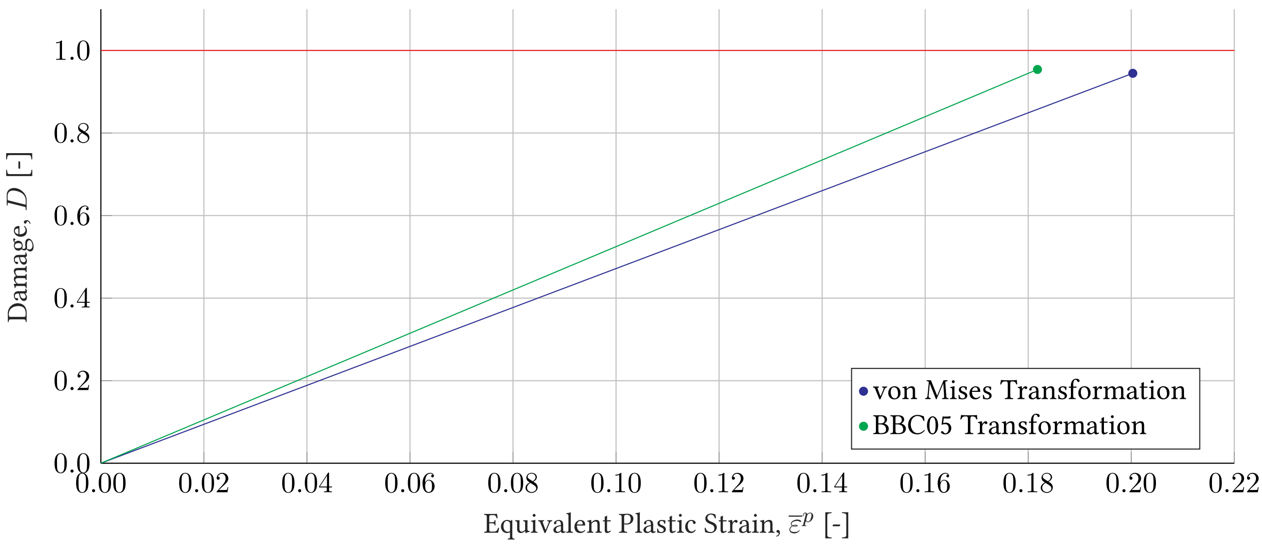

Figure 5.10. Comparison of maximum damage calculated from the two strain fields presented in Figure 5.9.

Constitutive Model	**Maximum Damage**	**Equivalent Plastic Strain**
von Mises	0.9446	0.2003
BBC05	0.9534	0.1818
Difference	0.0088	0.0185

Table 5.1. Difference between the calculated maximum damage and the plastic strain levels they occur at for the two transformation approaches.

5.4 Damage Evaluation

Having determined the way the transformation of the limit curve and strain field should be performed, the next step is to defined the way the damage is calculated. In Section 5.1, the damage calculation was limited to be described as only a relationship between the equivalent plastic strain and the failure strain (Equation 5.11) and a incremental damage evolution model (Equation 5.12).

A part of the GISSMO model is to choose what damage exponent n will be applied. In the work presented in this report, the model is simplified so the damage exponent $n = 1$. This simplifies the model in a way, that the damage D can be seen as a direct measure of how far the equivalent plastic strain is from passing the limit strain, for the given load scenario. This simplification also results in a computational benefit. By choosing the damage exponent $n = 1$, the number of equations to compute per element is reduced by one, since $\dot{D}$ becomes equal to D. This is proven in Equations 5.19 and 5.20.

$$\begin{aligned} \dot{D} &= \frac{n}{\varepsilon_f(\eta)} \cdot D^{1-(1/n)} \cdot \dot{\varepsilon}^p \\ &= \frac{1}{\varepsilon_f(\eta)} \cdot D^0 \cdot \dot{\varepsilon}^p \\ &= \int \frac{\dot{\varepsilon}^p}{\varepsilon_f(\eta)} dt \\ &= \frac{\overline{\varepsilon}^p}{\varepsilon_f(\eta)} \end{aligned} \tag{5.19}$$

$$\begin{aligned} D &= \left(\frac{\overline{\varepsilon}^p}{\varepsilon_f(\eta)}\right)^n \\ &= \left(\frac{\overline{\varepsilon}^p}{\varepsilon_f(\eta)}\right)^1 \\ &= \frac{\overline{\varepsilon}^p}{\varepsilon_f(\eta)} \end{aligned} \tag{5.20}$$

$$\because n = 1 \qquad \therefore \dot{D} = D \qquad \square$$

This also means, that the model no longer necessarily is defined as only the GISSMO approach, but also has a strong resemblance to the linear Johnson-Cook damage criterion presented in Equation 5.1. The only difference between these two, is how the failure strain is defined.

In the work presented in this report, the damage model is based on an incremental maximum. By tracking one element throughout the forming operation, it can be seen that the stress triaxiality values does not stay the same for the entire operation as illustrated in Figure 5.11. This causes the element to move along the x-axis in the triaxiality - equivalent plastic strain space and changing the limit strain value. Figure 5.12 presents an arbitrary strain path in the stress triaxiality space. In the presented strain path, the stress triaxiality value increases during the operation, why the different increments will have different damage values. As the damage calculation is described as the direct relationship between the equivalent plastic strain and the failure strain value, the maximum will for the case presented in Figure 5.12 occur in the second last increment.

Having presented the foundation of the GISSMO method, this is now ready to be used with actual limit curves and test specimens of various punch radii. Before moving on to the failure curve determination, a short summary of the key elements and decisions in the GISSMO approach will be presented.

5.5 Summary

The following section will present a brief summary of the key elements and decisions presented in the explanation of the GISSMO failure prediction approach.

Initially, in Section 5.1, the GISSMO model was limited to predict the onset of localized necking yielding the damage calculation to be performed using Equations 5.11 and 5.12. That meant that the GISSMO approach was decoupled from the stress tensor, as this is only necessary when predicting fracture (Andrade et al.

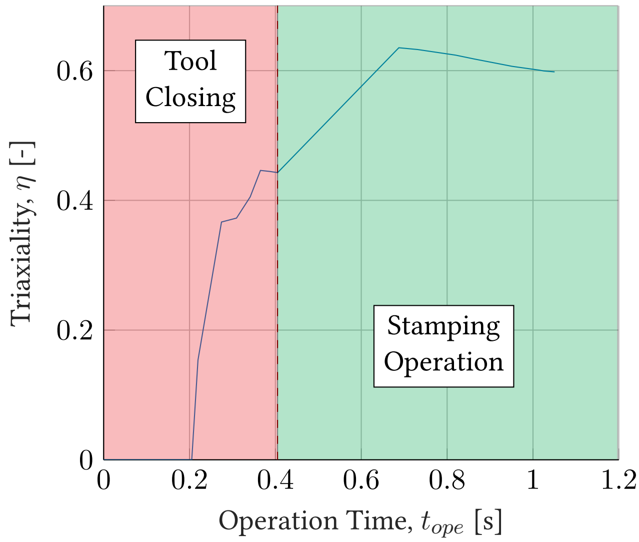

Figure 5.11. Stress triaxiality as a function of the operation time. The triaxiality values displayed is for the numerical simulation of the bending-under-tension R6 AA6016 aluminium alloy specimen using the BBC05 constitutive model.

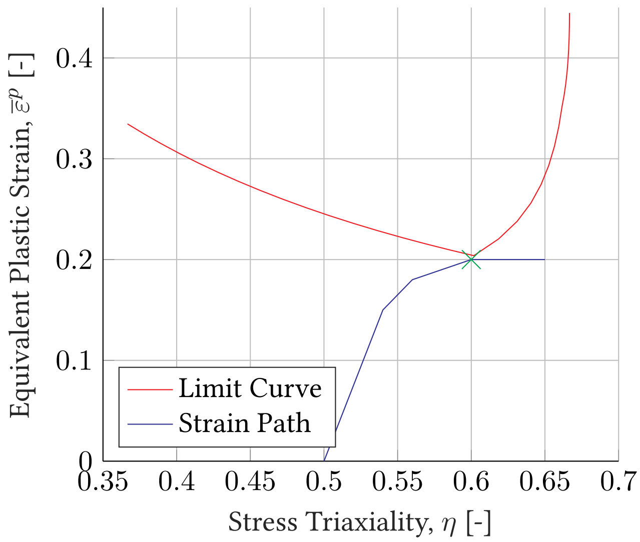

Figure 5.12. Arbitrary strain path illustrating the concept of maximum damage.

2016). Furthermore, in order to simplify the damage model, the damage exponent n was chosen to be 1, thereby yielding the damage as a direct relationship between the equivalent plastic strain and the failure strain. With this choice, the calculation of the damage is defined in the following way

$$D = \frac{\bar{\varepsilon}^p}{\varepsilon_f(\eta)} \tag{5.21}$$

In order to determine the limit curve and strain field in the stress triaxiality space, transformations from the principal strain space to the stress triaxiality space was performed using both the BBC05 and von Mises constitutive models. Observing only a negligible difference in the calculated damage of 0.0088, the von Mises transformation is decided to be used, as this transformation can be expressed explicitly in the following way

$$\bar{\varepsilon}^p = \sqrt{\frac{4}{3} \cdot (\varepsilon_{11}^2 + \varepsilon_{22}^2 + \varepsilon_{11} \cdot \varepsilon_{22})} \qquad \text{and} \qquad \eta = \frac{2 \cdot (\varepsilon_{11} + \varepsilon_{22})}{3 \cdot \bar{\varepsilon}^p} \tag{5.22}$$

Lastly, the concept of maximum damage was presented. Here it was defined, that the damage value for the operation should be the highest one present, and not the damage value in the final stage of the numerical simulation.

Limit Curve Determination 6

As previously mentioned, the Forming Limit Diagram (FLD) has been the industry standard since introduced by Keeler & Backofen (1964) more than half a century ago. Therefore, a great knowledge of how to create the Forming Limit Curves (FLC) has over the years been obtained. Two test methods are standardized for the purpose:

1. The Nakajima Test
2. The Marciniak Test

The main difference between the two methods is the Nakajima test uses a hemispherical punch with a punch nose radius of 50 mm, where the Marciniak test uses a flat headed punch and a carrier blank. In the material testing routine at Volvo Cars, the Nakajima test is used, why results presented in this chapter will be obtained using this approach. A more extensive description of the setup used for the testing can be found in (Barlo 2019, Section 3.2.3). The following chapter will present the methodology used for the determination of FLCs, and will use the determination of the necking curve for the AA6016 aluminium alloy as an example.

6.1 Experimental Approach and Data Retrieval

For the creation of the FLC at Volvo Cars, seven different blank geometries are used. A basic round blank with the width of 200 mm (biaxial strain path condition) is modified with cut-outs to depict different strain path conditions. An example of a blank with cut-outs can be found in Figure 6.1, and the seven applied blank widths can be found in Table 6.1.

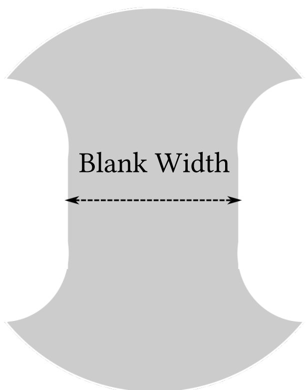

Figure 6.1. Illustration of the Nakajima test blank width.

Nakajima Blank Widths [mm]						
25	50	75	100	125	150	200

Table 6.1. Blank width used at Volvo Cars for the determination of the standard Forming Limit Diagram (FLD) using the Nakajima test method.

The testing of the Nakajima blank is recorded with the Digital Image Correlation (DIC) software ARAMIS$^{\mathrm{TM}}$ to allow for the strain history analysis necessary to determine not only fracture curves but also necking curves. For the case presented in this chapter, the methodology presented in Chapter 4 is used to determine the onset of necking for each blank width. The applied DIC software incorporates a 'FLC mode' feature, allowing for the creating of FLC reports for each sample. Figure 6.2 presents a measurement of a 200 mm Nakajima blank after deformation. On each measurement, three sections are defined for the FLC report to avoid global major strain outliers. An example of a FLC report for the 200 mm Nakajima blank is presented in Figure 6.3.

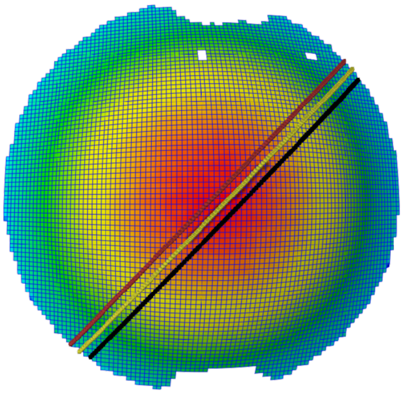

Figure 6.2. Sections defined for the AA6016 aluminium 200 mm Nakajima blank. Three sections are defined in order to secure that results are not outliers.

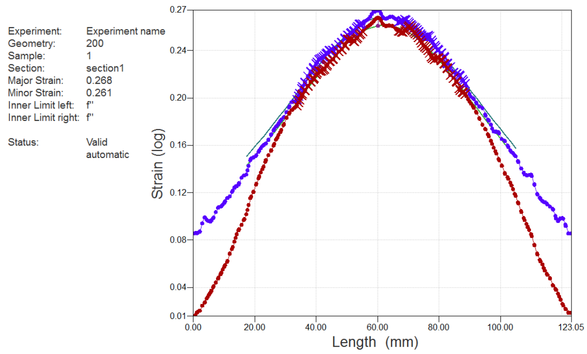

Figure 6.3. ARAMIS™ FLC report. The y-axis represents the major strain ε_{11}, and the x-axis represents the length of the aforementioned sections defined on the specimen. The presented example is taken from the Nakajima specimen presented in Figure 6.2.

Performing this analysis for all blank widths, the major-minor strain pairs are plotted in the FLD, and a curve is created from these. Figure 6.4 presents the measured strain pairs and the initial necking curve for the AA6016 aluminium alloy. For each blank width, three strain pairs are available. The experimental necking curve presented in Figure 6.4 is created from the strain pairs with the lowest major strain from each blank width.

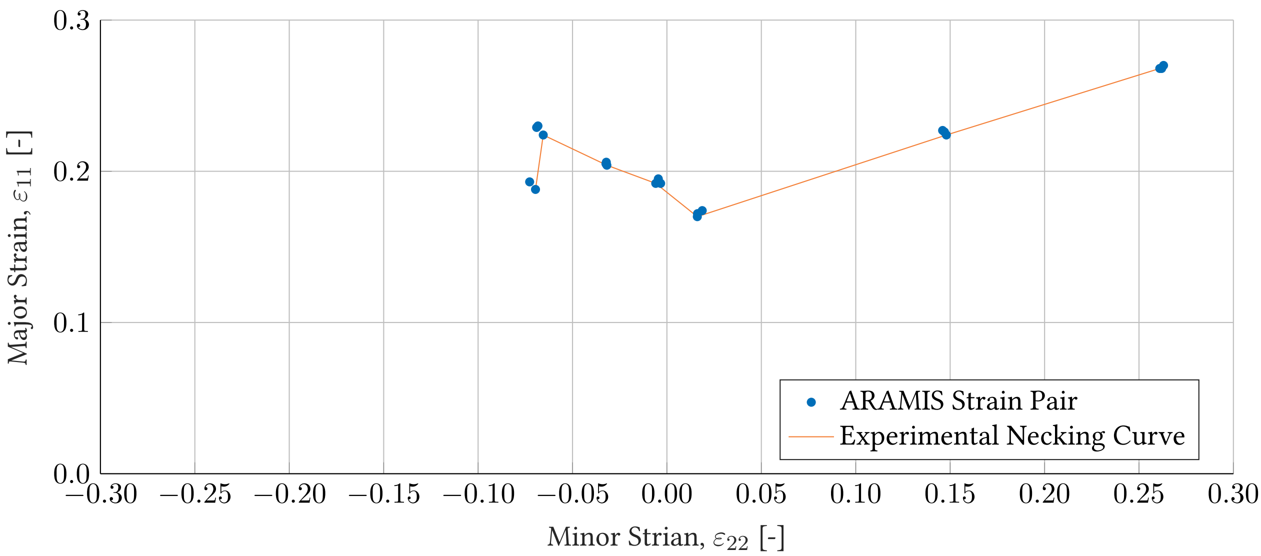

Figure 6.4. Strain pairs and initial necking curve for the AA6016 aluminium alloy. The strain pairs have been obtained from the 'FLC mode' in the DIC software ARAMIS™.

The necking curve presented in Figure 6.4 does however not cover the full range of the FLD, why additional data processing is needed.

6.2 Data Processing

As stated, the experimental necking curve needs to be modified to cover the full range from biaxial to uniaxial strain path conditions. In some cases, the FLD also contains limits for the shear and compressive strain path conditions however, this is out of scope for this limit curve determination.

Since the Nakajima blank with a width of 200 mm defines the biaxial strain path condition, the right-hand side of the necking curve is fully defined from the experiments. The left-hand side of the curve does however need to be theoretically defined. To determine the limit curve in the left-hand side of the FLD, a linear extrapolation based on the plane strain condition blank (125 mm) and the 100 mm blank width specimen is performed. This uniaxial extension of the necking curve can be seen in Figure 6.5. To determine when the uniaxial strain path condition is obtained Equation 6.1 is used

$$\varepsilon_{11} = \frac{(1 + r_\theta) \cdot \varepsilon_{22}}{r_\theta} \tag{6.1}$$

where r_θ is the Lankford coefficient in the tested direction. For a tensile test at Volvo Cars, the specimens are tested in the rolling direction, why r_0 listed in Table 6.2 is used. The uniaxial limit is found at the intersection between the uniaxial extension and the uniaxial limit presented in Figure 6.5.

Lankford Coefficients		
r_0	r_{45}	r_{90}
0.732	0.535	0.677

Table 6.2. Lankford coefficients of the AA6016 aluminium alloy.

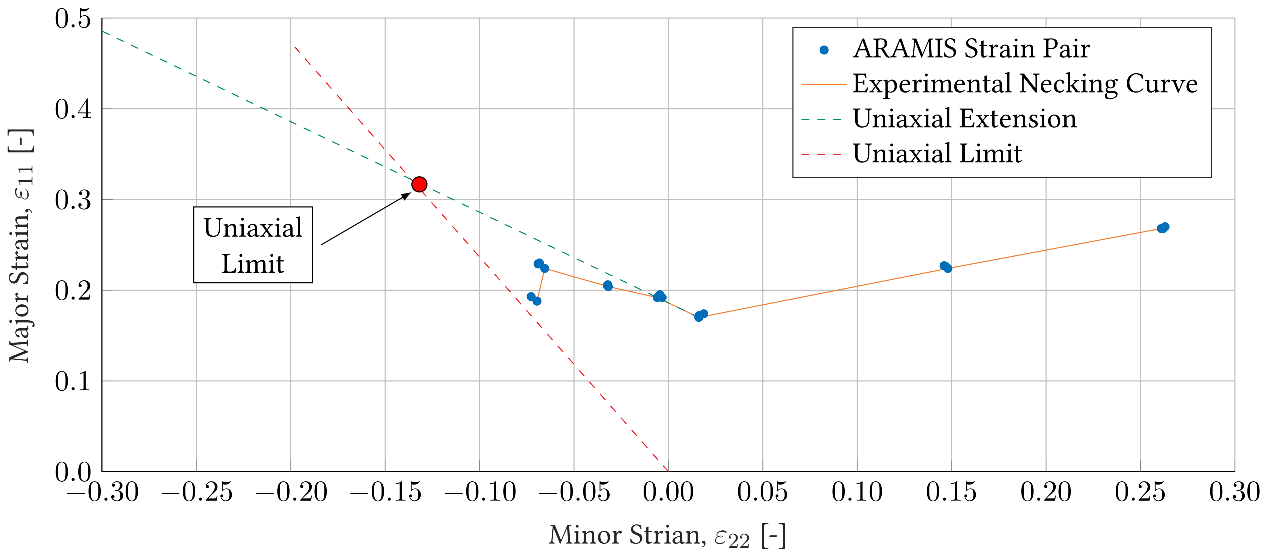

Figure 6.5. Uniaxial extension and uniaxial limit of the AA6016 aluminium alloy.

Having determined the uniaxial extension and limit, two trend lines are fitted to the right- and left-hand side respectively. For these trend lines, 34 points are evaluated, and the final necking curve of the AA6016 aluminium alloy can be created. This final curve is presented in Figure 6.6

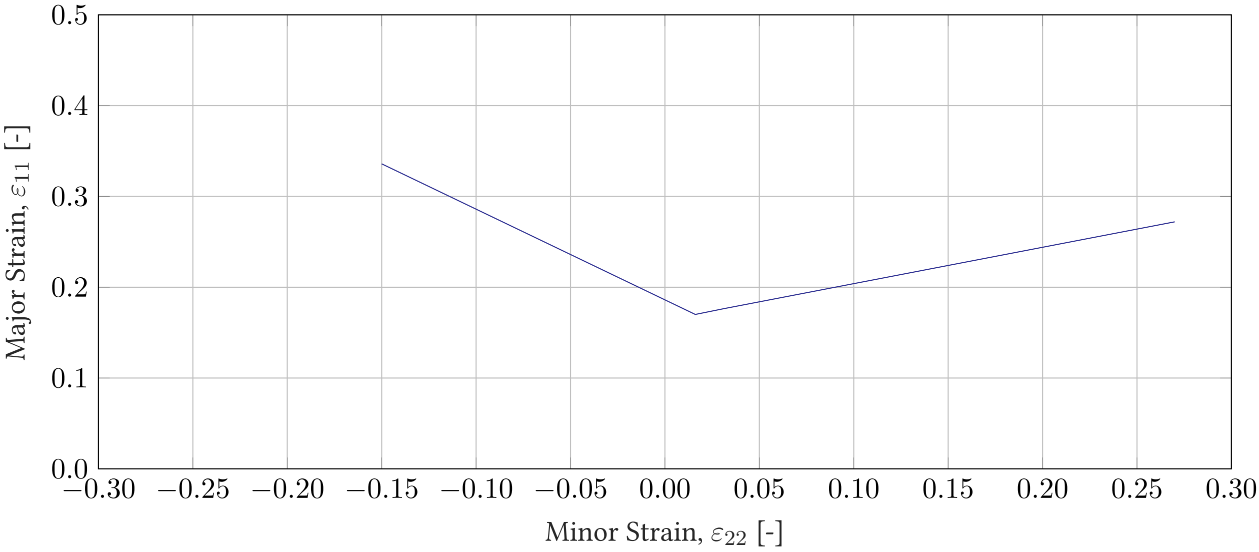

Figure 6.6. Final necking curve of the AA6016 aluminium alloy.

The presented methodology is repeated for the CR440Y780T-DP dual-phase steel alloy. When in possession of necking curves for both alloys, the validation of the GISSMO approach can be performed, using the bending-under-tension specimens of both alloys.

GISSMO Evaluation 7

Having determined the necking curves for both the AA6016 aluminium and CR440Y780T-DP dual-phase steel alloys, the GISSMO model is ready to be applied to the bending-under-tension specimens. Initially, the intermediate experimental setup with a punch nose radius of 6 mm will be evaluated. Before an actual evaluation of the damage in the specimens is determined, the transformation from the principal strain space to the stress triaxiality space must be performed.

7.1 Limit Curve Transformations

In Chapter 6 forming limit curves (FLC) describing the failure strain for both the AA6016 aluminium alloy and the CR440Y780T-DP dual-phase steel alloy (for convenience presented again in this chapter in Figures 7.1 and 7.3) were determined. By applying the transformation equations presented in Equation 5.22 the transformation of the determined FLCs can be performed mapping these from the principal strain space to the stress triaxiality space. Transforming the FLC for the AA6016 aluminium alloy (presented in Figure 7.1) the limit curve in the stress triaxiality space presented in Figure 7.2 is obtained.

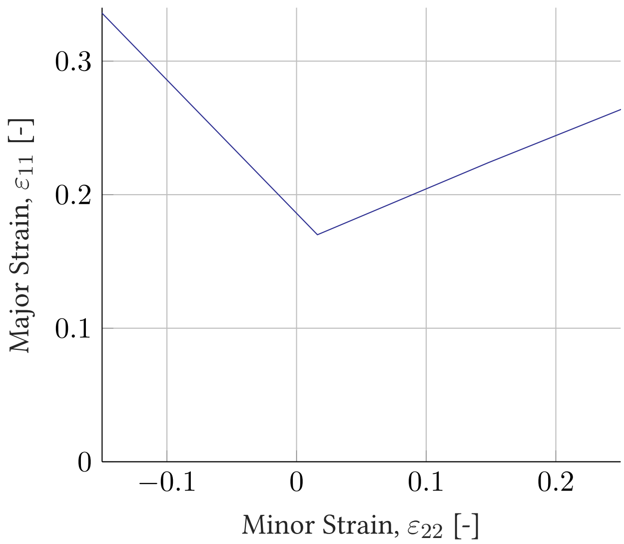

Figure 7.1. Forming Limit Curve in the principal strain space determining the failure strain for the AA6016 aluminium alloy.

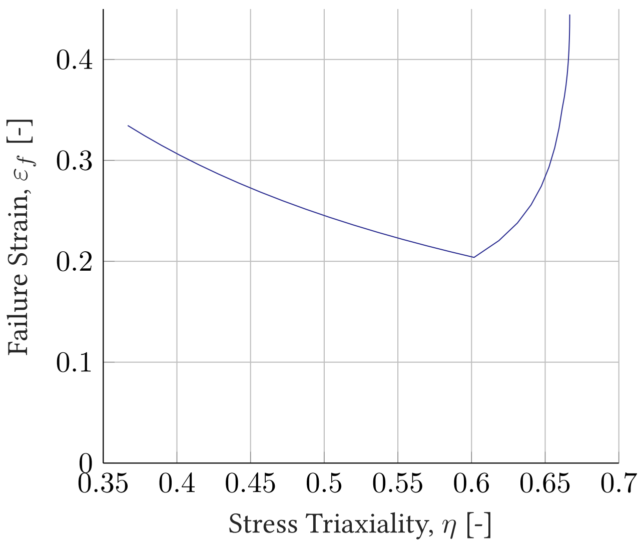

Figure 7.2. Forming Limit Curve from Figure 7.1 transformed into the stress triaxiality space.

The same transformation is performed for the FLC determined for the CR440Y780T-DP dual-phase steel alloy (presented in Figure 7.3). The transformation for the dual-phase steel alloy yields the limit curve presented in Figure 7.4.

Having determined the limit curves in the stress triaxiality space for both alloys, the evaluation of bending-under-tension R6 specimens can now be performed.

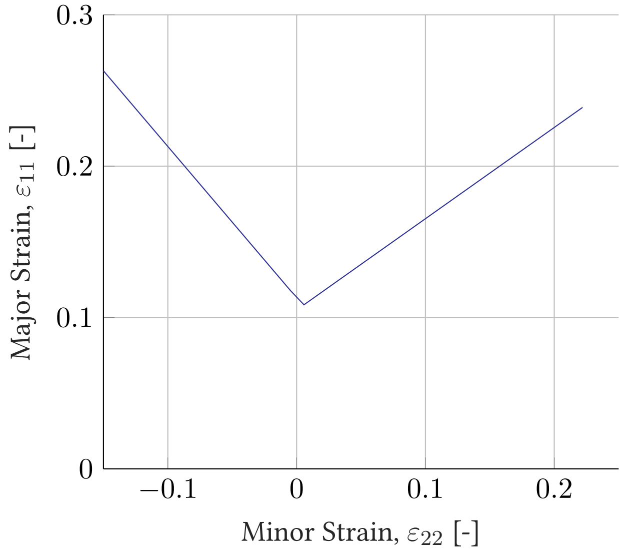

Figure 7.3. Forming Limit Curve in the principal strain space determining the failure strain for the CR440Y780T-DP dual-phase steel alloy.

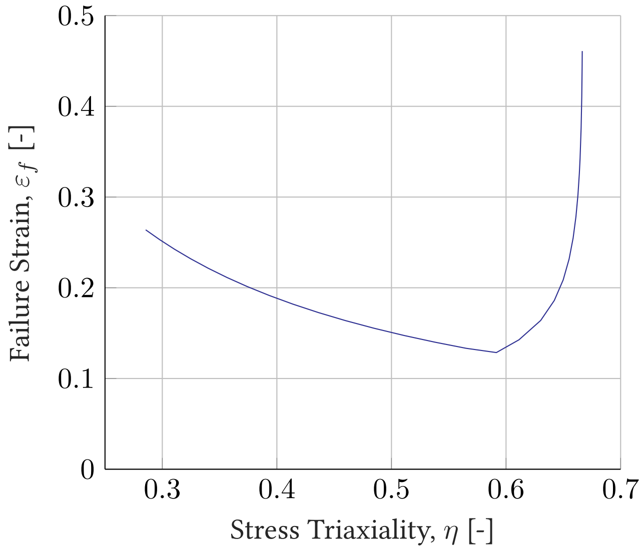

Figure 7.4. Forming Limit Curve from Figure 7.3 transformed into the stress triaxiality space.

7.2 Strain Gradient Assessment

For the evaluation of the bending-under-tension R6 specimens, a valid question to ask, is where to evaluate these. To clarify this, a strain gradient assessment must be performed for both materials. Introducing the idea of considering the sheet material as a superposition of layers through the thickness (see Figure 7.5), all with same mechanical properties as the base material, an evaluation of the strain gradient influence can be performed.

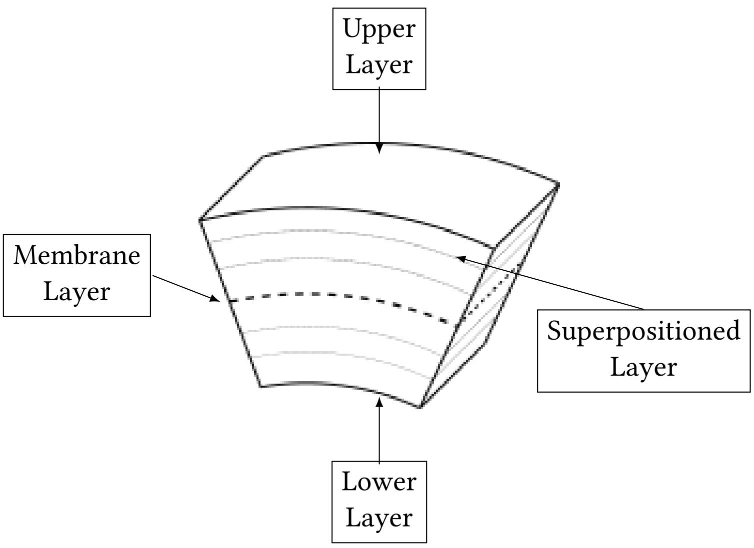

Figure 7.5. Terminology used for a sheet metal considered as a superposition of layers.

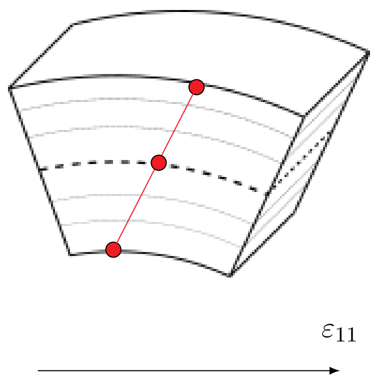

Figure 7.6. Illustration of the theoretical influence of a local bend on the strain gradient.

In theory, when exposing a sheet metal to a local bending, the strain gradient across the thickness of the sheet should behave as presented in Figure 7.6. This is checked in the numerical models for the two materials. To align the investigation of both materials, the element having the highest major strain value in the membrane layer is chosen.

Figure 7.7 presents the strain gradients of the dual-phase steel and aluminium alloy specimens. As

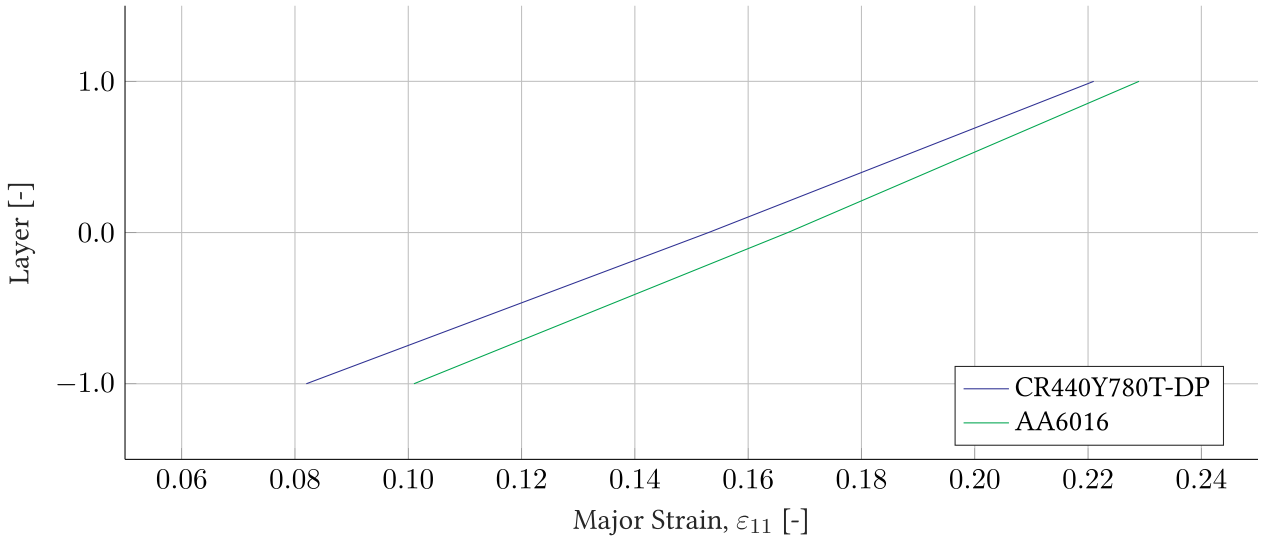

Figure 7.7. Strain gradient of the CR440Y780T-DP dual-phase steel and AA6016 aluminium alloys R6 bending-under-tension specimens. The y-axis represents the superpositioned layer in the numerical model where -1 is the lower layer, 0 is the membrane layer, and 1 is the upper layer. The values are based on the element with the highest major strain value in the membrane layer.

presented, the strain gradient follows the theory, and higher levels of straining is present in the upper layer than in e.g. the membrane and lower layers. Based on this, the final damage evaluation of the two bending-under-tension R6 specimens will be performed at the upper surface.

7.3 Damage Evaluation

Having determined the limit strain in the stress triaxiality space, and specified where on the sheet to evaluate, only a calibration of the numerical models is needed. This calibration ensures that the numerical models should resemble the strain state at the onset of localized necking as accurately as possible. The DIC measurements of the bending tests are yet again used, and the onset of localized necking is estimated applying the approach presented in Chapter 4. This yields the punch displacements presented in Table 7.1. Other than the calibration of the punch displacement, the numerical settings of both models are identical to the ones presented in Barlo (2019).

Material	Punch Displacement [mm]
CR440Y780T-DP	13.02
AA6016	15.02

Table 7.1. Punch displacements at the onset of necking for the two bending-under-tension specimens with a punch radius of 6 mm.

With the calibrated punch displacements, the evaluation can now be performed. The strain fields of the two models are transformed using the same transformation equations as for the limit curves (presented in Equation 5.22), and the damage can be calculated by applying Equation 5.21.

This yields the results presented in Figure 7.8. The figure presents the maximum damage i.e. the element having the highest damage in the numerical model. Consulting Figure 7.8 the results present a performance that resembles that of the Non-linear Forming Limit Diagram presented in Barlo et al. (2019).

The GISSMO approach is seen to perform well for the AA6016 aluminium alloy, where a maximum damage value of 0.9446 is predicted. This puts the specimen close to the onset of necking, and taking all of the uncertainties tied to the application of Finite Element simulations, von Mises based transformation and

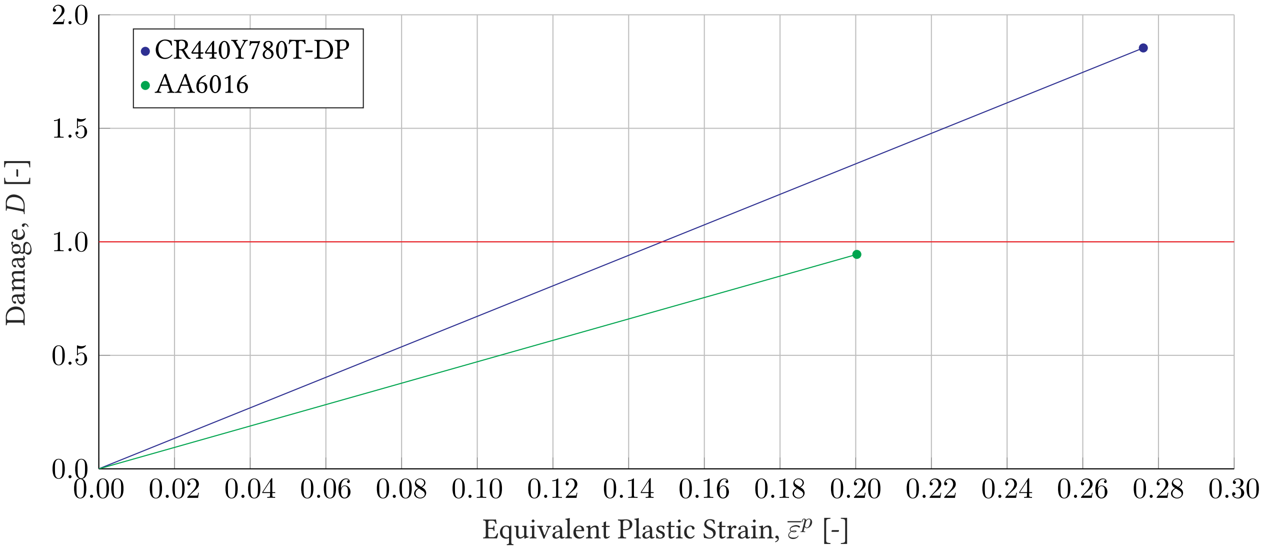

Figure 7.8. Maximum damage of the AA6016 aluminium and CR440Y780T-DP dual-phase steel alloys R6 bending-under-tension specimens.

potential experimental measuring errors into account, this is deemed as a good prediction. However, for the CR440Y780T-DP dual-phase steel alloy, the maximum damage value is 1.854 placing it well above the necking limit. Several potential reasons for this overestimation of the maximum damage value can be pointed out:

1. The Finite Element model of the bending-under-tension CR440Y780T-DP dual-phase steel alloy R6 test is not accurate.
2. The material model used for the numerical model does not reflect reality.
3. The bending effect on the CR440Y780T-DP dual-phase steel alloy is much greater than for the AA6016 aluminium alloy.

To address two of the three potential reasons, the major strain predictions of the CR440Y780T-DP dual-phase steel alloy bending-under-tension R6 specimen, found in the previous work by Barlo (2019), is presented in Figure 7.9.

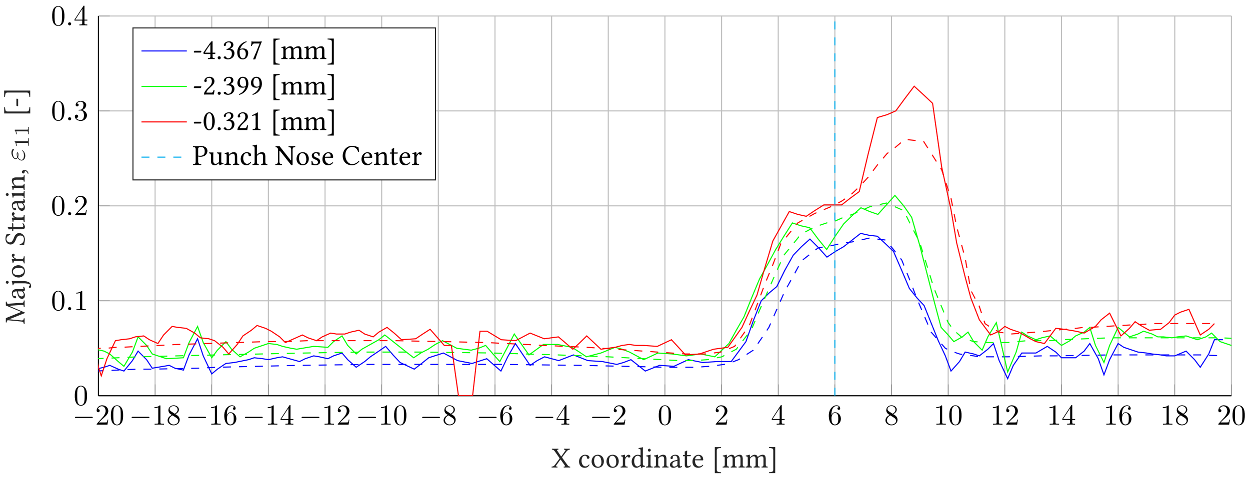

Figure 7.9. Major strain predictions of the CR440Y780T-DP dual-phase steel alloy bending-under-tension R6 specimen. The x-coordinates defines a section in the ARAMIS$^{\text{TM}}$ software, where the measurements are taken passing through the global maximum major strain. The dashed lines represent the numerical results, and the full lines represent the experimental measurements. The strain predictions is taken from Barlo (2019).

A good prediction compared to the experimental measurements of the major strain is obtained with the numerical settings of the Finite Element model up until 2.339 mm before fracture. This distance corresponds well to the onset of the localized necking. This prediction causes the first two reasons listed to initially be dismissed, and the bending effect of the CR440Y780T-DP dual-phase steel alloy is deemed the reason for the poor performance.

Based on the findings presented in this chapter, the GISSMO failure prediction approach is deemed not usable for the loading case of bending-under-tension. As the bending effect is believed to be the reason, an attempt to account for this will be presented in the following chapter.

Bending Corrected Forming Limit Surface 8

As presented in the previous chapter, the bending effect was deemed the reason for the poor performance of the GISSMO failure prediction approach for the CR440Y780T-DP dual-phase steel alloy. In the following chapter, an investigation of how to include this bending effect in a failure prediction approach will be presented.

In the work presented by Atzema et al. (2010) the authors presented the statement, that the Forming Limit Curve (FLC) is to some degree influenced by the stretch-bending loading situation. This influence has been reported to cause the failure strain to increase when the tool radius of which the specimen or component is bend over decreases. The following section will present the bending effect on both the AA6016 aluminium alloy and the CR440Y780T-DP dual-phase steel alloy.

8.1 Impact of Stretch Bending on Material Formability

The influence of the stretch bending on the formability of different alloys is something that have been discussed for a while. Already a decade and a half ago Sriram et al. (2003) presented a study on said influence on different high strength steels showing that the influence on dual-phase (DP) steel alloys is high compared to other steel types e.g. Transformation Induced Plasticity (TRIP) and High Strength Low Alloy (HSLA) steels when expressed as a relationship between the failure strain ε_f and the sheet thickness / tool nose radius ratio α. As presented in Chapter 7 the bending effect was suspected to influence the performance of the GISSMO failure prediction approach. In order to validate this previous statement, the two alloys used in this thesis are investigated. The investigation will be of the failure strain of the three available bending-under-tension experiments, and will be presented as in Sriram et al. (2003). The outcome of the investigation is presented in Figure 8.1.

From the investigation, it can be concluded that a bending effect is present in both alloys. Furthermore it can be concluded that the bending effect has a higher influence on the CR440Y780T-DP dual-phase steel alloy than on the AA6016 aluminium alloy. With these findings the idea of including the bending effect in the failure prediction approach seems even more relevant.

8.2 Bending Correction of the Forming Limit Curve

Having proved that the bending effect has a direct influence on the formability of the material a strain based bending correction of the Forming Limit Curve (FLC) is attempted using the three different bending-under-tension tests. An attempt of a bending corrected FLC has previously been presented by Ertürk et al. (2018) where a stress based in-plane correction was proposed. The approach presented in this report will focus on the top layer of the sheet due to the findings of the strain gradient assessment presented in Section 7.2.

The correction is performed by identifying the global maximum major strain in the failure mode wanted expressed (necking or fracture). Once again, the AA6016 aluminium alloy necking limit is used as an

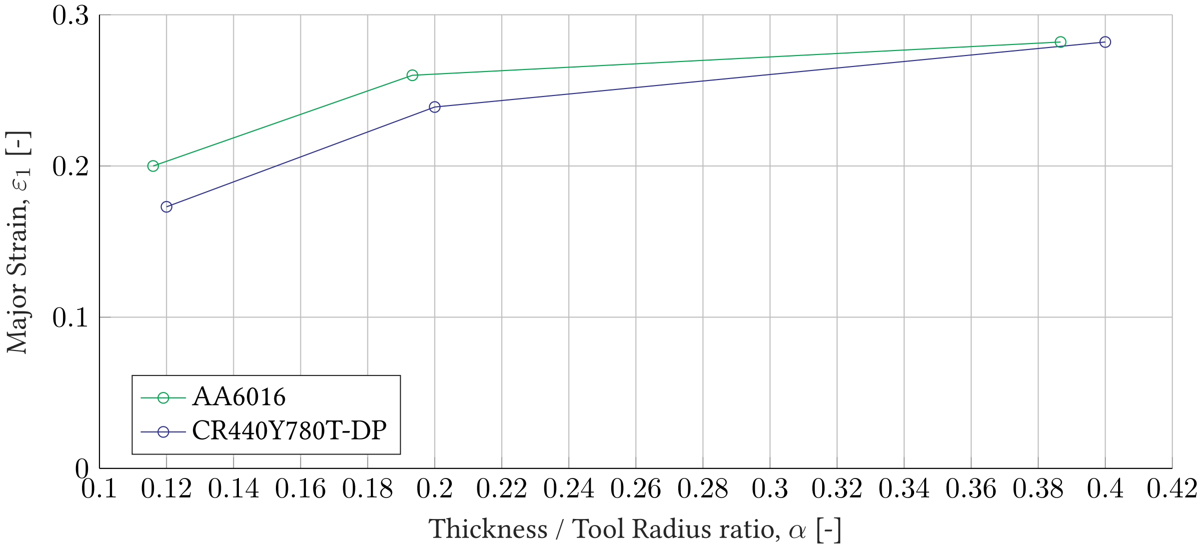

Figure 8.1. Relationship between the punch displacement at maximum force s and the ration between punch radius and sheet thickness α.

example. The procedure for determining the global maximum major strain in the bending specimens is explained in Section 4.1.1 and illustrated in Figures 4.5 and 4.6. Having identified the maximum major strain, and the corresponding minor strain, the correction of the FLC can be expressed as a difference in major strain $\Delta\varepsilon_{11}$. The delta value is calculated as presented in Equation 8.1, and illustrated in Figure 8.2.

$$\Delta\varepsilon_{11} = \varepsilon_{11,bending,max} - \varepsilon_{11,flc}(\varepsilon_{22,bending}) \tag{8.1}$$

Radius R	$\varepsilon_{11,bending,max}$	$\varepsilon_{22,bending}$	$\varepsilon_{11,flc}(\varepsilon_{22,bending})$
3	0.282	0.022	0.173
6	0.260	0.011	0.175
10	0.200	0.001	0.185

Table 8.1. Values used for the bending correction of the standard Forming Limit Curve.

Performing this correction for all three radii available on the necking curve for the AA6016 aluminium alloy, using the values presented in Table 8.1, the limits presented in Figure 8.3 are obtained.

In order to distinguish between when to use which curve the idea of using the tool nose curvature κ presented in Atzema et al. (2010) is adopted. By introducing the tool nose curvature, the FLD can be transformed from the 2D strain space into a 3D space defined as (ε_{22}, κ, ε_f). The tool nose curvature is defined as in Equation 8.2

$$\kappa = \frac{1}{R} \tag{8.2}$$

where R is the punch nose radius. This definition provides the curvature in the concave side of the bend (bottom side of the blank). This could cause small deviations from the experiments, as the measurement is performed at the convex side (top layer of the blank). However, this definition is used as a starting point, and can be adjust if the approach turns out to perform well. The used tool nose curvatures can be found in Table 8.2.

One thing that must be pointed out at this point is, that the model can not handle bending in two directions at this point. The data defining the curves are obtained from specimens all having only one bend and all of them in the same out of plane direction. With this clarified, the curvatures from Table 8.2 are linked

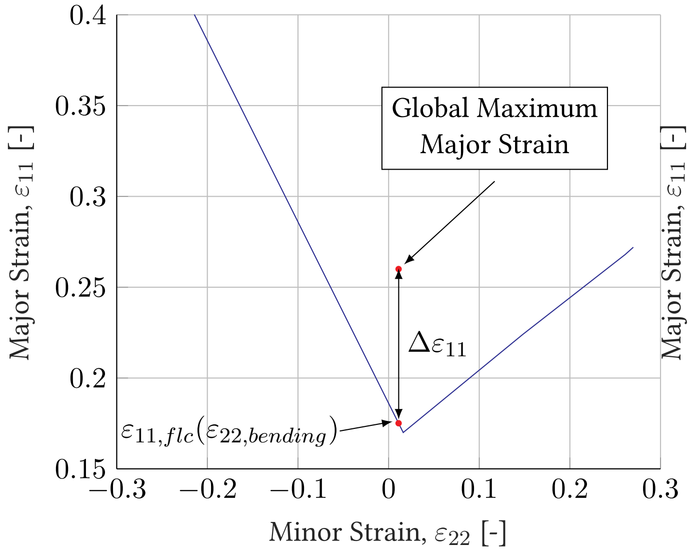

Figure 8.2. Illustration of the $\Delta\varepsilon_{11}$ correction of the necking limit curve for the AA6016 R6 specimen.

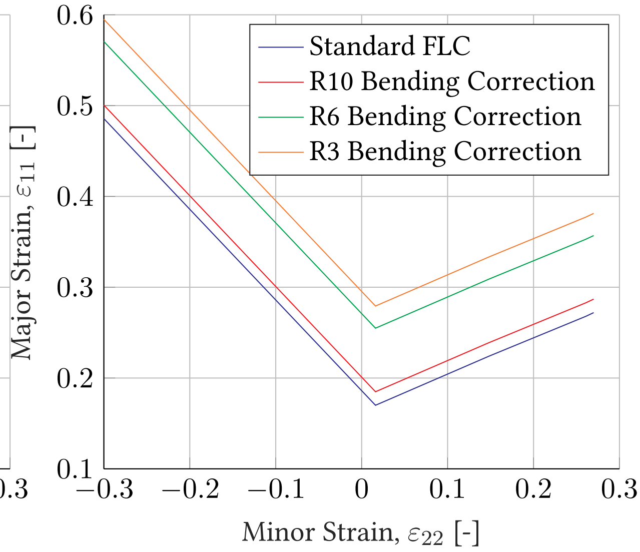

Figure 8.3. Bending corrected necking limit curves for the AA6016 aluminium alloy.

Punch Radius [mm]	3	6	10	50
Curvature [mm^{-1}]	0.3333	0.1667	0.1	0.02

Table 8.2. Curvatures calculated from the different punch nose radii.

with the bending corrected curves from Figure 8.3, and a surface is fitted to the data points. This surface will be called the Bending Corrected Forming Limit Surface (BC-FLS), and is illustrated in Figure 8.4. The equation defining the BC-FLS for the necking of the AA6016 aluminium alloy is presented in Equation 8.3, and is valid when $-0.3 \leq \varepsilon_{22} \leq 0.3$ and $0 \leq \kappa \leq 0.35$.

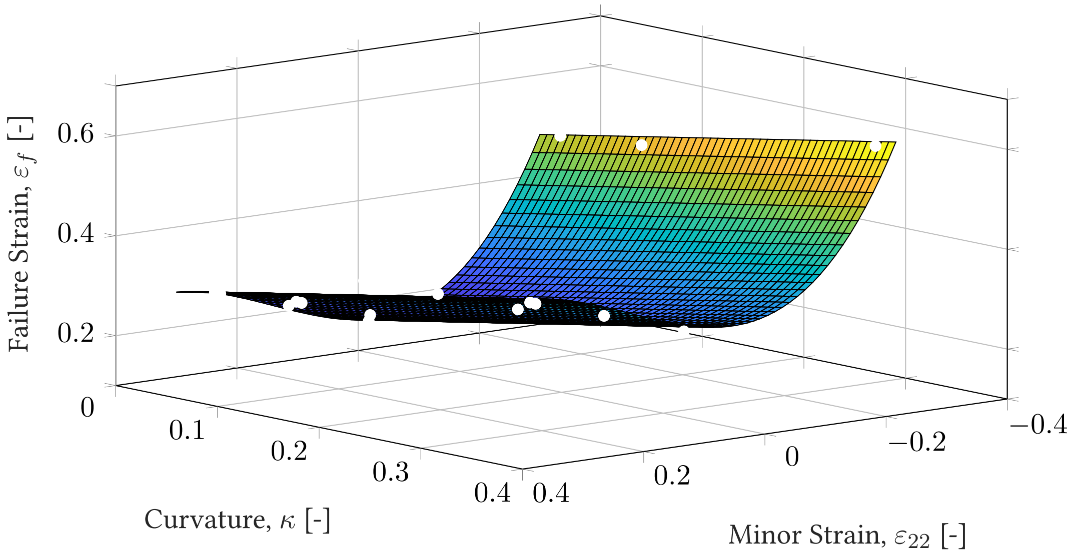

Figure 8.4. Bending Corrected Necking Limit Surface for the AA6016 aluminium alloy. The white data points represent the data points from the corrected FLCs presented in Figure 8.3.

$$\varepsilon_f = 0.1615 + 0.1571 \cdot \varepsilon_{22} + 0.3744 \cdot \kappa + 2.371 \cdot \varepsilon_{22}^2 - 5.632 \cdot 10^{-16} \cdot \varepsilon_{22} \cdot \kappa - 5.646 \cdot \varepsilon_{22}^3 + 1.309 \cdot 10^{-14} \cdot \varepsilon_{22}^2 \cdot \kappa \tag{8.3}$$

8.3 Volvo Cars Test Die

As the bending-under-tension experiments have been used for the creation of the Bending Corrected Forming Limit Surface (BC-FLS), an alternative component must be considered for the validation of the approach to avoid a false positive performance.

The alternative component chosen for the later validation of the BC-FLS approach, is a test die developed at Volvo Cars and depicts a more production like setup than the lab scale bending-under-tension experiments. The test die will in this example use a blank of the AA6016 aluminium alloy, and expose it to a stretch-bending condition with biaxial pre-stretching as encountered in critical automotive body component features such as fenders and door handles. An illustration of the stamped test die panel can be seen in Figure 8.5.

Figure 8.5. Volvo Cars test die AA6016 aluminium alloy stamped panel. The panel will be used for the validation of the BC-FLS failure prediction approach.

The following subsections will present the panel geometry, experimental results, and the applied Finite Element model.

8.3.1 Panel Geometry and Experimental Results

The test die developed at Volvo Cars operates with two different stamped geometries, and each geometry is stamped with a punch nose radius of 4 and 8 mm. The two geometries can be seen in Figures 8.6 and 8.7 respectively.

The geometry presented in Figure 8.6 is, according to Volvo Cars Stamping Engineering, the most important of the two to accurately predict, since this is a feature often present in body components e.g. fenders, bonnets, and side members, why exactly this geometry, highlighted in Figure 8.8, will be used for the validation of the BC-FLS approach.

As presented in Figure 8.8 the dimensions of the panel is quite large, why a DIC measurement during stamping was not possible. Instead, a manual inspect of the panel was performed post stamping, and yielded the results presented in Figure 8.9.

Figure 8.6. Geometry 1 of the Volvo Cars test die. This geometry will be used for the validation of the BC-FLS approach.

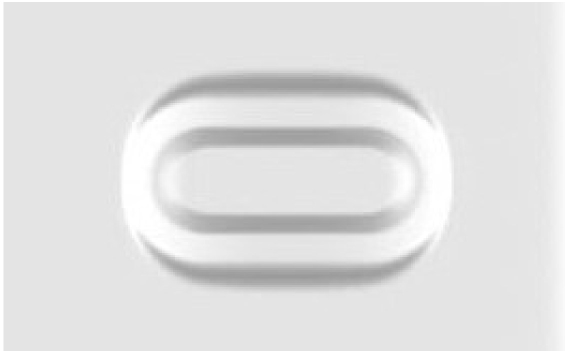

Figure 8.7. Geometry 2 of the Volvo Cars test die.

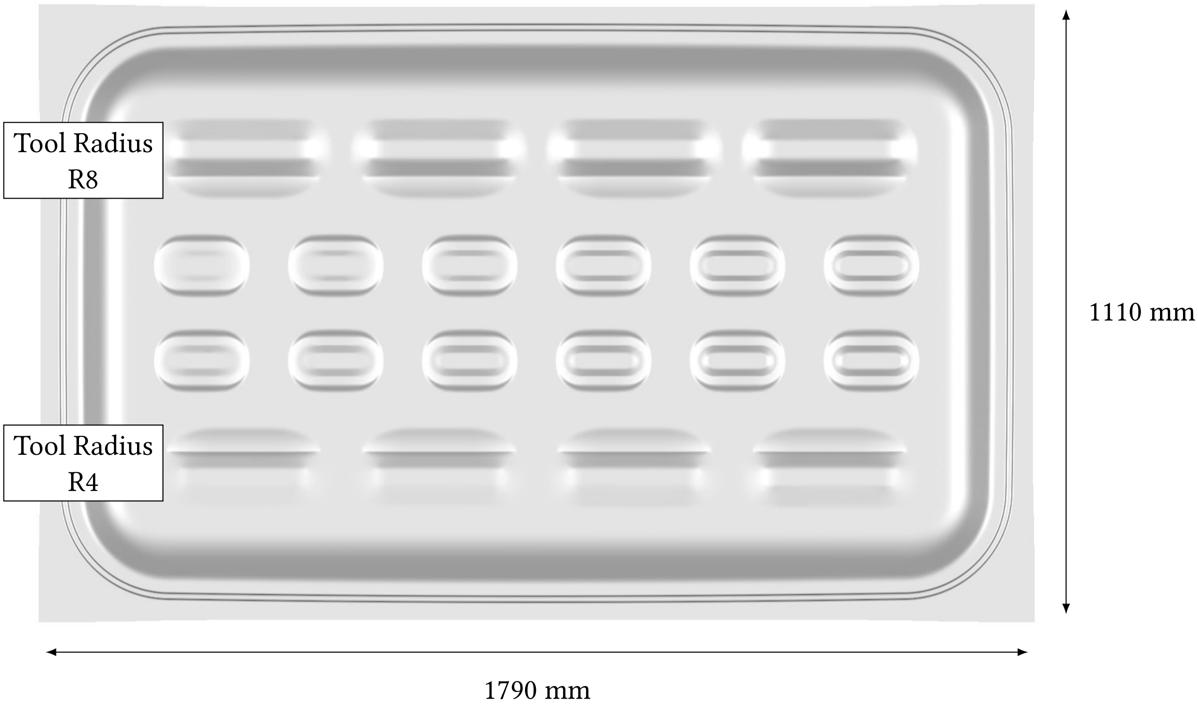

Figure 8.8. Volvo Cars test die AA6016 aluminium alloy stamped panel. The panel will be used for the validation of the BC-FLS failure prediction approach.

8.3.2 Finite Element Model

For the validation of the BC-FLS failure prediction approach a FE model of the Volvo Cars test die will be used in the commercial Finite Element code AutoForm$^{\text{plus}}$ R8. The original FE model has been created by Mr. Kristoffer Trana from Volvo Cars applying the Volvo Cars standard numerical settings. This model will for the purpose of the validation be modified. The modifications made to the FE model are highlighted in Table 8.3.

To minimize the material flow in the FE model, geometrical draw beads are used instead of increasing the blank holder force. With the application of the geometrical draw beads, the FE model resembles reality more since the actual blank holder force observed in the press can be used. An illustration of the geometrical draw beads in the FE model can be found in Figure 8.10.

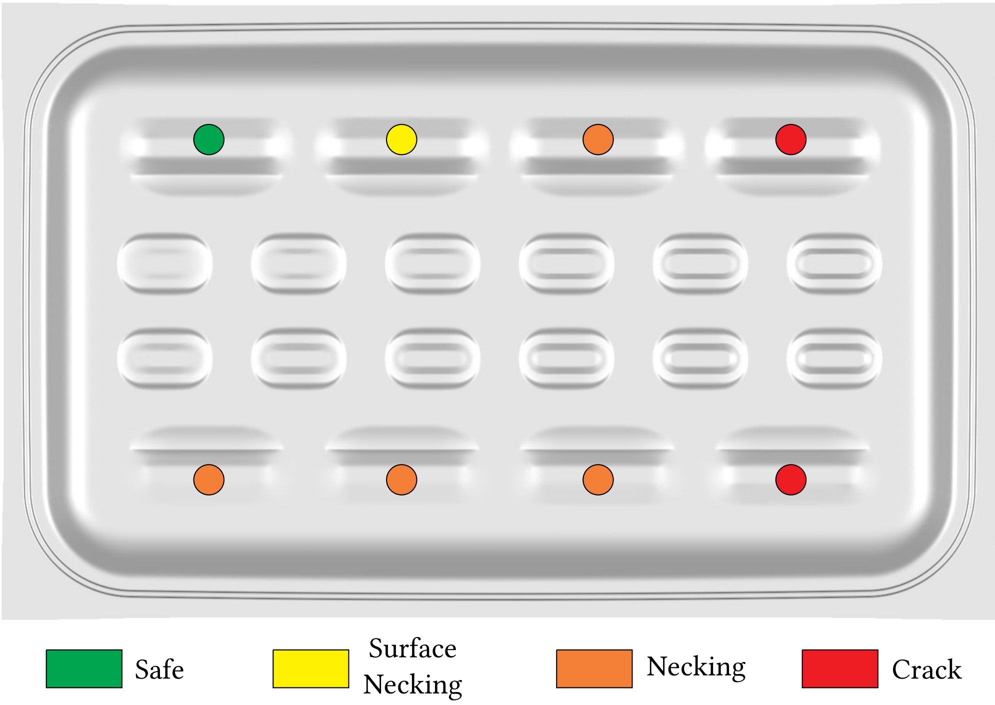

Figure 8.9. Different failure modes present in the stamped panel. These modes are observed from an experimental test of the tool setup.

General	
Element Type	Elasto-Plastic Shell with 11 integration points through thickness
Yield criterion	BBC05
Friction model	Global Coulomb model with friction coefficient $\mu = 0.12$
Thickness stress	On
Accuracy	
Allowed radius penetration	0.1 mm
Max. element angle	10°
Max. refinement level	5
Master element Size	20 mm
Min. element size	0.62 mm
Time Step Control	
Convergence tolerance	0.5
Max. iterations	80
Allowed boundary penetration	0.08 mm

Table 8.3. Important numerical settings used for the Finite Element model of the Volvo Cars test die. The numerical settings highlighted in red are the ones modified by the author.

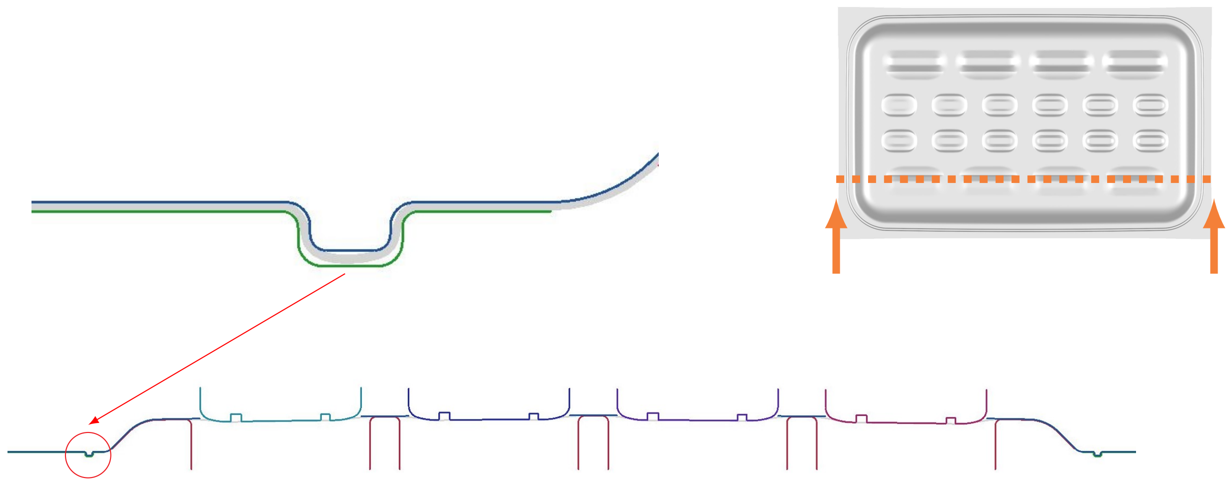

Figure 8.10. Geometrical draw beads used in the Finite Element model of the Volvo Cars test die. The geometrical draw beads are used to minimize material flow.

8.4 Validation of Proposed Failure Prediction Approach

Having created the BC-FLS and and being in possession of a FE model, a validation of the proposed failure prediction approach can now be attempted.

8.4.1 Implementation in AutoForm$^{\text{plus}}$ R8

For the validation of the proposed failure prediction approach, the idea of a failure measure is implemented in AutoForm$^{\text{plus}}$ R8 as a User Defined Variable (UDV). The failure measure is defined as in Equation 8.4, and an indication of onset of necking is given when F reaches unity.

$$F = \frac{\varepsilon_{11}}{\varepsilon_f(\varepsilon_{22}, \kappa)} \tag{8.4}$$

The failure measure is a relationship between the determined failure strain ($\varepsilon_f(\varepsilon_{22}, \kappa)$) and the major strain in the FE model (ε_{11}). In order to obtain the correct failure strain value, the minor strain (ε_{22}) and the curvature (κ) is taken from the FE model as well. Just as for the investigation of the impact of stretch bending on material formability (presented in Section 8.1) the evaluation of the FE model will be performed at the upper layer.

Obtaining the curvature from the FE model, additional options for the curvature definition have become available. Since the FE model will most likely not have a uniform curvature in each element (exemplified in Figure 8.11), a definition of how to define element curvature is needed.

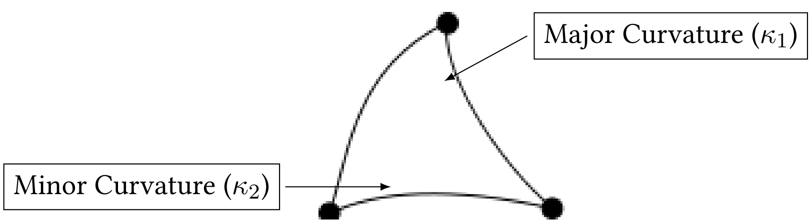

Figure 8.11. Example of curvature variation within an element.

The used Finite Element code AutoForm$^{\text{plus}}$ R8 offers four different curvature definitions pr. element:

1. Major curvature

2. Minor curvature
3. Mean curvature
4. Gaussian curvature.

To create the failure measure for the FE model in question, the mean curvature is used, and is defined as:

$$\text{Mean curvature} = \frac{\kappa_1 + \kappa_2}{2} \tag{8.5}$$

The mean curvature is chosen in an attempt to correct slightly for the curvature definition presented in Section 8.2 Equation 8.2. Having presented the failure measure, and defined the curvature in the FE model, the actual validation of the model can now be performed.

8.4.2 Performance Review

With both the failure strain determination and FE model presented, the validation of the proposed approach can now be performed. Equation 8.4 has been implemented in AutoForm$^{\text{plus}}$ R8 as an UDV, and the results of this implementation is presented in Figure 8.12.

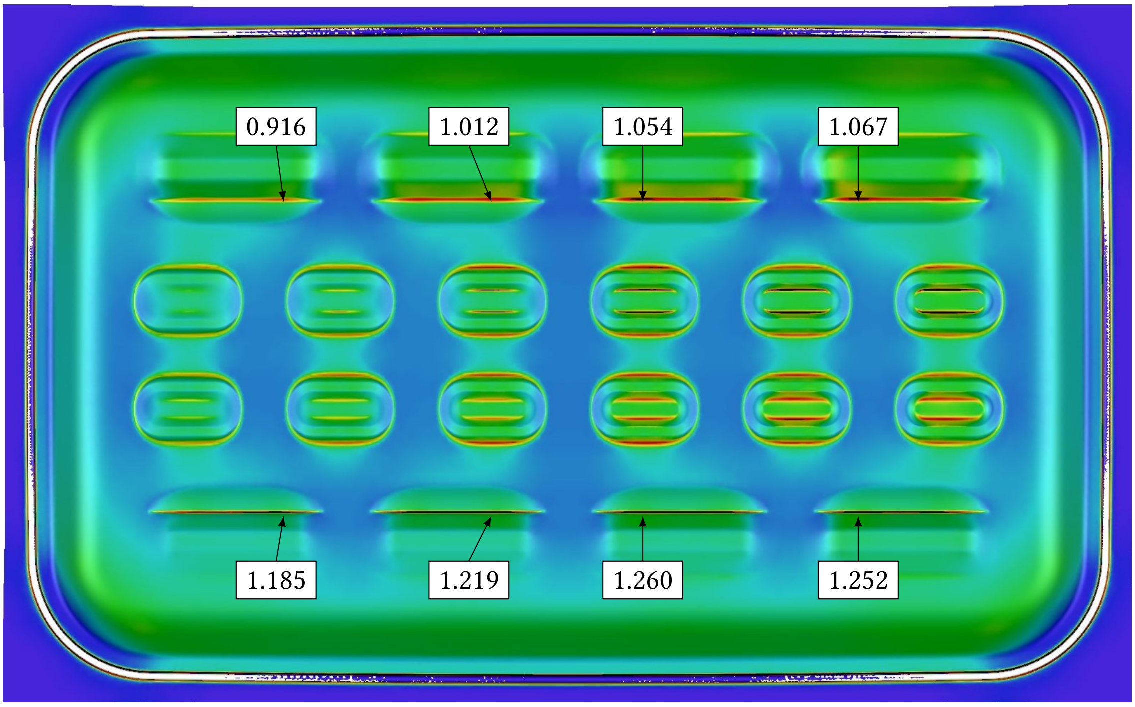

Figure 8.12. Local maximum failure values determined from Equation 8.4. The damage values have been implemented in AutoForm$^{\text{TM}}$ R8 as an User Defined Variable (UDV). The implementation is here plotted as an 'out of range' plot, meaning all black patches are areas that have passed the necking surface.

The presented results show a good prediction of the failure modes observed in the manual inspection of the panel (presented in Figure 8.9). All zones are predicted accurately, most noticeably the two upper left zones. The manual inspection yielded these as being safe and having a surface neck respectively. In the results presented in Figure 8.12, the failure value for the upper leftmost zone is 0.916 deeming that particular zone safe (necking is indicated then F reaches unity) and the zone to the right of this has a failure value of 1.012 indicating that the zones has just passed the point of localized necking corresponding well with the observation of a surface neck.

For the zones where a crack was observed in the panel, higher failure values than the ones presented in Figure 8.12 were suspected. These low values could be explained by the plane stress assumption that is general for sheet metal forming simulations applying shell elements. This plane stress assumption is only valid up to the onset of localized necking, why especially the accuracy of the major strain prediction in the FE model suffers once the onset of localized necking has been passed. An example of this is can be seen in Figure 7.9 comparing the experimentally and numerically obtained major strain in the CR440Y780T-DP dual-phase steel bending-under-tension R6 specimen. A similar behaviour is seen in the AA6016 aluminium alloy R6 bending-under-tension specimen presented in (Barlo 2019, Section 4.5.1).

For a reference of performance for the results presented in Figure 8.12, the FE model is also evaluated using the standard FLD. The way this is done in AutoForm^{plus} R8 is to look at the already implemented Max Failure option. The Max Failure option is defined as:

$$F_{max} = \frac{\varepsilon_{11}}{\varepsilon_{11,flc}(\varepsilon_{22})} \tag{8.6}$$

where ε_{11} is the major strain in the element, and $\varepsilon_{11,flc}(\varepsilon_{22})$ is the limit strain from the FLC at the element minor strain value ε_{22}. The results of this evaluation is presented in Figure 8.13. The outcome of the Max Failure evaluation clearly shows a superior performance of the proposed BC-FLS approach, since none of the zones are accurately predicted when applying the standard FLC.

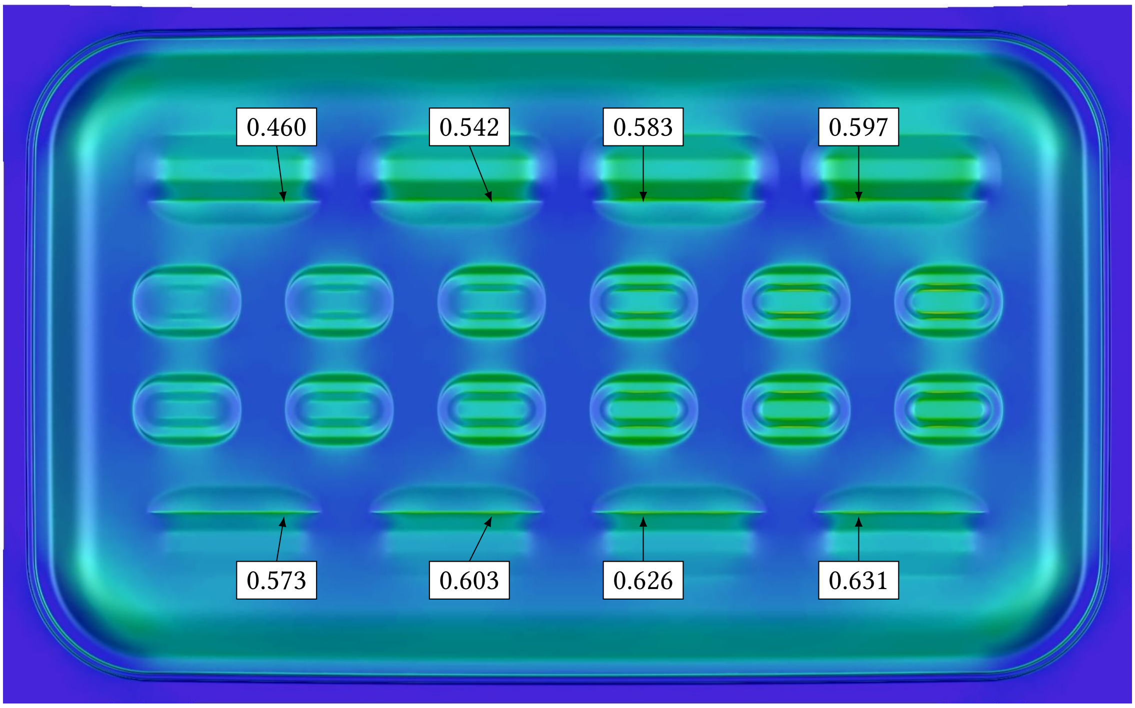

Figure 8.13. Local maximum failure values determined from Max Failure approach implemented in AutoForm AutoForm^{TM} R8. The implementation is here plotted as an 'out of range' plot, meaning all black patches are areas that have passed the necking surface.

From the results presented in this chapter, a conclusion on the BC-FLS approach can be drawn. The proposed approach is seen to accurately predict the failure modes in the different zones of the Volvo Cars Test Die well, and at the same time shows a superior performance compared to the standard FLD, in this chapter presented as the Max Failure criteria implemented in AutoForm^{plus} R8.

Discussion 9

Throughout the work presented in this report, two evaluations spaces for failure prediction in sheet metals have been tested as alternatives to the principal strain space in which the standard Forming Limit Diagram (FLD) operates in:

1. The GISSMO approach using a stress-strain based evaluation space defined by the stress triaxiality η and the equivalent plastic strain $\bar{\varepsilon}^p$.
2. The Bending Corrected Forming Limit Surface (BC-FLS) approach using a strain-geometry based evaluation space defined by the major strain ε_{11}, minor strain ε_{22}, and the component surface curvature κ.

The following chapter will discuss the the two evaluation spaces and attempt to uncover the potential shortcomings of these.

9.1 The GISSMO Approach

9.1.1 Strain vs. Stress Based Transformation

In the GISSMO approach presented in Chapter 5, an approach based on the transformation of the FLC in the principal strain space was presented. Consulting the original definition of the stress triaxiality η presented in e.g. Andrade et al. (2016), this is defined as:

$$\eta = \frac{\sigma_m}{\bar{\sigma}_{vm}} = -\frac{p}{\bar{\sigma}_{vm}} = \frac{\frac{\sigma_{11}+\sigma_{22}+\sigma_{33}}{3}}{\sqrt{\frac{1}{2}\cdot\left[(\sigma_{11}+\sigma_{22})^2+(\sigma_{11}-\sigma_{33})^2+(\sigma_{22}-\sigma_{33})^2\right]}} \tag{9.1}$$

Here, the definition uses the stress instead of the strains, why it can seem a bit odd to perform a strain based transformation. The reason for this is found in three areas

1. Data availability
2. Current measurement techniques
3. Industry standard

As the FLD has been the industry standard since introduced by Keeler & Backofen (1964) every material model for sheet metal forming simulation at Volvo Cars (and most likely also other automotive manufacturers) includes an FLC. Having all these data available, and a very well defined way of determining FLCs (ISO 12004 standard, Yoshida et al. (2008)) it was deemed beneficial to reuse these available data instead of having to define an all new way of determining stresses during experiments.

When determining the FLC, Digital Image Correlation (DIC) systems are most often used. In the case of the curves determined at Volvo Cars, the DIC system ARAMIS™ by German manufacturer GOM is used. This system allows for a strain history analysis necessary for the determination of the onset of localized necking. If the original stress based definition of the stress triaxiality should be used for the creation of limit curves, alternative options to the DIC systems must be found, where the stresses in e.g. the Nakajima tests are measured instead of the strains.

Lastly, as the strain based FLC has been the industry standard almost since its introduction in 1964, the concept of using strains for forming limits is something that is now deeply lodged into the minds of the stamping community. In order to ease a potential transition from the the FLC to an approach like the GISSMO approach, it is deemed beneficial that it is strain based.

So far, the strain based transformation approach has been accepted without being validated with the original formulation of the stress triaxiality. Figure 9.1 presents the same specimen where a strain based and stress based transformation approach has been used.

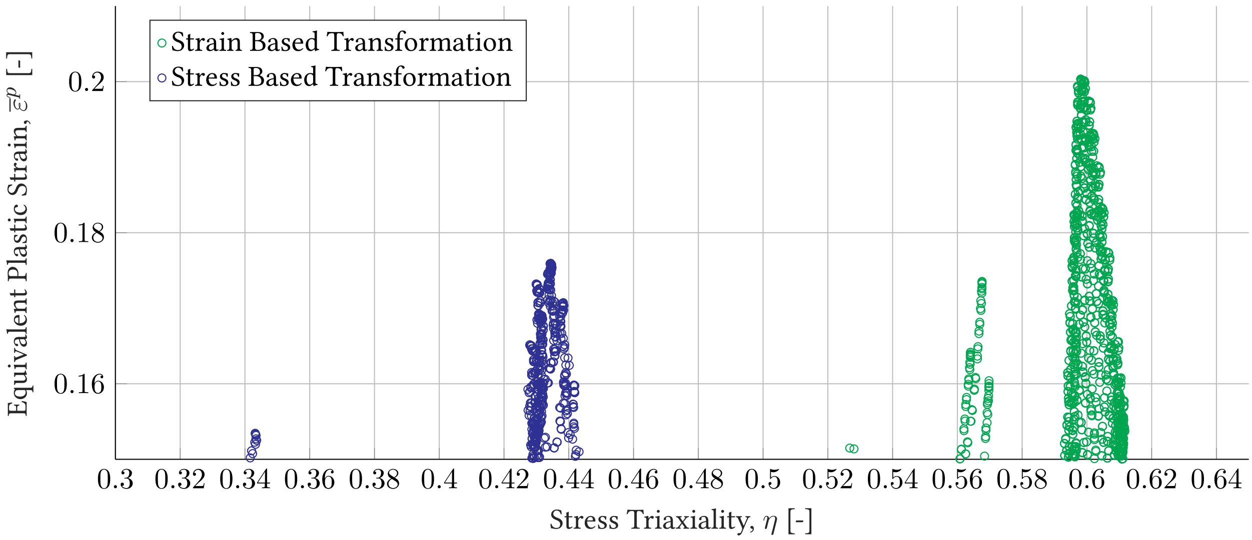

Figure 9.1. Difference between a strain and stress based strain field transformation.

The specimen tested has been simulated in AutoForm$^{\text{plus}}$ R8 with the BBC05 constitutive model. From this simulation, the major and minor stresses and strains have been exported along with the equivalent stress and equivalent plastic strain. Table 9.1 lists the different approaches to determine the equivalent plastic strain and the stress triaxiality for the two transformation approaches.

Parameter	Strain Based Approach	Stress Based Approach
Equivalent Plastic Strain	$\sqrt{\frac{4}{3} \cdot (\varepsilon_{11}^2 + \varepsilon_{22}^2 + \varepsilon_{11} \cdot \varepsilon_{22})}$	Calculated by AutoForm$^{\text{plus}}$ R8
Triaxiality	$\frac{2 \cdot (\varepsilon_{11} + \varepsilon_{22})}{3 \cdot \bar{\varepsilon}^p}$	$\frac{\frac{1}{3} \cdot (\sigma_{11} + \sigma_{22} + 0)}{\bar{\sigma}}$

Table 9.1. Equations and methods for determining the equivalent plastic strain and stress triaxiality when performing the strain and stress based transformations.

As seen in Figure 9.1 the two transformed strain fields does not coincide. This is due to the path independence of the stress based approach where the stresses are computed by considering the strain increment, thereby only depicting what has happened in the last increment. This way of including the path non-linearity is desired, but for a strain based approach, this is a difficult task not yet fully solved. This exact issue will be discussed later on.

There is no doubt that the stress based approach would create more accurate results when dealing with parts experiencing non-linear strain paths, but one big issue presents itself for the stress based approach. Currently, a method for determining a stress based forming limit from experimental data is extremely difficult if even possible. As presented throughout this report, the definition of the forming limit is extremely important in the prediction of failure in sheet metals. This leads to the conclusion that it would at this point be better to modify the current GISSMO to take non-linear strain paths into account, than to develop an entire new measuring technique for a stress based forming limit.

9.1.2 Path Dependency

Accepting the von Mises strain based transformation equations, another issue presents itself. During the derivation of said transformation equations an assumption of linear deformation ($d\varepsilon = \varepsilon$) was made. The discussion on path dependency in the stamping community has been around for several years, and a general and robust approach to account for this is yet to be found. Several attempts have however been made where the approach presented by Volk et al. (2012) and Volk et al. (2013) has been implemented in AutoForm$^{\text{plus}}$ R8. This approach relies on a discretization of the strain paths and a recalculation of the unique strain path lengths. A way to get around the path dependency problem of the GISSMO model could possibly be to adopt this approach and calculate the non-linear failure (F_{nl}) for each unique strain path. This way of thinking is illustrated in Figure 9.2.

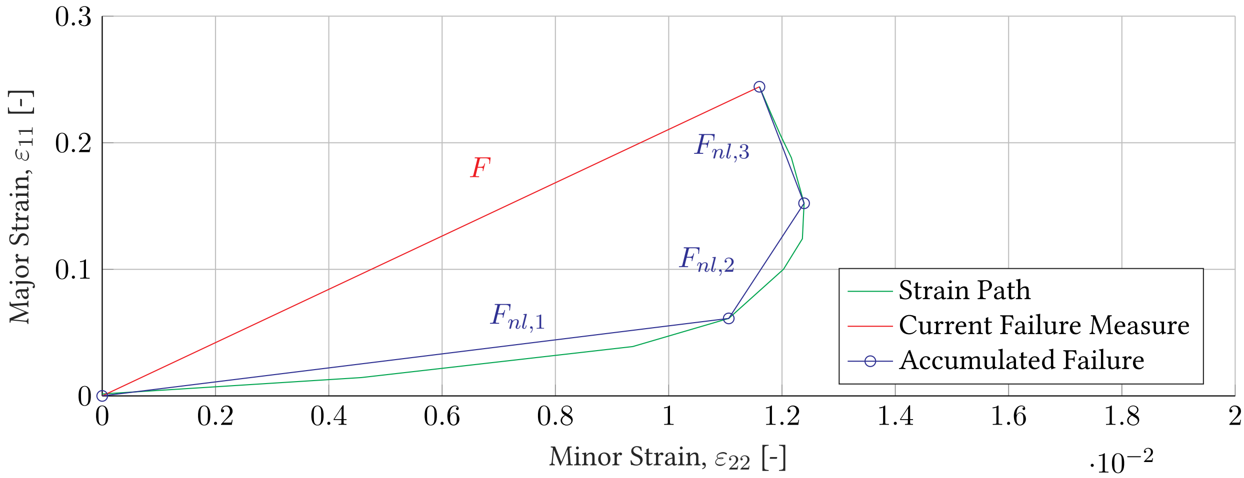

Figure 9.2. The concepts of linear and non-linear failure determination.

With this approach, it is possible a new way to calculate the non-linear failure or some type of correction is needed to calculate an accumulated failure in the different steps as defined in Equation 9.2.

$$F_{nl} = \sum_{i=1}^{n} F_{nl,i} = F_{nl,1} + F_{nl,2} + \ldots + F_{nl,n} \tag{9.2}$$

For the GISSMO model to bring any advances to the discussion on accurate failure prediction in sheet metals, this is a critical pitfall that needs to be addressed. If left with the current way of determining the failure, it is believed that the GISSMO model will perform almost identical to the standard FLD approach.

9.2 The Bending Corrected Forming Limit Surface Approach

9.2.1 Differentiated Bending Correction

One of the key elements in the proposed BC-FLS approach, is the $\Delta\varepsilon_{11}$ offset of the FLC. The current method presented in Chapter 8 offsets the entire FLC with the identified $\Delta\varepsilon_{11}$ value for different punch nose radii. This approach to a bending correction works well when the component evaluated is in the plane strain region. According to the findings of Atzema et al. (2010), the largest effect of the bending is seen in exactly the plane strain region, where the effect is moderate in the biaxial strain region, and and almost negligible in the uniaxial strain region. Therefore, a differentiated correction of the FLC would most likely depict material behaviour more accurately. An example of a differentiated correction is presented in Figure 9.3.

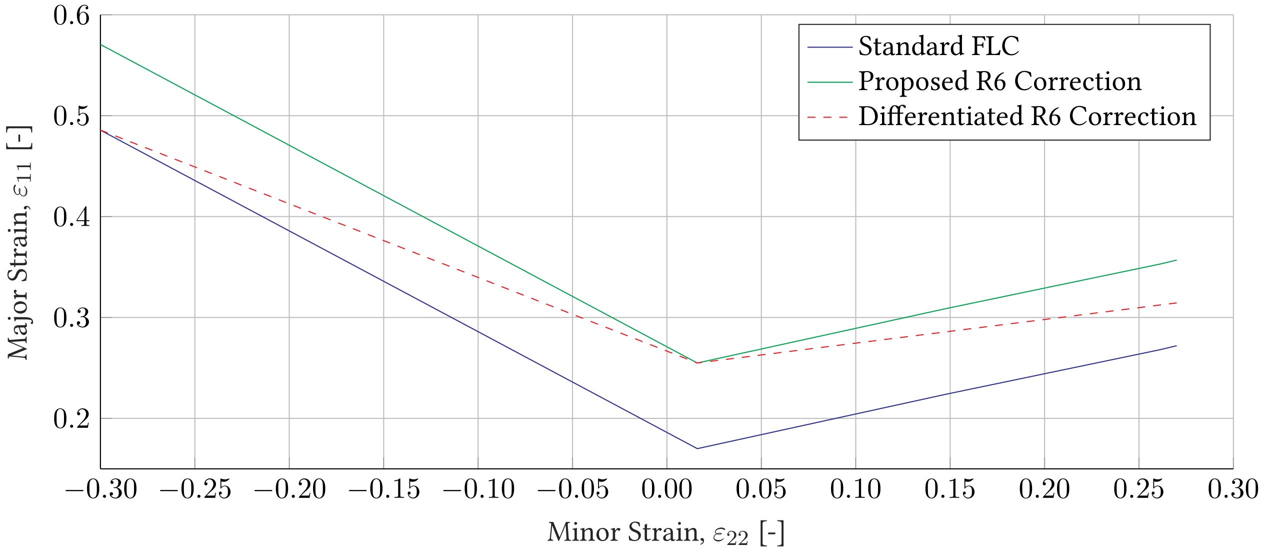

Figure 9.3. Example of a differentiated bending correction of the FLC as opposed to the current offset of the entire FLC.

Figure 9.4 presents the strain paths of the local maximum failure elements from the results presented in Figure 8.12. As presented, these are in the proximity of the plane strain region, why the constant $\Delta\varepsilon_{11}$ offset of the FLC is justified in the case of the Volvo Cars Test Die.

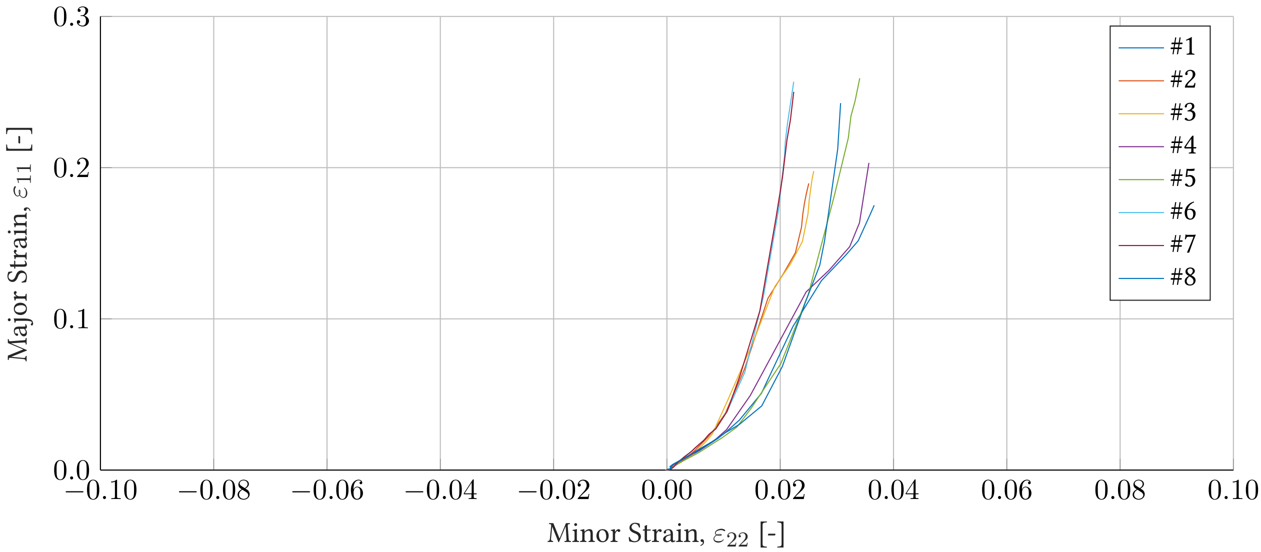

Figure 9.4. Strain paths of the local maximum failure elements of the Volvo Cars Test Die panel. Strain path #1 represents the upper left corner and a clockwise numeration is then performed of the results presented in Figure 8.12.

In order to perform a differentiated bending correction of the FLC, two approaches are found as possible candidates:

1. Bending-under-tension tests with blank geometries that represents the uniaxial and biaxial strain situations or,
2. A phenomenological approach.

Inarguably, the introduction of additional experimental tests for each punch nose radius would result in the most accurate forming limit surface. In the approach presented in Chapter 8, three bending corrections are performed of the FLC. Taking the experimental approach to the differentiated correction, this would result in an additional six experimental tests. While this might not be an issue for a large company like Volvo Cars having both the financial and employee capacity to perform additional experiments, this could prove difficult to implement in a medium or small size company.

To avoid the introduction of additional experiments, a phenomenological approach can be taken. A phenomenological approach for the differentiated bending correction of the FLC would however require extensive research on the bending behaviour in the uniaxial and biaxial loading conditions for a wide range of aluminium and steel alloys. One option is to investigate the possibility of introducing some general offset relationships for the two currently undefined regions based on e.g. crystallographic structure as it is seen in the BBC05 constitutive model with the exponent M (Banabic & Sester 2012).

9.2.2 Path Dependency

Looking at the strain paths presented in Figure 9.4, another concern about the proposed approach is raised. The strain paths presented are almost linear, which is one of the demands for using the standard FLD. Previous research on this exact topic by e.g. Volk et al. (2012), Volk et al. (2013), and Mattiasson et al. (2014) has shown that the standard FLD does not predict accurately when non-linear or even broken strain paths are present during the stamping operation. Since the method relies on offsetting the standard FLC, the forming limit surface presented in Chapter 8 will naturally adhere to the same conditions as the standard FLC. Therefore, in its current form the BC-FLS approach follows the same demands about strain path linearity as the standard FLD.

In order to account for this, two different approaches could be taken:

1. Non-linear GISSMO approach (discussed in Section 9.1.2).
2. Modified Non-linear Forming Limit Diagram (proposed by Volk et al. (2012) and Volk et al. (2013)).

Previously in this chapter, the path dependency of the GISSMO approach was discussed. Here it was presented, that an approach relying on an accumulation of failure through the stamping operation could possibly solve the path dependency problem. If this issue with the GISSMO approach is addressed, it is believed to be a strong contender for the way of solving the path dependency issue that the BC-FLS approach has in its current form.

Another option is to apply the concept of the Non-linear Forming Limit Diagram proposed proposed by Volk et al. (2012) and Volk et al. (2013). In order to apply this theory, a modification of the current implementation in AutoForm$^{\text{plus}}$ R8 is needed. Currently, the approach determines the non-linear failure in the membrane layer, thereby not fully grasping the bending effects of the specimens presented in this report.

The Non-linear Forming Limit Diagram has previously been attempted validated for the bending-under-tension specimens in both Barlo (2019) and Barlo et al. (2019). In the work presented by Barlo (2019) it was presented, that a compilation of a metamodel requiring a large database of material data is needed. A creation of such material database would be extremely expensive. If a way of accumulating the failure in the GISSMO model can be found (without the use of a metamodel requiring a material database) this would be the preferred way to account for non-linear strain paths.

9.2.3 Determination of Limit Strain for Smaller Tool Nose Radii

In the current version of the BC-FLS for the aluminium alloy, the lowest tool nose radius included in the model is 3 mm. As this initially provides a good indication of the bending effect, smaller tool nose radii definitions are needed for the application in the automotive industry. For components such as doors, fenders, and side members, tool nose radii is seen as low as 1 mm. In order to be able to predict components drawn over a tool nose radius this sharp, two approaches can be taken:

1. Alter or expand the current experimental series.
2. Use a mathematical approach.

As previously discussed, an approach using additional experimental testing is an option to define the differentiated bending correction of the FLC. Currently, the bending-under-tension tests for the plane strain bending correction uses tool nose radii of 3, 6, and 10 mm. An additional experimental test can be added to also include the 1 mm nose radius. This adds a higher level of accuracy to the model, but also increases the cost of the entire determination. Another option if the extension for the smaller radii is determined experimentally, is to use three nose radii but have them more evenly distributed between the standard FLC (50 mm) and the low 1 mm radius.

Another option is to use a mathematical approach to predict failure strains in lower tool nose radii. A polynomial fitting of a trendline based on the experimentally determined failure strains could be a suggestion. One downside to this method is that it is currently not known if the bending effect gets 'saturated' when passing a certain sheet thickness / tool nose radius ratio α.

Conclusion 10

The following chapter will present the conclusion of this report. Initially two sub-conclusions regarding the two investigated evaluation spaces will be presented followed by an overall conclusion answering the problem statement presented in Chapter 2.

10.1 Sub-Conclusion 1 - The GISSMO approach

Chapter 5 presented an approach mapping the principal strain space into the stress triaxiality space utilizing transformation equations based on the von Mises constitutive equations. During the presentation of the approach, it was found that the constitutive equations used for the transformation equations could be decoupled from the constitutive model used for the FE material model. A comparison of a transformation based on the von Mises and BBC05 constitutive equations was presented, and the difference of the yielded damage was negligible.

The GISSMO approach presented was attempted validated through Finite Element models of bending-under-tension specimens bend over a punch nose radius of 6 mm. Both an AA6016 aluminium alloy and a CR440Y780T-DP dual-phase steel alloy were used for the validation. The approach performed well for the AA6016 aluminium alloy yielding an accurate prediction of the onset of localized necking in the specimen, however a poor performance for the CR440Y780T-DP dual-phase steel alloy specimen was seen. This lead to the conclusion that the bending effect was more significant for the CR440Y780T-DP dual-phase steel alloy than for the AA6016 aluminium alloy.

The conclusion on the GISSMO approach based on the work presented in this thesis is that it can not be accepted as a general approach for failure prediction in specimens exposed to combined tension and bending based on its inability to accurately predict the onset of localized necking for both of the tested alloys.

10.2 Sub-Conclusion 2 - The Bending Corrected Forming Limit Surface Approach

With the conclusion of the bending effect playing a role in the inability of the GISSMO approach to accurately predict the onset of localized necking in both alloys, a bending correction of the standard Forming Limit Curve (FLC) was presented in Chapter 8. This bending correction of the FLC was performed using the bending-under-tension experiments why a special panel designed at Volvo Cars was used to validate the model to avoid a false positive performance. The bending correction of the FLC was performed by identifying the major strain difference between the FLC, created from the ISO standard Nakajima tests, and the global maximum major strain at the onset of localized necking in the bending-under-tension specimens. Furthermore, to distinguish between when to apply which curve, the curvature κ was introduced as a parameter thereby moving the standard FLC from the two-dimensional principal strain space, to a three-dimensional space defined by the minor strain ε_{22}, the curvature κ, and the failure strain ε_f thereby creating a Bending Corrected Forming Limit Surface (BC-FLS)

The BC-FLS was implemented as a User Defined Variable (UDV) in AutoForm^{TM} R8 for validation through a FE model of the specially designed panel. The implementation yielded excellent results accurately predicting all the investigated areas. Therefore, the approach was concluded to be valid for that exact panel. However being in the early stages of development, it was also concluded in the discussion of the approach, that in its current form, it is only valid when handling components having linear strain paths and having strains in the plane strain region.

10.3 Overall Conclusion

In Chapter 2 the overall objective of this thesis was defined as:

"*How can the onset of localized necking accurately be predicted by Finite Element simulation tools for AA6016 aluminium alloy sheets exposed to various cases of combined tension and bending?*"

Through the work presented in this thesis, this objective has been partially fulfilled with the introduction of the Bending Corrected Forming Limit Surface presented in Chapter 8. The reason for only partially fulfilling the overall objective of this thesis is due to the reasons presented in Sub-conclusion 2, where the model was concluded only to be valid for one load case. However, due to the positive performance of the approach when validated with the Volvo Cars Test Die, it is concluded, that the introduction of this approach is a step in the right direction towards a more general and accurate failure prediction approach for sheet metals.

11 Future Work

This chapter will presented the future work that the author finds relevant to conduct based on the work presented in the report. As most of the future work has already been briefly described in the discussion in Chapter 9, this futures works chapter will mostly be a summary of the discussed topics adding none to very little new ideas.

The following topics are deemed important for future work:

1. Standardize experimental approach for bending correction.
2. Investigation of mathematical approach for small radius failure strain determination
3. Investigation of phenomenological approach for differentiated bending correction
4. Investigation path independence in both the GISSMO and BC-FLS approach.

Once all of the above listed focus areas are addressed, the next step is to validate the models for several material grades of both aluminium and dual-phase steels.

11.1 Standardization of Experimental Approach

As discussed in Chapter 9 an experimental approach can be taken to determine both the small radii failure strains and the differentiated bending correction. In order to do so, some form of standardization is needed for the experimental bending-under-tension tests. This standardization would include, but not be limited to, the following:

- Blank dimensions for the uniaxial, plane strain, and biaxial bending-under-tension tests.
- Ram velocity of with which the specimens are tested
- Environmental settings
- Lubrication of experimental setup.
- DIC post processing approach.
- Curvature definition.

Even if an experimental approach to determining the small radii failure strains and differentiated bending correction is not chosen, this standardization should be created anyhow since the mathematical and phenomenological alternatives needs experimental validation.

11.2 Small Radius Failure Strain Determination

For the determination of the failure strain for small radii, the focus of the future work should be on the mathematical approach discussed in Chapter 9. This is suggested as the standardization of the bending-under-tension tests would cover the experimental approach. The two different approaches can however not be completely decoupled since the experimental approach would be needed to validate the mathematical approach.

The other way around, the mathematical approach could have an influence on which tool radii is used for an experimental approach. This is believed since α values too close to each other could have a negative effect on the mathematical approach, where the failure strain could be seen decreasing when passing a certain α value due to trendline fitting.

11.3 Differentiated Bending Correction

As for the determination of the small radii failure strains, the experimental approach for a differentiated bending correction would be covered by the standardization of the bending-under-tension experiments. Instead the main focus for this area should be a phenomenological approach as discussed in Chapter 9.

The phenomenological approach for the differentiated bending correction of the standard Forming Limit Curve (FLC) would require extensive studies of several grades of both aluminium and steel to create a general phenomenological model based on e.g. the crystallographic structure of the materials. Initially, the studies should be based on specimens exposed to the ram velocity and environment temperature determined in the standardization of the experiments, but in order to increase model accuracy, eventually both strain rate and temperature dependency should be included.

Bibliography

Andrade, F. X. C., Feucht, M. & Haufe, A. (2016), 'An incremental stress state dependant model for ductile failure prediction', *International Journal of Fracture* **200**, 127–150.

Atzema, E. H., Fictorie, E., van den Boogard, A. H. & Droog, J. M. M. (2010), The influence of curvature on flcs of mild steel, (a)hss and aluminium, *in* R. Kolleck, ed., 'Tools and Technologies for the Processing of Ultra High Strength Steels', IDDRG, pp. 519–528.

Banabic, D. (2010), *Sheet Metal Forming Processes - Constitutive Modelling and Numerical Simulation*, number ISBN 9783540881124, 1st edn, Springer.

Banabic, D. & Sester, M. (2012), 'Influence of material models on the accuracy of the sheet metal simulation', *Material and Manufacturing Processes* **27**, 304–308.

Barlo, A. (2019), *Failure prediction of dual-phase steel and aluminium alloys exposed to combined tension and bending*, number ID 292739853, 1st edn, Aalborg University Project Library.

Barlo, A., Sigvant, M. & Endelt, B. (2019), On the failure prediction of dual-phase steel and aluminium alloys exposed to combined tension and bending, *in* 'Proceedings of the IDDRG2019 Conference, Enschede, The Netherlands', IDDRG.

Ertürk, S., Sester, M. & Selig, M. (2018), Limitations of forming limit diagrams: Consideration of bending strain, surface and edge cracks, *in* '2018 FTF Conference Proceedings', FTF.

Gorji, M. (2015), Instability and Fracture Models to Optimize the Metal Forming and Bending Crack Behaviour of Al-Alloy Composites, PhD thesis, ETH Zurich.

Keeler, S. & Backofen, W. (1964), 'Plastic instability and fracture in sheet stretched over rigid punches', *ASM Trans. Quart.* **56**, 25–48.

Mattiasson, K., Jergéus, J. & DuBois, P. (2014), 'On the prediction of failure in sheets with special reference to strain path dependence', *International Journal of Machanical Sciences* **88**, 175–191.

Needleman, A. & Tvergaard, V. (1977), 'Necking of biaxially stretched elastic-plastic circular plates', *Journal of the Mechanics and Physics of Solids* **25**, 159–183.

Neukamm, F., Feucht, M., Haufe, A. & Roll, K. (2008), 'On closing the constitutive gap between forming and crash simulation', *Proceedings of the 10^{th} International LS-DYNA Users Conference, Detroit, United States of America* pp. 12–21.

Sigvant, M., Mattiasson, K. & Larsson, M. (2008), The definition of incipient necking and its impact on experimentally or theoretically determined forming limit curves, *in* 'Proceedings of the IDDRG2008 Conference', IDDRG.

Sowerby, R. & Duncan, J. L. (1971), 'Failure in sheet metal in biaxial tension', *International Journal of Mechanical Sciences* **13**, 217–229.

Sriram, S., Wong, C., Huang, M. & Yan, B. (2003), 'Stretch bendability of advanced high strength steels', *SAE Transactions* **112**, 641–649.

Volk, W., Hoffmann, H., Suh, J. & Kim, J. (2012), 'Failure prediction for nonlinear strain paths in sheet metal forming', *CIRP Annals - Manufacturing Technology* **61**, 259–262.

Volk, W., Weiss, H., Jocham, D. & Suh, J. (2013), Phenomenological and numerical desription of localized necking using generalized forming limit concept, *in* '2013 IDDRG Conference Proceedings', IDDRG.

Yoshida, H., Takamura, M., de Caix, C.-P. B. & Gigant, A. (2008), *ISO 12004 Metallic materials - Sheet and strip - Part 2: Determination of forming limit curves in the laboratory*, 1st edn, International Organization for Standardization, Geneva, Switzerland.

Appendices

Transformation Equations A

The following appendix will present the the derivation of the expressions to transform the limit curves of the GISSMO failure prediction approach from the principal strain space to the stress triaxiality space.

A.1 Derivation of the Stress Triaxiality Expression

First, the expression for the stress triaxiality is derived. The assumption of a plane stress state ($\sigma_{33} = 0$) result in the following expressions for the von Mises equivalent stress and the stress triaxiality:

$$\overline{\sigma}_{vm} = \sqrt{\sigma_{11}^2 - \sigma_{11} \cdot \sigma_{22} + \sigma_{22}^2} \qquad \text{and} \qquad \eta = \frac{\sigma_{11} + \sigma_{22}}{3 \cdot \overline{\sigma}_{vm}} \tag{A.1}$$

An assumption of associated flow is made

$$d\boldsymbol{\varepsilon} = d\overline{\varepsilon}^p \cdot \frac{d\overline{\sigma}_{vm}}{d\boldsymbol{\sigma}} \qquad \rightarrow \qquad \begin{bmatrix} d\varepsilon_{11} \\ d\varepsilon_{22} \end{bmatrix} = d\overline{\varepsilon}^p \cdot \begin{bmatrix} \dfrac{2 \cdot \sigma_{11} - \sigma_{22}}{2 \cdot \overline{\sigma}_{vm}} \\ \dfrac{2 \cdot \sigma_{22} - \sigma_{11}}{2 \cdot \overline{\sigma}_{vm}} \end{bmatrix} \tag{A.2}$$

Assuming linear deformation path $d\varepsilon = \varepsilon$ we get

$$\begin{bmatrix} \varepsilon_{11} \\ \varepsilon_{22} \end{bmatrix} = \overline{\varepsilon}^p \cdot \begin{bmatrix} \dfrac{2 \cdot \sigma_{11} - \sigma_{22}}{2 \cdot \overline{\sigma}_{vm}} \\ \dfrac{2 \cdot \sigma_{22} - \sigma_{11}}{2 \cdot \overline{\sigma}_{vm}} \end{bmatrix} \tag{A.3}$$

Splitting the matrix in Equation A.3 into components we get:

$$\varepsilon_{11} = \overline{\varepsilon}^p \cdot \frac{2 \cdot \sigma_{11} - \sigma_{22}}{2 \cdot \overline{\sigma}_{vm}} \qquad \text{and} \qquad \varepsilon_{22} = \overline{\varepsilon}^p \cdot \frac{2 \cdot \sigma_{22} - \sigma_{11}}{2 \cdot \overline{\sigma}_{vm}} \tag{A.4}$$

$$\downarrow$$

$$\frac{2 \cdot \overline{\sigma}_{vm}}{\overline{\varepsilon}^p} \cdot \varepsilon_{11} = 2 \cdot \sigma_{11} - \sigma_{22} \qquad \text{and} \qquad \frac{2 \cdot \overline{\sigma}_{vm}}{\overline{\varepsilon}^p} \cdot \varepsilon_{22} = 2 \cdot \sigma_{22} - \sigma_{11} \tag{A.5}$$

Multiplying the right expression in Equation A.5 with two, and adding both terms in Equation A.5, the following can be found:

$$\frac{4 \cdot \overline{\sigma}_{vm}}{\overline{\varepsilon}^p} \cdot \varepsilon_{11} + \frac{4 \cdot \overline{\sigma}_{vm}}{\overline{\varepsilon}^p} \cdot \varepsilon_{22} = 3 \cdot \sigma_{11} \qquad \rightarrow \qquad \sigma_{11} = \frac{2}{3} \cdot \frac{\overline{\sigma}_{vm}}{\overline{\varepsilon}^p} \cdot (2 \cdot \varepsilon_{11} + \varepsilon_{22}) \tag{A.6}$$

Performing the same operation the other way around (multiply the right expression in Equation A.5 with two), we get a similar expression:

$$\sigma_{22} = \frac{2}{3} \cdot \frac{\overline{\sigma}_{vm}}{\overline{\varepsilon}^p} \cdot (2 \cdot \varepsilon_{22} + \varepsilon_{11}) \tag{A.7}$$

Inserting Equations A.6 and A.7 into the triaxiality expression presented in Equation A.1, the following reduction can be performed:

$$\begin{aligned}\eta &= \frac{\frac{2}{3} \cdot \frac{\overline{\sigma}_{vm}}{\overline{\varepsilon}^p} \cdot (2 \cdot \varepsilon_{11} + \varepsilon_{22} + 2 \cdot \varepsilon_{22} + \varepsilon_{11})}{3 \cdot \overline{\sigma}_{vm}} \\ &= \frac{\frac{2}{3} \cdot (3 \cdot \varepsilon_{11} + 3 \cdot \varepsilon_{22})}{3 \cdot \overline{\varepsilon}^p} \\ &= \frac{2 \cdot (\varepsilon_{11} + \varepsilon_{22})}{3 \cdot \overline{\varepsilon}^p} \qquad \square\end{aligned} \tag{A.8}$$

A.2 Derivation of the Equivalent Plastic Strain Expression

Next, the expression for the equivalent plastic strain is derived. Still assuming a plane stress state, and a von Mises yield locus, the equivalent plastic strain can be expressed as follows:

$$\overline{\varepsilon}^p = \sqrt{\frac{2}{3} \cdot (\sigma_{11}^2 + \sigma_{22}^2 + +\sigma_{33}^2)} \tag{A.9}$$

The volume consistency is defined as follows:

$$\varepsilon_{33} = -\varepsilon_{11} - \varepsilon_{22} \tag{A.10}$$

Inserting Equation A.10 into Equation A.9, the following can be derived:

$$\begin{aligned}\overline{\varepsilon}^p &= \sqrt{\frac{2}{3} \cdot (\varepsilon_{11}^2 + \varepsilon_{22}^2 + \varepsilon_{11}^2 + \varepsilon_{22}^2 + 2 \cdot \varepsilon_{11} \cdot \varepsilon_{22})} \\ &= \sqrt{\frac{4}{3} \cdot (\varepsilon_{11}^2 + \varepsilon_{22}^2 + \varepsilon_{11} \cdot \varepsilon_{22})} \qquad \square\end{aligned} \tag{A.11}$$

BBC Transformation Algorithm B

The following appendix will present an algorithm for transforming limit curves and strain fields from the principal stress space to the stress triaxiality space using the BBC05 constitutive model. The equations and algorithms is based on the work presented in (Gorji 2015, Section 5.2.1)

Two definitions are created of the stress ratio α and strain ratio β. The stress ratio α is limited to take a value between 0 (uniaxial tension) and 1 (equi-biaxial tension).

$$\alpha = \frac{\sigma_{22}}{\sigma_{11}} \qquad \text{and} \qquad \beta = \frac{\Delta\varepsilon_{22}}{\Delta\varepsilon_{11}} \tag{B.1}$$

Two auxiliary functions are defined by Gorji (2015):

$$f(\alpha) = \frac{\sigma_{11}}{\overline{\sigma}} \qquad \text{and} \qquad g(\beta(\alpha)) = \frac{\Delta\overline{\varepsilon}}{\Delta\varepsilon_{11}} \tag{B.2}$$

Assuming associated flow rule for a given yield function, the strain ratio parameter can be rewritten:

$$\because \Phi(\sigma_{11}, \sigma_{22}) = 0 \qquad \therefore \beta = \frac{\frac{\partial\Phi}{\partial\sigma_{22}}}{\frac{\partial\Phi}{\partial\sigma_{11}}} \tag{B.3}$$

Assuming plane stress, and considering the work equivalent plastic theory, the auxiliary function $g(\beta(\alpha))$ can be defined as:

$$g(\beta) = f(\alpha) \cdot (1 + \alpha \cdot \beta) \tag{B.4}$$

Assuming plane stress condition, the stress triaxiality parameter can be expressed as a function of $f(\alpha)$ and the stress ratio α:

$$\eta = f(\alpha) \cdot \frac{1 + \alpha}{3} \tag{B.5}$$

With the above relations created by Gorji (2015), an algorithm for determining the stress triaxiality based on strain path history can be created. This algorithm can be found in Algorithm 1.

Algorithm 1: Implicit computation algorithm for the stress triaxiality η based on strain path history.

I: Evaluation of functions $f(\alpha)$, $\beta(\alpha)$, and $g(\beta(\alpha))$

for $\alpha = 0 : 1$ **do**

    $f(\alpha)$;
    $\beta(\alpha) = \frac{\partial\phi}{\partial\sigma_{22}} / \frac{\partial\phi}{\partial\sigma_{11}}$;
    $g(\beta(\alpha))$;

II: Evaluation of η for the different strain paths

for $t = 0 : t_{end}$ **do**

    ${}^{t}\Delta\varepsilon_{11} = {}^{t}\varepsilon_{11} - {}^{t-\Delta t}\varepsilon_{11}$
    ${}^{t}\Delta\varepsilon_{22} = {}^{t}\varepsilon_{22} - {}^{t-\Delta t}\varepsilon_{22}$
    $\beta = \frac{{}^{t}\Delta\varepsilon_{22}}{{}^{t}\Delta\varepsilon_{11}}$
    $\Delta\overline{\varepsilon} = g(\beta(\alpha)) \cdot \Delta\varepsilon_{11}$
    ${}^{t}\overline{\varepsilon} = \Sigma\Delta\overline{\varepsilon}$
    ${}^{t}\eta = {}^{t}f(\alpha) \cdot \frac{1+{}^{t}\alpha}{3}$

Electronic Appendix C

The following appendix presents the structure of the electronic appendix as well as provide a brief description of the MatLab files used for the application of the GISSMO failure prediction approach.

In the electronic appendix main folder the following items are found:

- MatLab_GISSMO
- Stress_vs_Strain_Based_Transformation
- FTF2019_Poster

C.1 MatLab_GISSMO

The item MatLab_GISSMO is a folder containing all necessary files, scripts, and functions to predict failure using the GISSMO approach presented in Chapter 5. As an example, the necessary files for the AA6016 aluminium alloy R6 bending-under-tension test is used. The files included in the folder will be listed below with a short description of its purpose.

AA6016_R6_CorrectDepth_ElementData.csv

This comma separated values (csv) file contains the element data from the Finite Element simulation in AutoForm^{plus} R8. The construction of the file is as follows:

1	2	3	4	5	6	7	8
Elemend Idx	Node Idx 1	Node Idx 2	Node Idx 3	Plastic Strain	Zones	Major Strain	Minor Strain

All values are exported at the end of the FE simulation.

AA6016_R6_CorrectDepth_NodeData.csv

This comma separated values (csv) file contains the node coordinate data from the Finite Element simulation in AutoForm^{plus} R8. The construction of the file is as follows:

1	2	3	4	5	6
Node Idx	XCoord	YCoord	ZCoord	Initial XCoord	Initial YCoord

All values are exported at the end of the FE simulation.

FailureCurvesAA6016.csv

Comma separated values (csv) file containing the data points for the standard FLCs of the AA6016 aluminium alloy.

GISSMO_MainScript

This MatLab file (.m) is the main file that runs the entire GISSMO approach, loading in the data files (.csv) and calling the different functions (.m) used.

LayerSeparation.m

This MatLab function (.m) takes the node file and separates node coordinates if multiple layers are evaluated.

VariableSeparation.m

This MatLab function (.m) takes the element file and creates vectors containing the major and minor strains of the specimen strain field.

vmLimitTransformation.m

This MatLab function (.m) performs the transformation of the standard FLCs loaded into the main script.

C.2 Stress_vs_Strain_Based_Transformation

The item Stress_vs_Strain_Based_Transformation is a folder containing the files and MatLab script to investigate the stress versus strain based transformation approaches.

C.3 FTF2019_Poster

For the 2019 Forming Technology Forum (FTF) conference in Munich, Germany, a poster has been submitted with the paper. Since the poster is an A0 size, this has been place in the electronic appendix instead of being included in the report as the two conference papers.

On the Failure Prediction of Dual-Phase Steel and Aluminium Alloys Exposed to Combined Tension and Bending

Alexander Barlo[1,2*], Mats Sigvant[1,3], and Benny Endelt[2]

[1]Volvo Cars Dept. 81110 Strategy & Concept, Olofström, Sweden

[2]Department of Materials and Production, Aalborg University, Aalborg, Denmark

[3]Department of Mechanical Engineering, Blekinge Institute of Technology, Karlskrona, Sweden

E-mail: `Alexander.Barlo@volvocars.com`

Abstract. The interest in accurate prediction of failure of sheet metals in the automotive industry has increased significantly over the last two decades. This paper aims to evaluate two failure prediction approaches implemented in the commercial Finite Element code AutoForm$^{\text{plus}}$ R7.04; (i) the standard Forming Limit Diagram (FLD), and (ii) the Non-linear Forming Limit Diagram. The evaluation will be testing the two approaches accuracy on predicting failure of both an AA6016 aluminium alloy and a CR440Y780T-DP dual-phase steel alloy specimen exposed to combined tension and bending. Based on the findings of this study, it is concluded that neither of the evaluated approaches is able to accurately predict failure in both cases presented.

1. Introduction

In the automotive industry today, a lot of effort is put into the failure prediction of sheet metal parts to ensure stamping process feasibility. Even though a large variety of failure prediction approaches have been proposed during the last decade, none of these have been able to replace the Forming Limit Diagram (FLD) as the industry standard within the sheet metal forming community.

At Volvo Cars Body Components, the focus on accurate failure prediction has increased over the years, and several experiments of AA6016 aluminium and CR440Y780T-DP dual-phase steel alloy specimens, exposed to combined tension and bending, have been performed. The research presented in this paper aims to evaluate two failure prediction methods implemented in the commercial Finite Element code AutoForm$^{\text{plus}}$ R7.04:

(i) The standard Forming Limit Diagram (FLD).

(ii) The Non-linear Forming Limit Diagram.

For clarification, the term FLD is used as a description of the complete Forming Limit Diagram, containing both Forming Limit Curves (FLC) and strain fields.

The evaluation of said methods will be based on numerical models calibrated towards experiments recorded with Digital Image Correlation (DIC) to obtain the history of the forming operation.

2. Experimental Work

2.1. Experimental Setup

Experiments with punch radii of 3, 6, and 10 mm have been conducted in the setup presented in Figure 1. In the setup, the punch is moved 6 mm to the right of the model in order to eliminate the stochastic fracture location, that otherwise would be with the punch located in the centre. All tests have been run to failure, and the applied DIC is used to go back in operation history to investigate the strain development. The focus of this paper will be on the setup with a punch radius of 6 mm.

The experiments are performed as single-action draw operations with a ram velocity of 25 mm/s.

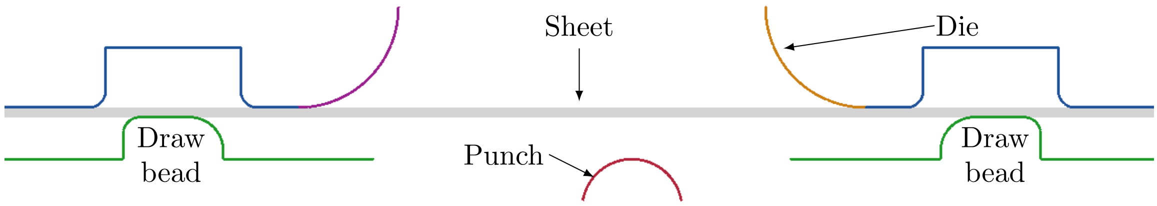

Figure 1. Cross-sectional view of the experimental setup geometry.

2.2. Experimental Repeatability

The repeatability of the AA6016 aluminium alloy is tested, to ensure the experimental data used is not an outlier.

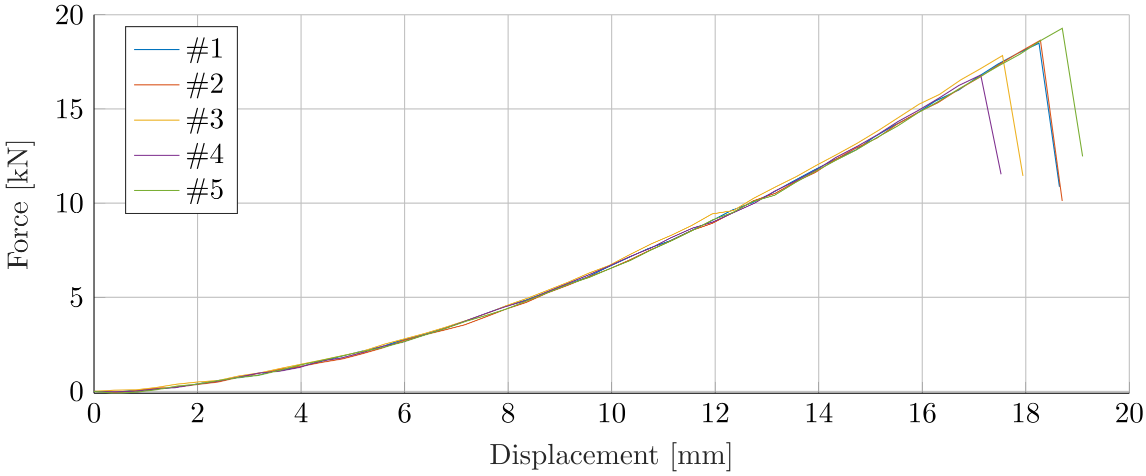

Figure 2. Force-displacement curves of the AA6016 aluminium alloy. Five tests have been conducted in order to determine repeatability.

As presented in Figure 2, the force-displacement curves of the repeated experiments align well on the force levels, but show a deviation between lowest and highest punch depth of approximately 2 mm at the point of fracture.

2.3. Neck Detection of Specimens

An undesirable phenomenon in the sheet metal forming process is failure caused by fracture. To detect if the fracture of the specimens is neck initiated, a test has been terminated approximately

0.5 mm before the fracture should occur. The punch depth of this test is based on the experiment with the lowest displacement (experiment # 4 in Figure 2). Figure 3 presents the result of this test, where a section has been examined and measured under a microscope. The outcome of the examination is that a neck in the specimen is present, why it can be concluded that the fracture is initiated by necking.

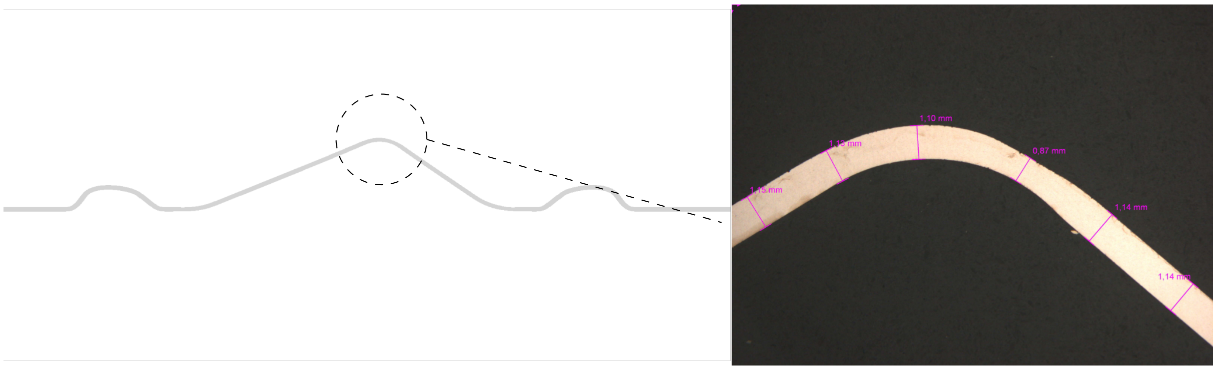

Figure 3. Cross section of an AA6016 specimen. The test has been terminated approximately 0.5 mm before fracture depth. The specimen clearly shows signs of necking.

3. Numerical Reproduction of Experiments

In order to evaluate the two failure criteria proposed, numerical reproductions of the experimental tests have been made in the commercial Finite Element code AutoForm$^{\text{plus}}$ R7.04. Models for both the AA6016 aluminium and CR440Y780T-DP dual-phase steel alloy have been created using the elasto-plastic shell element with 11 integration points through the thickness.

3.1. Material Models

The hardening curves of the material models have been created from a combination of tensile tests and bulge tests. The applied hardening curves can be found in Figures 4 and 5.

The anisotropic behaviour is modelled using the Banabic-Balan-Comsa (BBC) yield criterion for both materials. This is done as more than 10 years of experience at Volvo Cars proves this to perform well. The same experience does however show, that the standard values for the exponent M ($M = 2 \cdot k$, 6 for BCC structure, and 8 for FCC structure [1]) need to be calibrated. The calibration of the exponent is performed by inverse modelling of the Limiting Dome Height (LDH) test.

3.2. Strain Predictions

In order to be secure accurate numerical reproductions of the experiments, a comparison of simulated and experimental major strain values is performed. The comparison is carried out by applying the DIC software ARAMIS$^{\text{TM}}$ by GOM, where a stochastic pattern has been applied to the surface of the experimental specimens prior to testing.

Figures 6 and 7 present the major strain comparison of the numerical models and the experiments. The full lines represent the experimental data, and the dashed lines represent the numeric results. The vertical line at X = 6 mm indicates the center of the punch, and the distances in the legend describe the punch displacement distance from fracture. The predictions

Table 1. Material models used for the numerical reproduction of both the AA6016 aluminium alloy and the CR440Y780T-DP dual-phase steel alloy.

Parameter	**AA6016**	**CR440Y780T-DP**
σ_0	110.3 [MPa]	309.5 [MPa]
σ_{45}	105.9 [MPa]	307.8 [MPa]
σ_{90}	106.5 [MPa]	313.4 [MPa]
σ_b	98.3 [MPa]	307.5 [MPa]
r_0	0.732	0.678
r_{45}	0.535	0.875
r_{90}	0.677	0.848
r_b	1.01	1.02
Exponent (M)	5.7	6.2
Yield Criteria	BBC	BBC
Thickness Stress	ON	ON

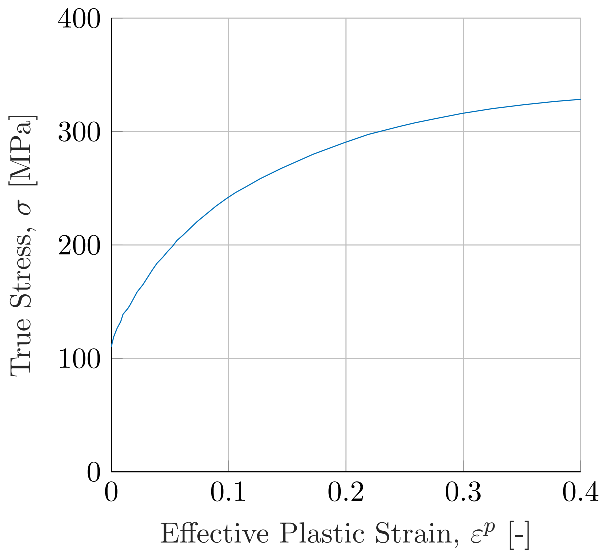

Figure 4. Hardening curve of the AA6016 aluminium alloy.

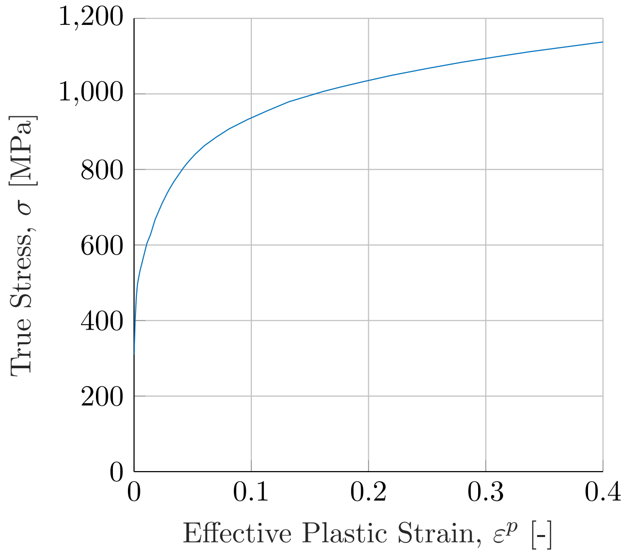

Figure 5. Hardening curve of the CR440Y780T-DP dual-phase steel alloy.

of the numerical models presented corresponds well with those of the experiments up until the last data extracted. This is believed to be due to the initialization of unstable necking, as the last data presented (red lines) are located less than 0.5 mm from fracture. The underprediction of the simulated major strain in the last stages could result in numerical models that do not indicate failure.

4. Failure Prediction

Having obtained numerical models with acceptable accuracy, the two specified failure prediction approaches can now be evaluated.

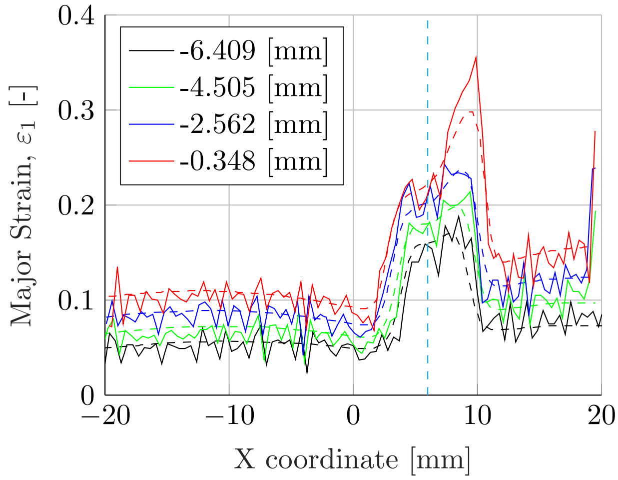

Figure 6. Major strain prediction of the AA6016 aluminium alloy numerical model. The distances presented in the legend cover both the experimental and numerical results.

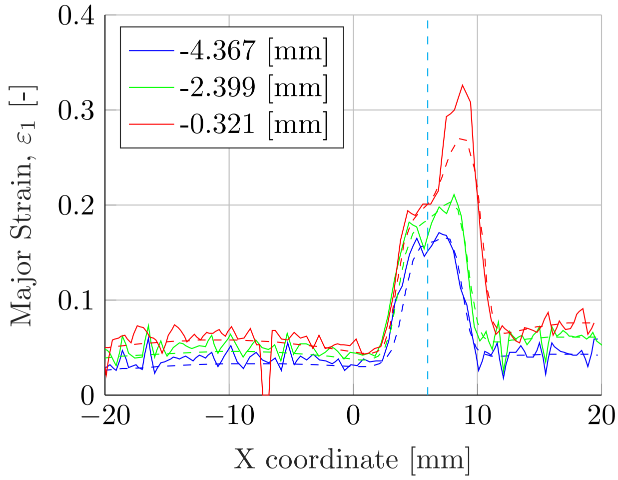

Figure 7. Major strain prediction of the CR440Y780T-DP dual-phase steel alloy numerical model. The distances presented in the legend cover both the experimental and numerical results.

4.1. Standard Forming Limit Diagram (FLD)

The Forming Limit Diagram (FLD) initially proposed by [2], has for the past many years been the industry standard within the automotive industry for predicting failure in sheet metal parts. The FLD does however require proportional loading to be applicable [3][4]. From a theoretical point of view, this would instantly reject the FLD as a suitable approach for failure prediction in specimens exposed to combined tension and bending. However, from an engineering point of view, the FLD approach is tested to investigate if the bending-under-tension load situation in the specimens could be evaluated accurately with the FLD option implemented in AutoForm$^{\text{plus}}$ R7.04.

Figures 8 and 9 present the strain paths of the two alloys in the element with the highest major strain value at the end of the simulation. Strain paths in the bottom (blue), membrane (green), and top (black) layer are presented. As seen, the strain path in both models is far from linear in all layers included. Furthermore, indications of fracture in the top layer of both models is present, despite the numerical model underpredicting the major strain of a point in time where the specimen has not yet fractured. This leads to the conclusion that the standard FLD can not be applied to specimens exposed to combined tension and bending.

4.2. Non-linear Forming Limit Diagram

The evaluation of non-linear strain paths for failure prediction in metal sheets, is a topic that has been discussed for many years. The approach investigated in this paper, is the Non-linear Forming Limit Diagram implemented in AutoForm$^{\text{plus}}$ R7.04 based on [5] and [6]. In short, the approach is expressed by a metamodel of a the total strain path length ratio λ, as presented in Equation 1.

$$\lambda = f(l_{pre}, \beta_{pre}, l_{post}, \beta_{post}) = \lambda_{pre} + \lambda_{post} = \frac{l_{pre}(\beta_{pre})}{l_{FLC}(\beta_{pre})} + \frac{l_{post}(\beta_{post})}{l_{FLC}(\beta_{post})} \tag{1}$$

The Non-linear Forming Limit Diagram is used to predict the onset of necking in sheets. To determine the point where an instability is introduced in the experiments, the approach proposed

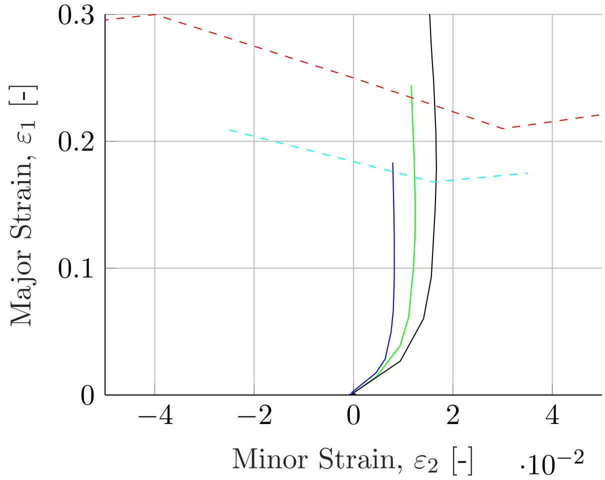

Figure 8. The strain paths of one element in the numerical model of the AA6016 aluminium alloy.

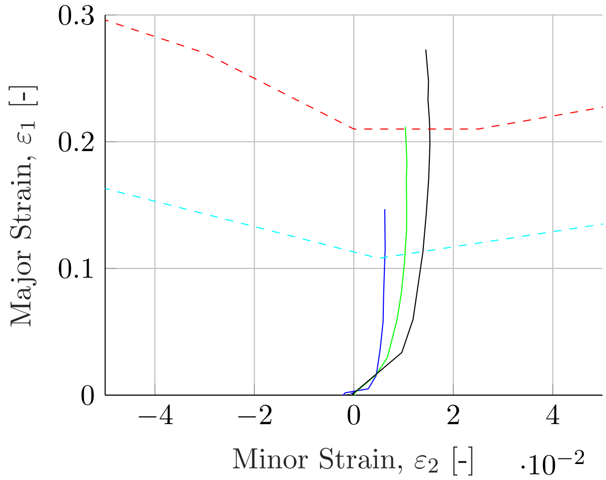

Figure 9. The strain paths of one element in the numerical model of the CR440Y780T-DP dual-phase steel alloy.

by [7], using the first derivative of the major strain with respect to time (strain rate), is applied. The instability point, determined in ARAMIS^{TM}, is then reproduced in the numerical model, and comparisons of the standard Forming Limit Diagram and the Non-linear Forming Limit Diagram can be performed. Figures 10 and 11 present the Forming Limit Diagram and the Non-linear Forming Limit Diagram of the AA6016 aluminium alloy.

The Forming Limit Diagram presented in Figure 10 reveals that the point of instability has been passed. This is in line with the findings in Section 4.1.

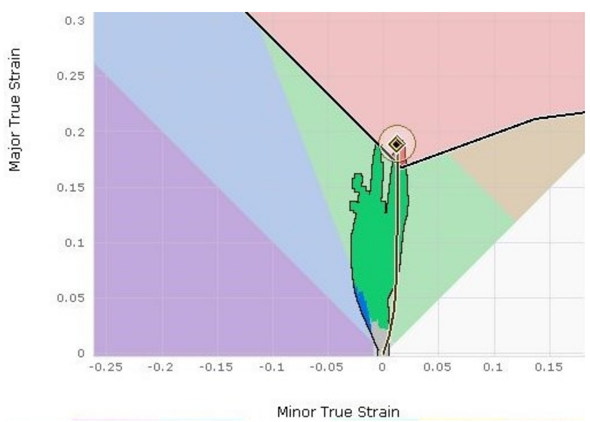

Figure 10. Forming Limit Diagram of the AA6016 aluminium alloy.

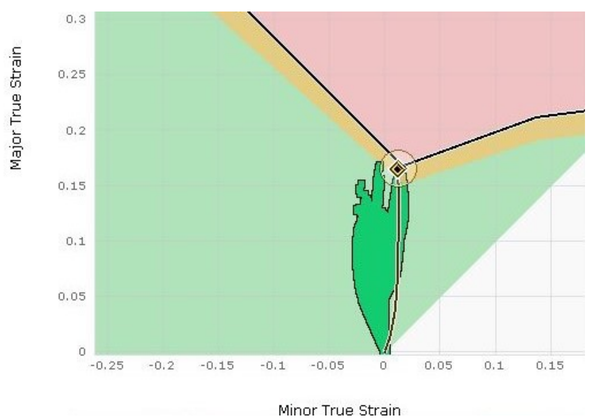

Figure 11. Non-linear Forming Limit Diagram of the AA6016 aluminium alloy.

Turning to the Non-linear Forming Limit Diagram (Figure 11), the model implemented in AutoForm^{plus} R7.04 yields a result that is acceptable, where indication of being on the border of instability is presented. This means that the Non-linear Forming Limit Diagram is an applicable approach in the case of the AA6016 aluminium alloy, but in order to accept it as a general approach, it must also perform well for other materials and radii.

Figures 12 and 13 present the standard Forming Limit Diagram and Non-Linear Forming Limit Diagram of the CR440Y780T-DP dual-phase steel alloy. The same approach for detection of the point of instability as used in the AA6016 aluminium alloy case is applied for this case.

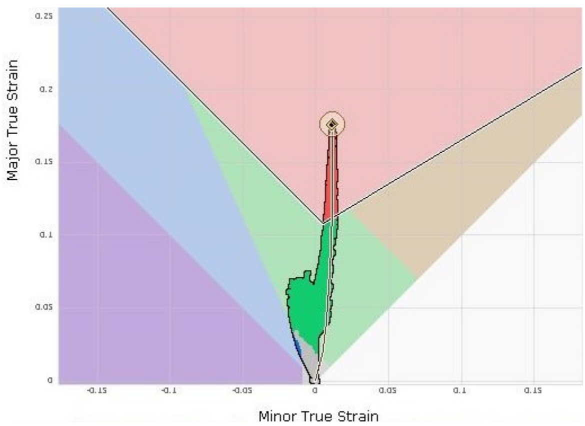

Figure 12. Forming Limit Diagram of the CR440Y780T-DP dual-phase steel alloy.

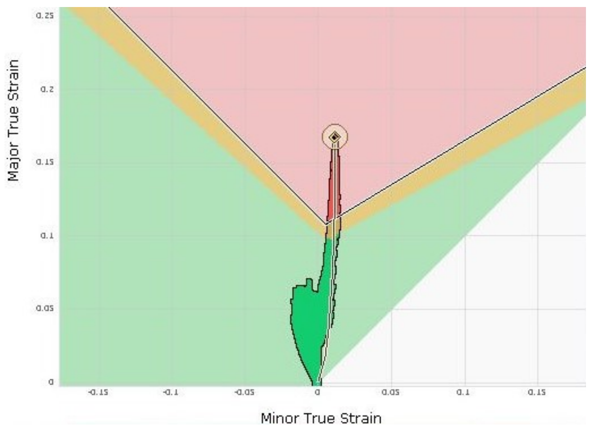

Figure 13. Non-linear Forming Limit Diagram of the CR440Y780T-DP dual-phase steel alloy.

The standard Forming Limit Diagram (Figure 12) yields that the point of instability is passed. What is interesting is that the Non-linear Forming Limit Diagram (Figure 13) also indicates that the point of instability has been passed. Furthermore, the magnitude of the strain level above the instability limit is significant and is believed not to be due to experimental uncertainties.

As the approach has not been able to predict the point of instability in both cases (both the AA6016 aluminium and CR440Y780T-DP dual-phase steel alloy), the authors of this paper can not accept the Non-linear Forming Limit Diagram as a general approach in its current implementation.

5. Conclusion

The work presented in this paper aimed to evaluate the following two failure prediction approaches implemented in the commercial Finite Element code AutoForm^{plus} R7.04 in regards to handle specimens exposed to combined tension and bending:

(i) The standard Forming Limit Diagram (FLD)
(ii) The Non-linear Forming Limit Diagram

Through comparison of experiments and numerical models, the industry standard Forming Limit Diagram proved to be not applicable due to its inability to handle the non-linear strain paths during the forming operation. The Non-linear Forming Limit Diagram yielded an accurate prediction of the AA6016 aluminium alloy, but performed poorly for the CR440Y780T-DP dual-phase steel alloy. Due to the unstable performance of the approach, the Non-linear Forming Limit Diagram is, in this paper, not accepted as a general approach.

Based on the research presented in this paper, it can be concluded that none of the evaluated approaches can be accepted as general approaches to failure prediction of specimens exposed to combined tension and bending.

6. Future Work

As presented in this paper, the two approaches evaluated were not able to accurately predict failure for all cases and failure modes. In both the stamping and crash community, a general accurate approach for predicting different failure modes is of great interest.

An interesting approach to reduce the sensitivity to non-linear strain paths in failure prediction of metal sheets, is to investigate the stress based FLD presented in e.g. [10], where the FLD in the principal strain space is transformed into the principal stress space.

Another interesting approach is the damage accumulation model GISSMO. The GISSMO model relies on tracking the damage state in different stages of the simulation in form of the plastic strain, and comparing it to a specified failure strain value dependent on both the triaxiality [8] and the Lode angle [9]. This approach will be the starting point for further research on this topic by the authors.

Yet another interesting question to raise, is where numerical models are evaluated. Both the standard Forming Limit Diagram and the Non-linear Forming Limit Diagram evaluates the models in the membrane layer, but Figures 8 and 9 present steep strain gradients across the thickness of the blank. Therefore, failure prediction approaches evaluating the blank at the top layer of the model, when exposed to combined tension and bending, is believed to be an interesting approach.

Acknowledgments

The authors of this report would like to thank Dr. Niko Manopulo from AutoForm Engineering GmbH for the interesting discussions about the Finite Element models concerning the AA6016 aluminium alloy. Furthermore, the authors would like to show their gratitude towards Prof. Dr. Wolfram Volk and Mr. Roman Norz from the Lehrstuhl für Umformtechnik und Geißereiwesen at Techniches Universität München for their assistance regarding the Non-linear Forming Limit Diagram approach.

References

[1] Banabic,D. & Sester,M.(2012), 'Influence of material models on the accuracy of the sheet metal simulations', *Material and Manufacturing Processes* **27**, 304-8.

[2] Keeler,S. & Backofen,W.(1964), 'Plastic instability and fracture in sheet stretched over rigid punches',*ASM Trans. Quart.* **56**, 25-48.

[3] Hosford,W.F. & Cadell,R.M.(2007), *Metal Forming - Mechanics and Metallurgy*, ISBN 9780521881210, 3rd edn., Cambridge University Press.

[4] Banabic,D.(2010), *Sheet Metal Forming Processes - Constitutive Modelling and Numerical Simulations*, ISBN 9783540881124, 1st edn., Springer.

[5] Volk,W. et al.(2012), 'Failure prediction for nonlinear strain paths in sheet metal forming', *CIRP Annals - Manufacturing Technology* **61**, 259-262.

[6] Volk,W. et al.(2013), 'Phenomenological and numerical description of localized necking using generalized forming limit concept', *IDDRG Proceedings 2013*, 16-21.

[7] Sigvant,M. et al.(2008), 'The definition of incipient necking and its impact on experimentally or theoretically determined forming limit curves', *Proceedings of the IDDRG2008 Conference*, Olofström, Sweden.

[8] Neukamm,F. et al.(2008), 'On closing the constitutive gap between forming and crash simulation', *10th International LS-DYNA Users Conference*, 12-21.

[9] Basaran,M. et al.(2010), 'An extension of the GISSMO damage model based on lode angle dependence', *9. LS-DYNA Anwenderforum.*

[10] Stoughton, T.B. & Yoon, J.W.(2010), 'A new approach for failure criterion for sheet metals', *International Journal of Plasticity* **27**, 440-459.

INVESTIGATION OF A BENDING CORRECTED FORMING LIMIT SURFACE FOR FAILURE PREDICTION IN SHEET METALS

Alexander Barlo[1,3*], Niko Manopulo[2], Mats Sigvant[1,4], Benny Endelt[3], Kristoffer Trana[1]

[1]Volvo Cars Stamping Engineering, Olofström, Sweden
[2]AutoForm Engineering GmbH, Zürich, Switzerland
[3]Department of Materials and Production, Aalborg University, Aalborg, Denmark
[4]Department of Mechanical Engineering, Blekinge Institute of Technology, Karlskrona, Sweden

ABSTRACT: Ensuring process feasibility is a high priority in the automotive industry today. Within the CAE departments concerning the manufacturing of body components, one of the most important areas of interest is the accurate prediction of failure in components through Finite Element simulations. This paper investigates the possibility of introducing the component curvature as a parameter to improve failure prediction. Bending-under-tension specimens with different radii are used to create a Bending Corrected Forming Limit Surface (BC-FLS), and a test die developed at Volvo Cars, depicting production-like scenarios by exposing an AA6016 aluminium alloy blank to a stretch-bending condition with biaxial pre-stretching, is used to validate the proposed model in the commercial Finite Element code AutoForm™ R8. The findings of this paper showed that the proposed BC-FLS approach performed well in the failure prediction of the test die compared to the already in AutoForm™ R8 implemented max failure approach.

KEYWORDS: Sheet Metal Forming, Failure Prediction, Formability, Curvature Dependency

1 INTRODUCTION

In the automotive industry today, one of the top priorities is to ensure process feasibility. One of the areas where this is seen, is within the Computer Aided Engineering (CAE) departments concerning the design and manufacturing of body components. Over the past years, more complex lightweight materials, such as AHSS and aluminium alloys, have been introduced along with increased component complexity. One of the great challenges the automotive industry faces today in regard to ensuring process feasibility, is the accurate prediction of failure of parts during the engineering phase. Between different industries, the term 'failure' has different meanings, but within the stamping department at Volvo Cars, failure is defined as *the onset of necking*.

For the past decades, the standard way of predicting failure in sheet metal forming simulations has been to apply the Forming Limit Diagram (FLD) originally proposed by Keeler & Backofen [1]. As the research on formability of sheet metals has advanced, the FLD approach has at several occasions been proven to perform poorly e.g. for components experiencing non-linear strain paths, or components where the stamping operation includes bending over a sharp radius.

The latter case has been investigated by e.g. Barlo et al. [2] presenting an evaluation of the performance of the FLD and the Non-Linear Forming Limit Diagram for failure prediction in dual-phase steel and aluminium alloys exposed to bending under tension. This evaluation of the FLD showed that it was indeed not able to accurately predict the onset of necking in a numerical model of the tested components.

Based on these observations, this paper aims to investigate how a bending correction of the standard Forming Limit Curve (FLC) could aid in the accurate failure prediction of components exposed to bending under tension for components of an AA6016 aluminium alloy.

2 EXPERIMENTAL WORK

In this paper two different experimental setups are used other than the Nakajima test setup used to determine the standard FLC:

* Corresponding author: Bruksgatan 1, SE-293 38 Olofström, Sweden, Alexander.Barlo@volvocars.com

1. Bending-under-tension experimental setup
2. Volvo Cars bending-under-tension test die

2.1 BENDING-UNDER-TENSION EXPERIMENTAL SETUP

The bending-under-tension experiments are used to perform the bending correction of the FLC. An experimental setup with three changeable double-curved punches with three different major radii of 3, 6, and 10 mm, and a minor punch radius of 100 mm is used. The reasoning for applying double-curved punches is to reduce the risk of a stochastic fracture location, and for the same reason the punch centre has been offset 6 mm to one side. An illustration of the experimental setup is presented in Figure 1.

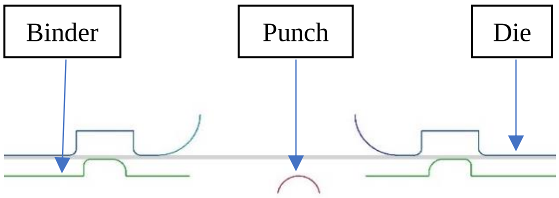

Fig. 1 *Illustration of the bending-under-tension experimental setup. The punch in the setup is changeable between punches of 3, 6, or 10 mm.*

To ensure the stretch-bending condition being present, locking beads (see Figure 2) are used to prevent material flow towards the area exposed to the actual bending operation.

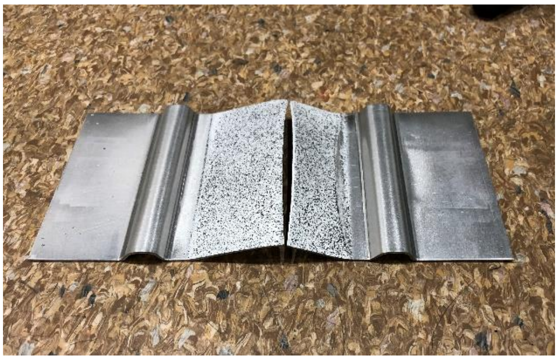

Fig. 2 *Post operation bending-under-tension specimen. The stochastic pattern applied to the surface is used for the DIC analysis.*

The experiments are performed in a single-action mechanical press using the die as the displacing tool, and with a ram velocity of 25 mm/s. The actual experimental setup is presented in Figure 3.

Fig. 3 *Setup for the bending-under-tension experiments.*

On top of the die, two cameras are mounted enabling 3D Digital Image Correlation (DIC) and strain history analysis through the software ARAMIS™ developed by GOM.

2.2 VOLVO CARS BENDING-UNDER-TENSION TEST DIE

The Volvo Cars Bending-Under-Tension Test Die has been developed to depict a more production-like scenario, a s the blank during stamping is exposed to a stretch-bending condition with biaxial pre-stretching as encountered in critical features such as door handles or fenders.

Fig. 4 *Volvo Cars Bending-Under-Tension Test Die panel. The die produces two different geometries, using punch radii of 4 and 8 mm.*

The panel produced by the test die is presented in Figure 4. The die produces two different geometries, and each geometry is repeated two times – one time with nose punch radius 4 mm and one with punch radius 8 mm. Furthermore, each of the geometries are then repeated a number of times with different feature depths to capture the actual forming limits. For the validation of the proposed failure prediction approach, only one of the geometries is initially of interest.

No DIC measurements has been recorded on this panel, why a manual inspection has been performed instead. The outcome of the manual inspection is presented in Figure 5.

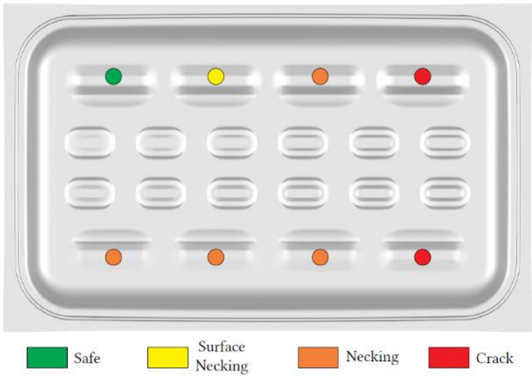

Fig. 5 *Outcome of the manual inspection of the stamped panel. Results for only one geometry is presented as this is initially the only one used for failure prediction approach validation.*

3 MATERIAL CHARACTERIZATION

For a validation of the proposed failure prediction approach, a numerical model of the Volvo Cars Bending-Under-Tension Test Die will be applied.

Table 1: *Material parameters for de modelling of the AA6016 aluminium alloy with the BBC05 yield surface.*

Material Parameter	Value	Unit
R_0	0.732	-
R_{45}	0.535	-
R_{90}	0.677	-
R_b	1.007	-
σ_0	110.3	MPa
σ_{45}	105.9	MPa
σ_{90}	106.5	MPa
σ_b	98.3	MPa
M	5.7	-

To ensure valid numerical results, an important factor is the applied material model. As experience throughout the years at Volvo Cars have shown the BBC05 material model to perform well, this material model will also be applied in this case. Material parameters of the AA6016 aluminium alloy used for the material model are listed in Table 1, and the applied hardening curve is presented in Figure 6.

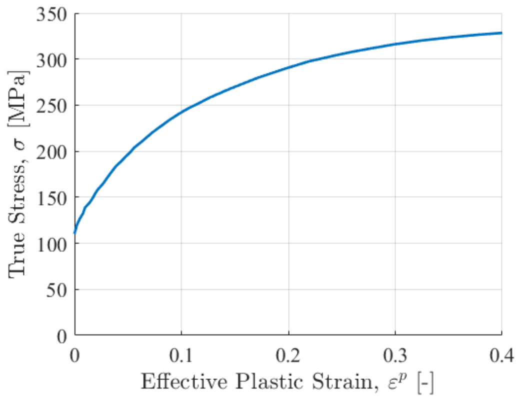

Fig. 6 *Hardening curve of the AA6016 aluminium alloy.*

4 DETERMINING THE EXPERIMENTAL ONSET OF NECKING

As defined in the introduction of this paper, the term failure is defined as onset of necking. Approaches to determine the onset of necking in experiments is something that has been discussed for several years and has still not been defined. To determine the initial FLC for onset of necking, as well as the onset of necking in the bending-under-tension experiments, an approach based on the development of the first derivative with respect to time of the major strain ($\dot{\varepsilon}_1$) proposed by Sigvant et al. [3] is applied. The major strain rate is calculated based on a statistical area introduced to the DIC measurement. The derivative is found using both the previous and next point in time as presented in Equation (1).

$$\dot{\varepsilon}_1 = \frac{\varepsilon_1(t_{n+1}) - \varepsilon_1(t_{n-1})}{t_{n+1} - t_{n-1}} \quad (1)$$

Figure 7 presents an example of how this analysis could turn out. In the method applied, the onset of necking is defined to occur when the maximum measured major strain rate exceeds the predicted average plus three standard deviations.

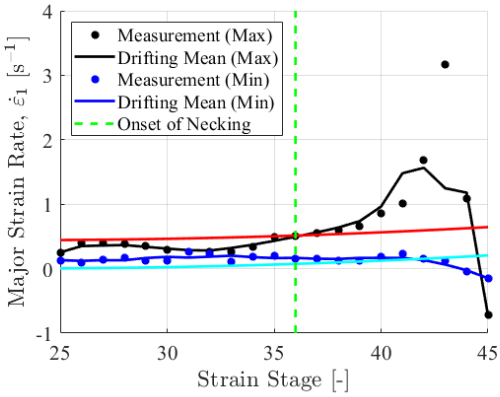

Fig. 7 *Illustration of determination of the onset of necking in a bending-under-tension R6 specimen.*

5 INFLUENCE OF BENDING ON SHEET FORMABILITY

The influence of bending on the formability of sheet materials is something that has been previously investigated by e.g. Atzema et al. [4] and Vallellano et al. [5]. A format often used to visualize the bending effect on sheet formability is to consider the outer surface maximum major strain at maximum force as a function of the thickness / tool radius ratio (α). Performing this check for the AA6016 aluminium alloy bending-under-tension experiments, Figure 8 show an increase in failure strain with the decrease of tool radius.

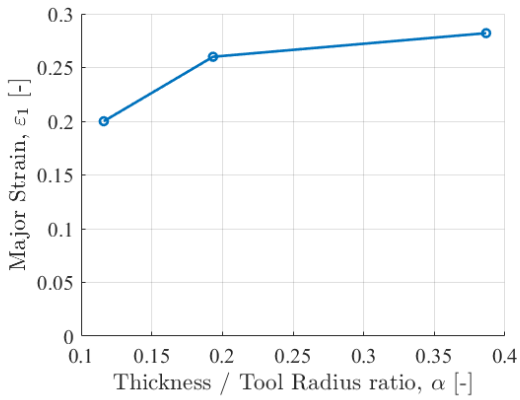

Fig. 8 *Bending influence on the outer surface maximum major strain for the AA6016 aluminium alloy bending-under-tension experiments. The values have been obtained from the DIC analysis.*

The increase of the major strain at the outer surface with a decrease in tool radius illustrates quite well why the FLD performs poorly for bending over sharp radii. The Nakajima test used to determine the standard FLC employs a hemispherical punch with a radius of 50 mm. With this observation, a bending correction of the standard FLC now seems even more interesting.

6 BENDING CORRECTION OF THE STANDARD FLC

In this first attempt to create a bending correction in this paper, the entire FLC will be corrected by an offset ($\Delta\varepsilon_1$). To determine this offset, the DIC measurements of the bending-under-tension experiments are used to find the delta value between the outer surface maximum major strain, and the standard FLC. This delta value is determined as presented in Equation (2) and illustrated in Figure 9.

$$\Delta\varepsilon_1 = \varepsilon_{1,DIC,max} - \varepsilon_{1,FLC}(\varepsilon_{2,DIC}) \tag{2}$$

Table 2 presents the data determined from the DIC measurements of the bending-under-tension experiments. Using Equation (2) the bending corrected curves are determined and presented in Figure 10. The idea of creating a bending corrected FLC has previously been presented by e.g. Ertürk et al. [6] proposing a bending correction of the FLC in the membrane layer of a numerical model.

Table 2: *Values necessary to calculate the $\Delta\varepsilon_{11}$ values for the bending correction.*

Radius	$\varepsilon_{1,DIC,max}$	$\varepsilon_{2,DIC}$	$\varepsilon_{1,FLC}(\varepsilon_{2,DIC})$
3	0.282	0.022	0.173
6	0.260	0.011	0.175
10	0.200	0.001	0.185

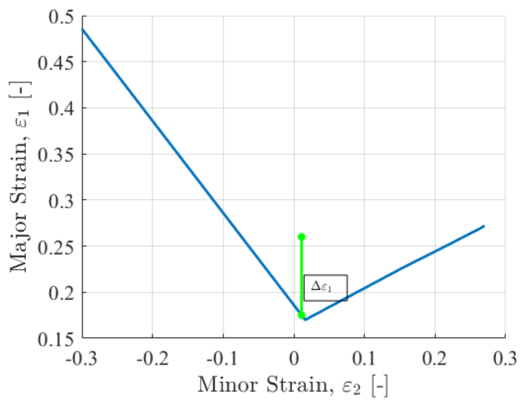

Fig. 9 *Illustration of the determination of the $\Delta\varepsilon_{11}$ value.*

To determine when to use which of the in Figure 10 presented curves, an additional parameter is introduced. In the work presented by Atzema et al. [4] the curvature (κ) on the concave side of the bend (tool curvature) was used as a measure to distinguish between the limit curves. This paper introduces the curvature to distinguish between limit curves, and thereby creating a limit surface. This surface will be called the Bending Corrected Forming Limit Surface (BC-FLS).

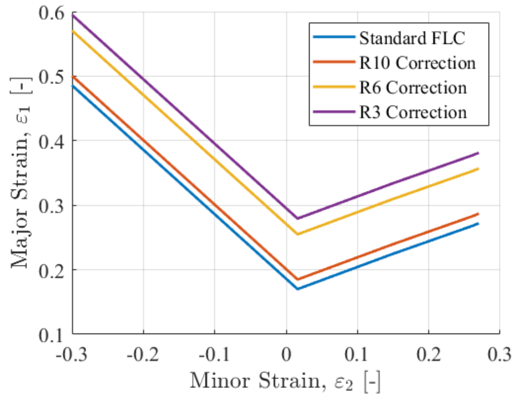

Fig. 10 *Bending corrected forming limit curves of the AA6016 aluminium alloy.*

As in [4], the curvature of the bend will be defined on the concave side i.e. it is calculated directly from the tool radius as presented in Equation (3)

$$\kappa = \frac{1}{R} \tag{3}$$

where *R* is the tool radius. This definition of the curvature yields the values presented in Table 3. The introduction of the curvature transfers the two-dimensional FLC into the three-dimensional space. A polynomial fitting of a surface to the data points, based on the best fit method, a BC-FLS ($\varepsilon_f(\varepsilon_{22}, \kappa)$) is performed, and yields a surface with an adjusted R^2 value of 0.9690. This limit surface is presented in Figure 11.

Table 3: *Curvature values at the concave side of the bend of the bending-under-tension specimens as well as for the Nakajima test.*

Radius:	3	6	10	50
Curvature:	0.3333	0.1667	0.1	0.02

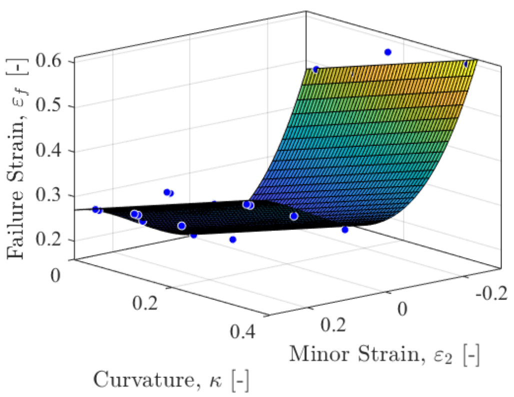

Fig. 11 *Bending corrected forming limit curves of the AA6016 aluminium alloy.*

The created BC-FLS does however have its limitations. Since the surface is fitted to data points, the presented failure strain definition should not be used outside of the experimentally defined space i.e. when the data points do not satisfy the conditions $-0.3 \leq \varepsilon_2 \leq 0.3$ and $0 \leq \kappa \leq 0.35$.

7 NUMERICAL EVALUATION

To validate the proposed BC-FLS approach, a numerical model of the Volvo Cars Bending-Under-Tension Test Die is used. The model is run in the commercial Finite Element code AutoForm^{TM} R8. The model is created using the Elasto-Plastic Shell (EPS) element formulation with 11 integration points through the thickness, as well as an active consideration of surface pressure as a result of tool reactions and binder pressure. A simple friction model is applied using a global Coulomb friction coefficient of 0.12.

In this model, the draw beads have been of significance to ensure the presence of the stretch-bending phenomenon. Therefore, to reduce material flow in the model geometrical draw beads have been used.

To increase the possibility of capturing the onset of necking in the numerical model, a fine mesh is applied in the zones exposed to bending with a minimum element size of 0.62 mm and a maximum allowed element angle of 10°.

To assess the state of the elements in the models, the idea of failure measure (*F*) to each element is introduced. The idea of failure in this model, is a direct relationship between the failure strain ($\varepsilon_f(\varepsilon_2, \kappa)$, Figure 11) and the element major strain at the convex side of the bend (ε_1) as presented in Equation (4). Once the failure measure reaches unity, the onset of necking has been reached for the element.

$$F = \frac{\varepsilon_1}{\varepsilon_f(\varepsilon_2, \kappa)} \tag{4}$$

Having a numerical model of the component, additional options regarding the definition of the curvature have become available. Evaluating the component at the convex side of the bended zones, the curvature is also found at this point. As the curvature could possibly variate within a single element, as exemplified in Figure 12, a choice must be made on which curvature definition should be used for the validation. As previously presented in Figure 8, the failure strain increases with an increase in curvature but due to the definition of the curvature on the concave side of the bend in the creation of the BC-FLS, the curvatures are lower than they should be from the DIC surface measurement. An initial attempt to account for this is to use the mean curvature (as defined in Equation (5)) of the element, thereby also lowering the curvature used for the validation.

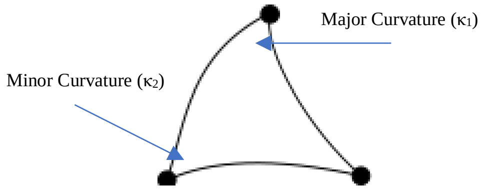

Fig. 12 *Example of curvatures on a triangular shell element.*

$$\text{Mean Curvature} = \frac{\kappa_1 + \kappa_2}{2} \qquad (5)$$

Having defined the curvature to be used in the numerical model, the validation can be performed. For the purpose of visualising the BC-FLS approach, Equation (4) has been implemented as a User Defined Variable (UDV) in AutoForm™ R8. Figures 13 (a) and (b) present the top and bottom rows of the Volvo Car Bending-Under-Tension Test Die component respectively.

(a) Top row R8

(b) Bottom row R4

Fig. 13 *Local failure maxima for one geometry.*

The fringe plots presented for the two rows are so-called 'out of range' plots, meaning all elements having passed a certain threshold are presented without colour. In the case of the BC-FLS the threshold value is set to 1, resulting in all elements having passed the onset of necking is presented without colour in the fringe plots. The results presented seems to accurately predict the failure state observed in the manual inspection of the panel.

To support a claim of this application to perform better than the standard FLD, the Max Failure approach implemented in AutoForm™ R8 is used as a reference. The local max failure maxima are presented in Figures 14 (a) and (b).

Comparing the results from Figures 13 and 14, it can be seen that the proposed BC-FLS approach predicts the onset of necking more accurately than the Max Failure approach implemented in AutoForm™ R8.

(a) Top row R8

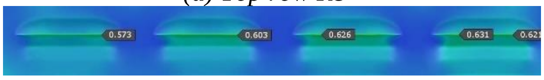

(b) Bottom row R4

Fig. 14 *Local max failure maxima for one geometry.*

8 CONCLUSIONS

This paper presented an approach for failure prediction in sheet metal components exposed to bending over sharp radii during the forming operation. This approach is based on performing a bending correction of the standard Forming Limit Curve (FLC) based on tool curvature, thereby transforming the standard Forming Limit Diagram (FLD) into a Bending Corrected Forming Limit Surface (BC-FLS). The surface was created using experimental data from a series of bending-under-tension tests, where global maximum strain values were used to correct the FLC. From these corrected curves, and the major punch curvature, the BC-FLS was fitted using a best fit approach. An evaluation of the Volvo Cars Bending-Under-Tension Test Die with an AA6016 aluminium alloy blank was performed in the commercial Finite Element code AutoForm™ R8.

The numerical model validated the proposed failure prediction approach, and a comparison of the proposed approach and the already implemented Max Failure approach in AutoForm™ R8 aided to support the claim that the BC-FLS is a step towards a more accurate failure prediction of components exposed to bending-under-tension.

9 FUTURE WORK

The work presented in this paper, is at an early stage why several points of improvements can be pointed out. In its current form, the BC-FLS approach presented in this paper, is a post-processing tool. For the Volvo Cars Bending-Under-Tension Test Die component, the maximum failure (failure as defined by Equation (4)) is fortunately located at the very end of the simulation. However, scenarios of changing strain paths during one or multiple stamping operations could cause onset of necking at an arbitrary point in the process time without the user noticing it. Based on this, the first improvement that must be done to the approach is to introduce the principle of a process maximum failure, where the maximum failure obtained in a specific element is kept, even if this is reduced due to changes in strain paths.

Also the bending correction of the FLC must be improved. As presented in Table 1, the major strains used for the bending correction is in very near proximity of the plain strain loading condition. During their investigation Atzema et al. [4] concluded that the effect of an increased curvature was close to negligible in the proximity of the uniaxial loading condition, moderate in the proximity of the biaxial loading condition and large in the proximity of the plain strain loading condition. This indicates that the bending corrected curves presented in Figure 10, and the BC-FLS presented in Figure 11, heavily overpredict the failure strain limit on parts of the left-hand side of the FLD, while a moderate overestimation is suspected to be present on parts of the right-hand side.

As presented in this paper, the BC-FLS approach has performed well for the Volvo Cars Bending-Under-Tension Test Die with an AA6016 aluminium alloy blank. To verify the approach as being general, the study must initially be extended to investigate multiple grades of aluminium and eventually also to include other material types e.g. dual-phase steel alloys.

REFERENCES

[1] Keeler S. & Backofen W.: *Plastic Instability and Fracture in Sheet Stretched over Rigid Punches*. In: ASM Trans. Quart **56**, 25-48, 1964.

[2] Barlo A., Sigvant M., & Endelt B.: *On the Failure Prediction of Dual-Phase Steel and Aluminium Alloys Exposed to Combined Tension and Bending*. In: The 38th International Deep Drawing Research Group Annual Conference, 2019.

[3] Sigvant M., Mattiasson K. & Larsson M.: *The Definition of Incipient Necking and its implication on Experimentally or Theoretically Determined Forming Limit Curves.* In: 2008 IDDRG Conference Proceedings, 2008.

[4] Atzema E. H., Frictorie E., van den Boogard A. H. & Droog J. M. M.: *The Influence of Curvature on FLCs of Mild Steel, (A)HSS and Aluminium.* In: The 28th International Deep Drawing Research Group Annual Conference, 519-528, 2010.

[5] Vallellano C., Morales D., Martinez A.J., & Garcia-Lomas F. J.: *On the use of the Concave-Side Rule and Critical-Distance Methods to Predict the Influence of Bending on Sheet-Metal Formability.* In: Int J Mater Form **3**, 1167-1170, 2010.

[6] Ertürk S., Sester M., & Selig M.: *Limitations of Forming Limit Diagrams: Consideration of Bending Strain, Surface and Edge Cracks.* In: FTF 2018 Conference Proceedings, 2018.